

**APCVD PREPARATION AND STUDIES OF PHYSICAL
PROPERTIES OF TIN OXIDE THIN FILMS**

by

Ahmed M. Alkaoud

ProQuest Number: 10796801

All rights reserved

INFORMATION TO ALL USERS

The quality of this reproduction is dependent upon the quality of the copy submitted.

In the unlikely event that the author did not send a complete manuscript and there are missing pages, these will be noted. Also, if material had to be removed, a note will indicate the deletion.



ProQuest 10796801

Published by ProQuest LLC (2019). Copyright of the Dissertation is held by the Author.

All rights reserved.

This work is protected against unauthorized copying under Title 17, United States Code
Microform Edition © ProQuest LLC.

ProQuest LLC.
789 East Eisenhower Parkway
P.O. Box 1346
Ann Arbor, MI 48106 – 1346

A thesis submitted to the Faculty and Board of trustees of the Colorado School of Mines in partial fulfillment of the requirements for the degree of Doctor of Philosophy (Applied Physics)

Golden, Colorado

Date April 2, 1999

Signed: Ahmed Alkaoud
Ahmed M. Alkaoud

Approved: Victor Kaydanov
Dr. Victor Kaydanov
Thesis Advisor

Approved: Tim Ohno
Dr. Tim Ohno
Thesis Co-Advisor

Golden, Colorado

Date April 2, 1999

Don Williamson
Dr. Don Williamson
Head of Physics Department

ABSTRACT

Transparent conductive oxides (TCOs) exhibit a unique combination of properties. They are highly conductive and at the same time, unlike usual good conductors, transparent to visible light. Recently, TCOs have found application as a front contact in photovoltaic solar cells. Improving the conductivity along with the transparency can lead directly to a decrease in electrical and optical losses and enhancement of cell efficiency.

Tin oxide is one of the most usable materials in this area because of its availability, good opto-electrical properties, and reasonable cost. The objectives of this investigation were two-fold; first, fabrication of high quality SnO₂:F thin films on inexpensive soda lime glass substrates, and second, studying optical and electrical properties of the films to clarify some basic parameters of the electron system in this material relevant to their figure of merit.

For film fabrication we used atmospheric pressure chemical vapor deposition. After changes in deposition system design and optimizing processing parameters we have succeeded in preparation of SnO₂:F films with optical transmission and sheet conductivity as high as for the best commercially available materials. The structural properties of the films were characterized by using x-ray diffraction, scanning electron microscopy, and atomic force microscopy. For basic studies of the electronic properties we used a variety of

methods and techniques, including measurements of Hall and Seebeck coefficients, electrical resistivity, spectrophotometry and ellipsometry.

Comparative studies of the same basic electronic parameters, such as carrier concentration and mobility, using different methods, enabled us to develop and recommend some new non-destructive techniques for material characterization and mapping of electronic properties over the film area. It was shown that ellipsometry is a very promising method for the comprehensive characterization of SnO₂ thin films and process monitoring.

Combination of optical and electron transport phenomena studies provided reliable information on the band spectrum and scattering effects in SnO₂:F thin films. Effective mass of free electrons in a wide range of energies was determined without any observed indications of nonparabolicity. Comparison of the Hall and optical mobilities was a basis for estimation of the grain boundaries contribution to the film resistivity. Analysis of the experimental data on temperature dependence of mobility and Seebeck coefficient led to the conclusion that mobility in the bulk of the grains is determined and limited by scattering by the ionized impurity Coulomb potential screened with free carriers. It was shown that for theoretical calculations of mobility one has to take into account spatial dispersion of the dielectric constant and compensation of the dopant with acceptor intrinsic defects.

TABLE OF CONTENTS

	Page
ABSTRACT.....	iii
LIST OF FIGURES.....	viii
LIST OF TABLES.....	x
ACKNOWLEDGMENTS.....	xi
CHAPTER 1. INTRODUCTION.....	1
1.1 Motivation for research.....	1
1.2 Objectives of Research.....	5
1.3 Thesis Organization.....	5
CHAPTER 2. BACKGROUND (LITERATURE REVIEW).....	7
2.1 General Physical Properties of TCO.....	7
2.1.1 Optical Properties.....	8
2.1.1.1 Classical Drude Model.....	8
2.1.1.2 Burstein-Moss Effect.....	11
2.1.2 Electrical Properties.....	13
2.2 Review of Properties of SnO ₂	16
2.2.1 Structural Properties.....	16
2.2.2 Optical and Electrical Properties.....	19
2.2.3 Preparation Methods.....	21
2.3 Summary.....	23
CHAPTER 3. EXPERIMENTAL: CHARACTERIZATION METHODS AND TECHNIQUES.....	24
3.1 Structural Properties.....	24
3.1.1 Film Thickness and Surface Roughness.....	24
3.1.2 Grain Size and Orientation.....	25

3.2	Electrical Properties.....	26
3.2.1	Sheet Resistance and Bulk Resistivity.....	26
3.2.2	Hall Effect.....	29
3.2.3	Seebeck Effect (Thermoelectric Power).....	31
3.3	Optical Properties.....	39
3.3.1	Spectrophotometry: Transmission, Absorption, and Reflection Spectra.....	39
3.3.2	Ellipsometry: Dielectric Constant, Plasma Frequency, and Collision Frequency.....	44
3.4	Comparison of Different Methods of Characterization.....	51
3.4.1	Carrier Concentration.....	52
3.4.2	Carrier Mobility.....	56
3.4.3	Structural Properties (Film Thickness and Surface Roughness).....	59
3.5	Summary.....	60
CHAPTER 4. EXPERIMENTAL: SnO₂:F THIN FILM GROWTH AND PROPERTIES.....		62
4.1	Films Growth Using APCVD.....	62
4.1.1	CVD Method Basic: Chemistry of Deposition Process.....	62
4.1.2	APCVD System Used for Deposition.....	64
4.1.3	Effect of the Main Processing Parameters and Improvement of the System Design.....	66
4.1.3.1	Temperature.....	66
4.1.3.2	The Gas Composition and Rate.....	69
4.1.3.3	Exhaust System.....	70
4.1.4	Diffusion Barrier.....	70
4.1.5	Annealing Conditions.....	72
4.2	Films Properties Dependent on the Processing Procedures.....	74
4.2.1	Structural Properties.....	75
4.2.2	Optical Properties.....	81
4.2.3	Electrical Properties.....	88
4.3	Summary.....	90
CHAPTER 5. STUDIES OF BASIC ELECTRONIC PROPERTIES OF SnO₂ THIN FILMS.....		92

5.1	Theory of Electron Transport in Solids.....	92
5.1.1	Approximations of the Theory and Verification of their Validity.....	93
5.1.1.1	Quasi-Continuous Electron Spectrum.....	93
5.1.1.2	Quasi - Classical Approximation.....	94
5.1.1.3	Relaxation Time Approximation.....	94
5.1.1.4	Isotropic Electron Spectrum.....	95
5.1.1.5	Parabolic Electron Spectrum.....	96
5.1.1.6	High Degeneracy of the Carrier gas and Sommerfeld approximation.....	97
5.1.2	Transport Coefficients for the Stationary External Fields.....	100
5.1.3	AC Electrical Conductivity (Plasma and Collision Frequencies).....	105
5.2	Experimental Results and Discussion.....	108
5.2.1	Plasma Frequency and Seebeck Coefficient in the Films with Varying Electron Concentration (Dependence of Energy on the Electron Momentum).....	108
5.2.2	Resistivity and Mobility (Influence of the Grain Boundaries)....	114
5.2.3	Bulk Scattering Mechanism.....	118
5.2.4	Calculation of Mobility in the Bulk of the Grains.....	123
5.3	Summary.....	128
CHAPTER 6 MAJOR RESULTS, CONCLUSIONS, AND RECOMMENDATIONS.....		130
REFERENCES CITED.....		134

LIST OF FIGURES

Figure 2.1.	Illustration of the spectral transmittance of TCO films.....	9
Figure 2.2.	Band Diagrams for Burstien-Moss shift.....	12
Figure 2.3.	Unit cell of SnO ₂ crystal where the small circles indicate tin atoms and the large circles indicate the oxygen atoms.....	17
Figure 3.1.	A collinear four-point probe.....	28
Figure 3.2.	A lamella-type van der Pauw Hall sample.....	28
Figure 3.3.	Measurement of Seebeck coefficient.....	33
Figure 3.4.	Tools for measuring Seebeck coefficient for our samples.....	36
Figure 3.5.	Carrier concentration versus Seebeck coefficient for tin oxide samples...	40
Figure 3.6.	Reflection measurements for some typical tin oxide samples.....	42
Figure 3.7.	Plasma frequency for some tin oxide films by using reflection measurements.....	43
Figure 3.8.	Ellipsometry measurements of plasma frequency for some tin oxide films.....	50
Figure 4.1.	The APCVD system we used for production of tin oxide films.....	65
Figure 4.2.	Illustration of old (a) and new (b) injector.....	68
Figure 4.3.	SEM images of sample 1mmSLG (a) and sample 1.1mmCG (b).....	77

Figure 4.4.	XRD of sample 2mmSLG before (large box) and after annealing (small box).....	78
Figure 4.5.	AFM image of sample 1mmSLG.....	80
Figure 4.6.	SEM image of sample 2mmSLG.....	81
Figure 4.7.	Transmission and reflection of some typical samples.....	82
Figure 4.8.	Transmission, reflection, and absorption of some substrates.....	84
Figure 4.9.	Absorption of tin oxide for some typical samples.....	84
Figure 4.10.	Absorption coefficient of the typical samples.....	86
Figure 4.11.	Square of absorption coefficient *Energy of the typical samples.....	86
Figure 4.12.	Absorption coefficient of sample 1mmSLG using different equations.....	87
Figure 4.13.	Absorption coefficient of samples 1.1mmCG using different equations...	87
Figure 5.1.	Plasma frequency from both ellipsometry (o) and reflection measurements (□) against carrier concentration for some tin oxide films.....	113
Figure 5.2.	Carrier concentration versus Seebeck coefficient for tin oxide samples where the straight line represents the best fitting.....	115
Figure 5.3.	Carrier concentration versus scattering parameter for tin oxide samples	115

LIST OF TABLES

Table 3-1	Ratio of the measured Hall concentration to the real concentration in the bilayer films. Carrier concentration is the same in both layers. Ratio of mobility values is assumed to be $\mu_1/\mu_2=0.1$	38
Table 3-2	Plasma frequency for different samples with different carrier concentration by using reflection measurements.....	41
Table 4-1	The range of best-applied temperature of SnO ₂ :F deposition.....	67
Table 4-2	The gas flow for the best TCO films. The location the gas flows is shown in figure 4.1:.....	69
Table 4-3	Reactive RF magnetron sputtering conditions for deposition of Al ₂ O ₃	73
Table 4-4	Annealing conditions for the substrate.	75
Table 4-5	Electrical properties of three typical samples.....	89
Table 4-6	Electrical property for two samples before and after annealing.....	90
Table 5-1	Comparison of the Hall and optical mobility values.....	117
Table 5-2	Calculated mobility as a function of dielectric constant $n=5 \times 10^{20} \text{ cm}^{-3}$; compensation degree $\beta=0$	125
Table 5-3	Calculated ratio of mobilities in compensated and non-compensated SnO ₂ for the same donor concentration, $N_d=5 \times 10^{20} \text{ cm}^{-3}$	126

ACKNOWLEDGMENT

At this opportunity, I would like to express my sincere gratitude to my thesis advisor Dr. Victor Kaydanov. His great knowledge in solid state physics in general and transport phenomena in particular gave me a good understanding in this subject. Without his contribution and cooperation, my thesis would not have been done. It is my fortune to worked with him in characterization under his guidance. In addition, his kindness and sympathy built a good friendship with him.

My deepest thanks to my co-advisor Dr. Tim Ohno who helped me a lot in many aspects despite his busy schedule. His advice and organization helped me very much in finishing this thesis. Both of my advisors built an active CdTe group.

I would like also to thank all of my thesis committee. My special thanks will be to Dr. Jianping Xi who gave me a valuable information regarding APCVD system. We spent a lot of time together in building and adjusting the system. I am very thankful to Dr. Reuben Collins for his advice and valuable discussion of my thesis and in particular optical and electrical properties. My thanks also will be to Dr. John Moore and Dr. Robert Woolsey for their serving in my thesis committee and for their advice

My thanks will extend to my former advisors Dr. John Trefny and Dr. Duli Mao, for introducing me to this subject and their advice. I am grateful to Dr. Don Williamson for his guidance in X-ray measurements and interpretation.

My special appreciation will be to my friend and colleague Angelo Gilmore (Scotty) for his extensive assistance in ellipsometry measurements. He always provided me with any service without delay or hesitation. I wish him a great life and success.

I would like to thank all of TCOs and CdTe group for their support and in particular Dr. Colin Wolden for his contribution to modeling, and Dr. Lianghuan Feng and Tingjun Wen for providing me many data and samples.

Finally, I will not forget my parents who encouraged me to continue my studies. I thank them for their good advice, support, and supplication. My special thanks to my wife for her patience, support, and backing. My thanks will be for my children (Abdulmalik, Mohmed, and Shahad) who fill my life and give me the meaning of happiness.

CHAPTER 1

INTRODUCTION

1.1 Motivation of Research

Photovoltaic (PV) solar energy conversion has the potential to become one of the major sources of power to replace those that are leading to environmental pollution. Another important reason to develop solar modules is to reduce the cost for providing power for remote locations where conventional power sources cannot be used. For a long time solar modules have been used as the power sources in space, and needs in these area increased dramatically recently because of rapidly growing numbers of commercial satellites. Polycrystalline thin film solar cells have tremendous potential for meeting the requirements of low cost and reliable PV power sources.

Since 1992, the Department of Physics of the Colorado School of Mines (CSM) has continued the research of CdS/CdTe thin film solar cells initiated by the Ametek Corp. The general approach in this research is based on combining activities aimed at improvement of cell performance and stability with the activities aimed at increasing the fundamental understanding of the properties of materials making up the cells. The relations are emphasized between structural and electronic properties of the cell components and various processing procedures. Along with the CdS and CdTe layers and the back contact

multilayer structure, the transparent conducting oxide (TCO) front contact directly impacts cell performance. Improvement of its characteristics decreases both electrical and optical losses in the cell and hence increases its efficiency. After significant accomplishments achieved in processing and studies of the first three components, which provided a considerable increase in cell performance, it was reasonable and even necessary to emphasize the front contact properties. This thesis research is devoted to development of processing and basic studies of heavily doped tin oxide thin films that are widely used as a front contact in the cells based on CdTe. These studies were started by CSM in 1996 in collaboration with Green Development, LLC, and are supported by DOE (Grant No. DE-FGO3-96 ER82183 and Subcontract No. XAK-8-17619-28 under Prime Contract No. DE-Ac 36-83CH10093).

Transparent conductive thin film oxides are important basic electronic materials that have numerous applications. TCOs were originally developed for window defrosting. Over the past 20 years large-scale TCO coated glass substrates have been applied commercially as a component in flat panel display devices, a front contact in photovoltaic modules, and heat-reflecting coatings on architectural windows. Thus developments of processing and fundamental studies of TCO thin films are important and can be beneficial not only for PV applications. Most applications require high transparency in the visible spectrum. Solar cells and flat displays also require high electrical conductivity (low sheet resistance) of the films. Today, TCOs in commercial use include tin oxide, which is

usually doped with fluorine or antimony ($\text{SnO}_2\text{:F}$, $\text{SnO}_2\text{:Sb}$), tin doped indium oxide ($\text{In}_2\text{O}_3\text{:Sn}\equiv\text{ITO}$), and zinc oxide, usually doped with aluminum (ZnO:Al) [1].

Improving TCOs is challenging because optical and electrical properties are somewhat anti-correlated - optimal performance requires a compromise between the two. Although increasing carrier concentration through extrinsic doping increases electrical conductivity, σ , it does so at the expense of decreased transparency, T , in the visible and near IR spectrum due to free carrier absorption. In the figure of merit of TCOs that is commonly used, transparency is weighted much higher than low sheet resistance [2], hence the limit for the doping level is defined by transparency and is usually in the range of $\sim 5 \times 10^{20}$ to $1 \times 10^{21} \text{ cm}^{-3}$. The carrier concentration in commercially available TCO's often approaches this limit. It is not practical to increase carrier concentration further, even if it were chemically possible. Thus the only possible way to increase σ is to improve carrier mobility, μ .

Mobility in single crystals is defined by fundamental electronic parameters, such as the effective mass of free carriers, the dominating scattering mechanism, types and density of scatters, etc. In polycrystalline thin film materials the mobility value is also influenced by structural imperfections, such as grain boundaries, specific point defects, voids, gaps, etc. All the factors that determine mobility in TCO thin films have not been investigated thoroughly or completely understood. Experimental data provided by various authors deviate widely as well as the estimations of the theoretical limit of mobility that could be achieved by optimizing the film structure and processing procedure. This situation

explains one of the major goals of our research - basic studies of SnO₂ thin films aimed at clarification of the factors that determine mobility value in real films and estimation of the theoretical limit.

A wide variety of deposition techniques have been used to deposit TCOs, such as evaporation, sputtering, spray pyrolysis, and chemical vapor deposition (CVD). In our research atmospheric pressure chemical vapor deposition (APCVD) was used to produce SnO₂ thin films. This choice was dictated by several factors:

1. CVD is considered to be one of the best techniques and is widely used for commercial applications because it is an inexpensive process in terms of the equipment costs. The reactants are available in high purity form and the dopants can be introduced easily during the deposition. APCVD is convenient and more productive for high-scale manufacturing on large area substrates.
2. An APCVD system for deposition on glass substrates of moderate size (4"x4") became available for us due to collaboration with Green Development, LCC.
3. Several specialists at CSM and Green Development, LCC, involved in these studies had experience in APCVD deposition of various materials.

Fluorine was chosen as a dopant providing the optimal carrier concentration in tin oxide because it is known from the literature that fluorine yields higher mobility and optical transmission than the other possible dopant, antimony.

Comprehensive characterization of the films prepared with APCVD and combined analysis of the structural, compositional, optical and electronic properties provided feedback for optimization of the processing procedure and the APCVD system design.

1.2 Research Objectives

According to the problems to be studied and general approach formulated above, this research had the following objectives:

- To establish the set of experimental methods that can provide the information we need on the film properties.
- To provide the tools necessary for the planned experimental studies.
- To revise and optimize processing conditions and improve the APCVD system design.
- To perform experimental studies and theoretical analysis of the fundamental properties of the electron transport in tin oxide thin films, such as electron energy spectrum in the conduction band and free electron scattering.
- To clarify the factors influencing sheet resistance and bulk mobility in the actual SnO₂ films and evaluate their importance in the sense of improvement of the film electrical properties.
- To develop recommendations regarding the directions of future studies.

1.3 Thesis Organization

Chapter 2 presents a general literature review of transparent conductive oxides, and a more specific review of tin oxide. All steps in the processing procedure optimization and the processing system improvement were based on studies of the properties of the films obtained under varying preparation conditions. Chapters 3 and 4 present technical aspects of our studies. We present the experimental methods and techniques of characterization in Chapter 3. The description of processing technology and properties of the fabricated films are presented in Chapter 4. Chapter 5 presents studies of basic electronic properties of SnO₂ thin films, which we consider as the most important part of our research. The chapter starts with the analysis of the theory of electron transport in semiconductors. The approximations and simplifications of the theory we use, were analyzed to verify their validity for a heavily doped semiconductor like SnO₂. Final formulas for the transport coefficients (Hall, Seebeck, resistivity, plasma and collision frequencies, mobility, mean free path length) were discussed to define what information on the electronic characteristics of a material can be derived from the experimental studies of transport phenomena and their combined analysis. The next portion of the chapter presents experimental results and their discussion: effective mass as a function of electron energy, influence of granular structure on material resistivity, and dominating scattering mechanism in the bulk of the grains. The chapter is concluded by comparison of the measured mobility with that calculated theoretically. Chapter 6 contains a summary of the research: major results, conclusions and recommendations.

CHAPTER 2

BACKGROUND (LITERATURE REVIEW)

2.1 General Physical Properties of TCO

A transparent conducting oxide, as indicated from its name, should have both high electrical conductivity and optical transparency in order to meet the requirement of many applications. Increasing the film thickness of the TCO will lead to increasing the conductivity but will reduce the transparency. In addition, increasing the free carrier concentration will increase the conductivity but shift the plasma edge (IR reflection) to shorter wavelength. Therefore both changes in film thickness and doping can improve one desired characteristic but at the expense of the other. To solve this contradiction, it is necessary to use a figure of merit to quantify the TCO quality. Many definitions were suggested [3] and the definition that will be used here, which is independent of thickness, is [4]:

$$\phi_{f.m} = \frac{\sigma}{\alpha} \quad (2.1)$$

where the conductivity (σ) is equal to:

$$\sigma = \frac{1}{R_{sh} t} \quad (2.2)$$

in which R_{sh} is the sheet resistance and t the thickness of the film. α represents the absorption coefficient and can be determined by calculation from the total transmission (T) and total reflection (R) of the film. Films with high figure of merit have high conductivity and a low absorption coefficient in all the wavelengths of interest.

2.1.1 Optical Properties

TCOs have a high transmittance in the visible and near-IR region. The wide band gap of the transparent conducting oxides ($E_g \geq 3.0 \text{ eV}$) is the main reason for this high transparency. For low photon energy or long wavelength (IR region), there is a high reflectivity due to excitation of the free carriers. For high photon energy or short wavelength (UV region), there is a high fundamental absorption due to the electron transitions across the band gap [5] that can be modified by Burstien-Moss shifts. These three regions are separated, as in figure 2.1, by two fundamental energies, first the band gap absorption (E_g), second the free electron plasma energy (E_p). The electron plasma is generally described using the Drude model.

2.1.1.1 Classical Drude Model

TCOs have high reflection and absorption in the near-IR region because of the free-carrier effect. This phenomenon can be explained by using the classical Drude model. Consider a crystal that consists of immobile ions and free electrons in motion due to oscillating electromagnetic field. It is shown [6] that the permittivity can be expressed as:

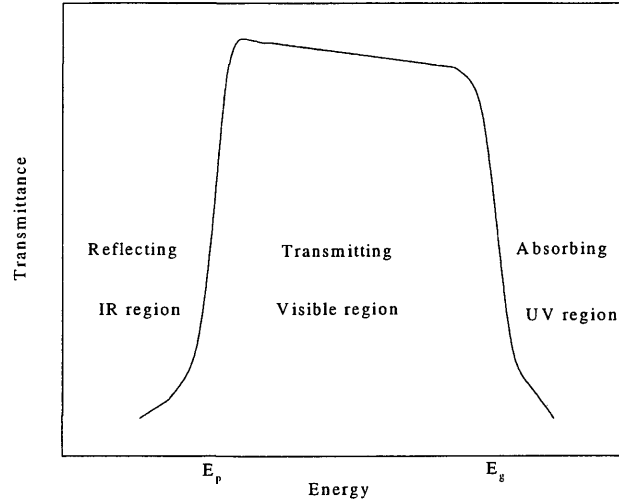


Figure 2.1. Illustration of the spectral transmittance of TCO films.

$$\varepsilon(\omega) = \varepsilon_{\infty} - \frac{4\pi n e^2 \tau}{m^* \omega} \frac{(\omega\tau - i)}{\omega^2 \tau^2 + 1} \quad (2.3)$$

where ε_{∞} is the high frequency limit ($\omega \rightarrow \infty$) and m^* is the carrier effective mass. τ is the relaxation time that results from collisions between electrons and ions, phonons, or other electrons etc. This equation can be rewritten as:

$$\varepsilon = \varepsilon_1 + i\varepsilon_2 \quad (2.4)$$

where the real part of permittivity is:

$$\epsilon_1(\omega) = \epsilon_\infty - \frac{4\pi n e^2 \tau^2}{m^*} \frac{1}{\omega^2 \tau^2 + 1} \quad (2.5)$$

and the imaginary part is:

$$\epsilon_2(\omega) = \frac{4\pi n e^2 \tau}{m^* \omega} \frac{1}{\omega^2 \tau^2 + 1} \quad (2.6)$$

For tin oxide with a sufficiently high mobility and for the high frequency range (i.e. $\omega\tau \gg 1$), the real part of ϵ can be approximated by:

$$\epsilon_1 = \epsilon_\infty - \frac{4\pi n e^2}{m^* \omega^2} \quad (2.7)$$

The plasma wavelength λ_p corresponds to $\epsilon_1 = 0$ and is equal to:

$$\lambda_p = \sqrt{\frac{\pi c^2 \epsilon_\infty m^*}{n e^2}} \quad (2.8)$$

where the relation $\omega = 2\pi c / \lambda$ has been used. Plugging (2.7) in (2.8) where $\epsilon_2 \approx 0$ near the plasma frequency will give:

$$\epsilon = \epsilon_\infty \left(1 - \frac{\lambda^2}{\lambda_p^2}\right) \quad (2.9)$$

therefore for $\lambda \approx \lambda_p$, $\epsilon \approx 0$ which implies a very low reflectance. For $\lambda > \lambda_p$, ϵ is negative and the plasma becomes reflective. Since $\lambda_p \propto n^{-1/2}$, increasing n will decrease λ_p , which results in the plasma reflection edge to be shifted to shorter wavelengths.

2.1.1.2 Burstein-Moss Effect

A degenerate semiconductor occurs when the free carrier concentration (n) is higher than the effective density of states of the corresponding band. In this case the Fermi level (E_f) lies in the band. It was observed that the optical band gap (E_{og}) of a degenerate semiconductor is wider than the fundamental (non-degenerate) band gap (E_g). For TCOs, the fundamental absorption edge lies in the UV region and shifts to a shorter wavelength as the carrier concentration increases. This phenomenon was explained independently by both Burstein [7] and Moss [8] and called the Burstein-Moss effect or blue shift. As shown in figure 2.2, filling the lowest states in the conduction band does not allow the direct transition from the top of the valance band (E_v) to the bottom of the conduction band (E_c). Instead, the transition will occur only to the empty electron levels that are above the Fermi level. As a result of this conduction band filling, the transition will also shift in the K direction. This effect is most pronounced for a conduction band with low effective mass because the Fermi level can rise significantly with increasing carrier concentration. The effective mass of electrons in undoped tin oxide and doped with fluorine is around (0.25-0.35) m_0 , which is low enough to observe this effect. The optical band gap is given by:

$$E_{og} = E_g + \Delta E_{BM} + \Delta E_{bn} \quad (2.10)$$

where ΔE_{BM} is the gap broadening due to the Burstein-Moss shift and from [7 and 8] is equal to:

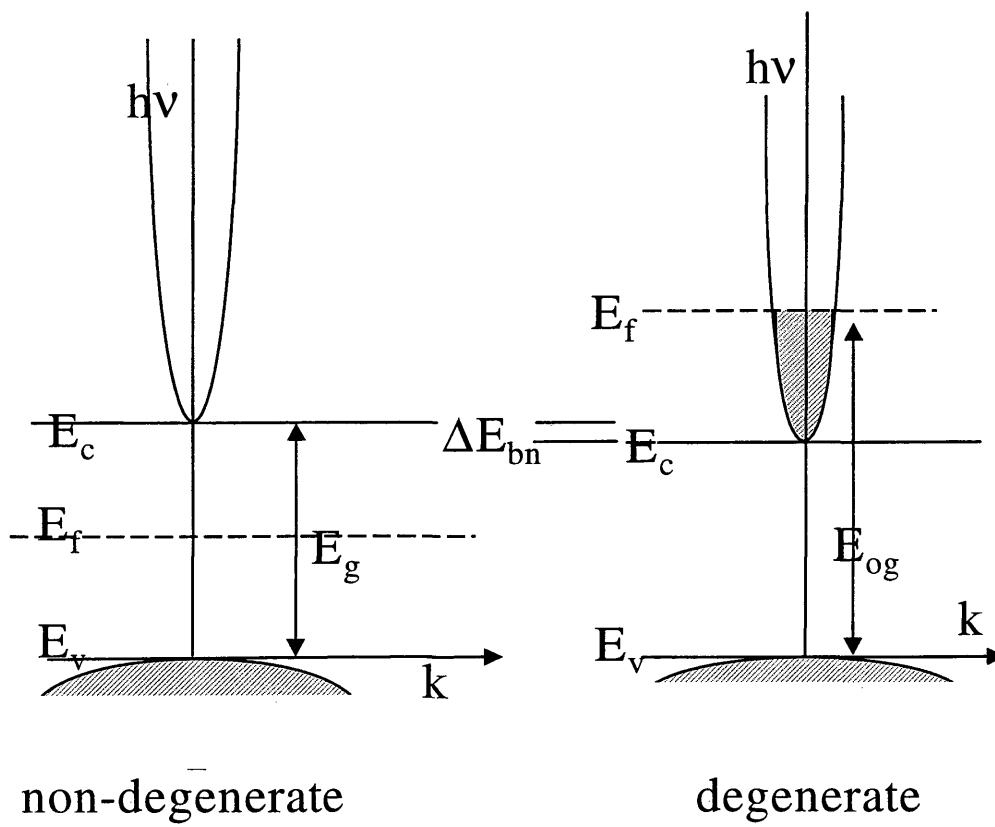


Figure 2.2. Band Diagrams for Burstien-Moss shift

$$\Delta E_{\text{BM}} = \frac{h^2}{8m_{cv}^*} \left(\frac{\pi^2 n}{3} \right)^{2/3} \quad (2.11)$$

where m_{cv}^* is the reduced effective mass and can be written as:

$$\frac{1}{m_{cv}^*} = \frac{1}{m_c^*} + \frac{1}{m_v^*} \quad (2.12)$$

where m_c^*, m_v^* are the effective masses in the conduction and valence bands, respectively. A

graph of E_{og} versus $n^{2/3}$ should provide m_{cv}^* and E_g from the slope and intercept

respectively. ΔE_{bn} is the shift due to gap narrowing. This narrowing, as shown in figure

2.2, happens at high electron concentration because of electron-electron and electron-impurity interactions.

2.1.2 Electrical Properties

The detailed theory of transport phenomena, such as conductivity and mobilities is presented in section 5.1.1. Here we present a simpler model. The electrical conductivity of a TCO is determined by the carrier concentration (n) and the electron mobility (μ) according to the relation:

$$\sigma = nq\mu \quad (2.13)$$

where q is the electron charge. Mobility can be expressed as:

$$\mu = \frac{q\tau}{m^*} \quad (2.14)$$

where τ is the relaxation time and m^* the effective mass.

From (2.13) and (2.14):

$$\sigma = \frac{nq^2\tau}{m^*} \quad (2.15)$$

It is difficult to know the highest achievable conductivity (or the lowest resistivity) in TCO without a full understanding of the mechanism behind the free carrier concentration and mobility. In order to get high conductivity, both n and μ should be optimum. This leads to another trade-off since increasing carrier concentration usually causes decreased mobility and also decreased optical transmission due to increased plasma frequency. Theoretically and experimentally, the best values for tin oxide is for n to be around $3 \times 10^{20} \text{ cm}^{-3}$ and μ to be greater than $40 \text{ cm}^2/\text{Vs}$ [5].

In pure oxide films, high carrier concentration is the main reason for high conductivity since the mobility is considerably lower than that in the corresponding bulk materials [9]. This high carrier concentration is because of the deviations from stoichiometry due to anion vacancies or excess interstitial cations [9]. Additional increase in carrier concentration can be achieved by doping with donor impurities.

Mobility of the TCO materials and its dependence on carrier concentration and temperature can be explained in terms of the scattering mechanism. There are many factors affecting the scattering mechanism but only four of them are dominant: ionized impurity scattering (μ_i), neutral impurity scattering (μ_o), phonon scattering, and grain boundary

scattering (μ_g). The observed mobility can be obtained by adding the contribution of these three scattering mechanisms reciprocally. Impurity scattering will be discussed later in chapter 5. In the case that not all the impurities, which are added to the film, are ionized, then neutral impurities will also affect the mobility. The mobility will be the reciprocal addition of both μ_i and μ_o .

For polycrystalline films, the influence of grain boundaries is usually treated in terms of “grain scattering”. If we assume that the carrier transport through the potential barriers at grain boundaries occurs by thermionic emission, then the measured mobility limited by this mechanism can be presented in the form [10]:

$$\mu_g = \frac{dq}{\sqrt{2\pi m^* k_B T}} \exp\left(-\frac{\phi}{kT}\right) \quad (2.16)$$

where ϕ is the grain boundary activation energy and d is the grain size. This can explain the increased mobility of fluorine doped tin oxide (FTO) compare to undoped tin oxide (TO). Doping TO with fluorine increases the grain size, which contributes to a decrease of the grain boundary scattering. This mobility can be analyzed by plotting a graph of $1/T$ against $\ln(\mu_g T^{1/2})$. This should yield a straight line in which the slope is equal to the grain boundary scattering potential ϕ . It is easy to show that the maximum μ_g should occur at temperature $T_m=2\phi/k_B$, provided that there is a considerable variation in the grain boundary mobility. In order for the grain boundary to be dominant, the mean free path of the electrons controlled by the impurity scattering should be in the range of the grain size or greater.

From the scattering mechanisms above, we can distinguish the controlling mechanism of our film. Measuring the relation between the mobility and temperature will help to find the effect of grain boundary scattering. Thermoelectric power (Seebeck coefficient) measurements can determine the dominant scattering through the scattering parameter (r) as discussed in chapter 3.

2.2 Review of Properties of SnO₂:F

2.2.1 Structural Properties

Tin oxide (SnO₂), which is also called stannic oxide, has a tetragonal rutile structure with six atoms per unit cell, two tin and four oxygen [11] as shown in figure 2.3. Each tin atom is surrounded by six oxygen atoms located approximately at the corners of a regular octahedron, and every oxygen atom is at the center of three tin atoms approximately at the corners of an equilateral triangle [11]. The lattice parameters are in a range: $a=b=4.737$ - 4.754 Å and $c=3.185$ - 3.205 Å with c/a ratio of 0.672 - 0.674 [11-13]. Fluorine-doped tin oxide films (FTO) retain the same rutile structure and lattice parameter as tin oxide [9]. The fluorine atoms are substitutional on oxygen sites.

Tin oxide is an insulator in its stoichiometric form, but it has unusual properties (high conductivity, high transparency in the visible region, and high reflectivity in the IR region) in the non-stoichiometric form. In the stoichiometric form, each tin atom provides four valence electrons, which are used to form bonds with oxygen atoms. In the case of the non-

stoichiometric form, the lack of oxygen will cause extra electrons in the conduction band, to form conducting tin oxide. Too little oxygen will cause formation of SnO instead of SnO₂, which degrades the conductivity.

SnO₂ has many advantages including very good adhesion to many substrates such as glass (about 2×10^7 N/m² [14]) and very good mechanical and chemical stability which precludes the problem of peeling it off mechanically or of being affected by acids or bases at room temperature [12].

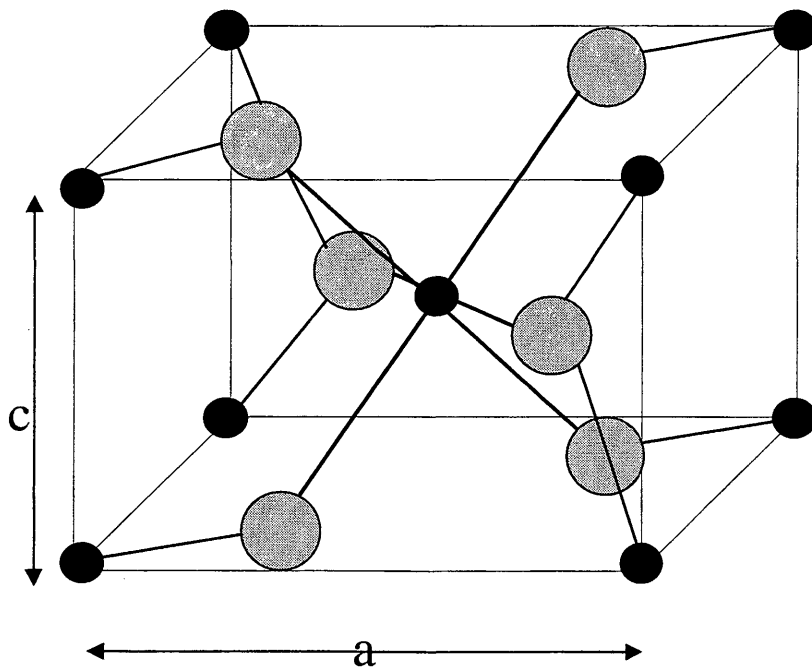


Figure 2.3 Unit cell of SnO₂ crystal where the small circles indicate tin atoms and the large circles indicate the oxygen atoms.

There is a wide spread in reported values of grain size and preferred orientation that is probably due to a strong dependence of structural parameters on the preparation conditions. For example, grain size varies from 20 nm [15] to 500 nm [13]. It is difficult to compare and analyze data of others. But we can conclude that for high substrate temperatures (400 – 600 °C) and thickness in the range of 300 to 500 nm, the typical grain size is of the order of hundreds of nm for films fabricated with CVD or spray pyrolysis.

According to Belanger [16], grain size of FTO prepared by CVD depends on the thickness, and increases linearly from 60 to 800 nm as the thickness increases from 500 to 5000 nm. Many reports [16-18] found an increasing of the grain size as the substrate temperature increase for both TO and FTO prepared by CVD. This is believed to be the main cause of decreasing resistivity as the substrate temperature increase [17]. For tin oxide prepared by CVD with thickness of 500 nm, grain size increased from 100 to 230 nm as substrate temperature increased from 300 to 500°C, but decreased to 170 nm for $T_s = 550^\circ\text{C}$ [19]. Maudes [20] found that tin oxide produced by spray pyrolysis has grain size from 240 - 320 Å for substrate temperature between 475 – 615°C and it is amorphous for temperature less than 350°C.

The wide spread of data regarding the preferential orientation of the crystallographic planes can also be due to the sensitivity of the preferred orientation to the preparation conditions. Tin oxide doped with fluorine exhibits different orientation planes parallel to the substrate depending on the temperature and thickness [9 and 21]. In general the planes

(110), (101), (211), and (200) are the most reported as the dominant planes for tin oxide films. For TO prepared by CVD, it is found that at substrate temperature T_s less than 370°C , the main peak is (101), but at 370°C the preferred orientation is (200) [12]. For FTO processed by CVD, the plane (200) is considered to be dominant at high T_s ($\geq 400^\circ\text{C}$), but for $T_s = 350^\circ\text{C}$, the structure is amorphous [21]. In terms of film thickness, the (110) plane is dominant for films that are prepared by CVD at $t = 390$ nm; however, at $t = 1650$ and 4500 nm the dominant plane becomes (200) [16]. Some studies [22] did not show any difference between the dominant plane of TO and FTO. However Prosica [17] found a preference to change from (211) to (200) plane as the Freon percentage increases from 0% to 1%. Annealing at 600 , 800 , and 1000°C for SnO_2 films deposited at 400 and 450°C will not change the preferred plane (101) and (211) respectively [23].

2.2.2 Optical and Electrical Properties

It is possible to increase the carrier concentration by replacing a -2 valence anion (oxygen) with a -1 valence fluorine atom [3]. This substitutional doping by fluorine and the absence of change in lattice constant results from the similar ionic radii of both oxygen and fluorine (the radius of oxygen is 1.32 \AA and the radius of fluorine is 1.33 \AA [24]. Furthermore, fluorine should not form compounds or solid solutions with tin oxide. Doping tin oxide with antimony affects the conduction band to a greater extent, since it replaces the tin atoms, which leads to scattering of electrons in the conduction band. This results in

reduced mobility of electrons and degraded conductivity and transparency of the film. In contrast, doping tin oxide with fluorine disturbs the filled valence band and disturbs only slightly the electron wave functions in the conduction band, because fluorine replaces the oxygen atoms. Therefore, fluorine causes the least scattering and leads to F-doped tin oxide films with high conductivity and transparency [17].

The electrical and optical properties of the oxide film depend strongly on its microstructure, stoichiometry, and the nature of the impurities present. The impurities are introduced by either intentional doping, such as with fluorine in tin oxide, or unintentional doping, usually with chlorine when tin chloride compounds are used in CVD or with sodium diffused from soda-lime glass substrates under high temperature deposition conditions (more than 350 °C). The size and the shape of the grains depend on the deposition parameters.

Many factors, such as preparation methods, deposition temperature, fluorine concentration, and film thickness, effect FTO (prepared by APCVD) structure and lead to a wide range of both electrical and optical properties.

In general, FTO films have a carrier concentration n , which increases as the amount of F increases, from about 1×10^{20} to $4 \times 10^{20} \text{ cm}^{-3}$ for thickness between 500 and 1000 nm [15]. The bulk resistivity of the film can reach as low as $5 \times 10^{-4} \Omega\text{-cm}$ [17,25,27]. The effective mass of conduction band electrons increases from $0.1 m_0$ for pure tin oxide (TO) to about $(0.27 - 0.33) m_0$ for $\text{SnO}_2\text{:F}$ [9]. Shanthi [15] found that FTO films prepared by

spray pyrolysis techniques have higher mobilities (25 - 50 cm/Vs) than TO (5 - 30 cm/Vs) while a slight decrease in the mobility was reported [27] when tin oxide is doped with fluorine.

Fluorine doped tin oxide films exhibit high transmittance in the visible range ($T \approx 80\% - 90\%$) and high reflectance in IR region between 5000 - 10000 nm ($R \approx 80\% - 90\%$). It has an optical band gap higher than that of the pure tin oxide (3.7 - 4.3 eV) [16,25,28]. The transition from high transmission to high reflection occurs at the plasma edge. The plasma edge is typically in the range 1500 - 2000 nm [11 and 16] and λ_p decreases if n increases.

$\text{SnO}_2:\text{F}$ meets the three basic criteria to be used as TCO in a CdTe photovoltaic device: high optical transmission (spectrally above the CdTe and CdS band gap), high electrical conductance, and suitable adhesion for fabrication of subsequent layers. In order to produce optimal CdTe device efficiency, the three criteria should be developed to a certain balance. The band gap energy for TO, between 3.5 - 3.7 eV, is adequate for fabricating high efficiency solar cells since it correlates to a wavelength between 330 - 360 nm, below which there is little solar irradiance.

2.2.3 Preparation Methods

A wide variety of deposition techniques have been used to deposit tin oxide films. These techniques can be classified as chemical and physical methods. Chemical methods involve a chemical reaction such as chemical vapor deposition (atmospheric and plasma)

and spray pyrolysis. Physical methods cover deposition techniques that produce thin films by evaporation or ejection of materials from a source, e.g., thermal evaporation, including close space sublimation, electron beam evaporation, and sputtering techniques. As discussed, electrical and optical properties depend strongly on the deposition techniques, and the associated deposition parameters, because of the variance in film microstructure and composition.

Sputtering methods have been used to produce tin oxide films by using a tin target in a 1:1 gas mixture of argon and oxygen at 10^{-2} Torr [29]. Tin oxide doped with antimony was deposited by electron beam from a powder mixture of SnO and Sb₂O₃ in a vacuum ranging from 5×10^{-5} to 1×10^{-3} Torr [30]. Sputtering and evaporation techniques produce films at low growth rate on the order of 0.1 nm/s [17].

In spray pyrolysis techniques, tin oxide films are prepared by using alcoholic solutions containing a suitable tin compound such as SnCl₄ and a suitable dopant. These solutions are atomized and directed onto heated substrate [17 and 31]. Tin oxide can also be produced by APCVD by passing the heated substrate under an injector in where gases are introduced and react on the substrates to form SnO₂.

Chemical vapor deposition and spray pyrolysis are considered to suitable techniques for commercial applications [12 and 31] because they are inexpensive in terms of the equipment cost, and they are convenient for high throughput, large-area depositions (high growth rate on the order of 10-100 nm/s). In addition, the reactants are available in high

purity form and the dopants can be introduced easily. CVD films have better electrical conductivity, transparency, and thickness uniformity than for the sprayed films [4].

However CVD films are reported to be poor in reproducibility and uniformity.

2.3 Summary

In this chapter, a background of transparent conducting oxide and especially tin oxide were presented. Carrier concentration and mobility are the main controlled factors in electrical properties. It was shown that carrier concentration can be increased greatly by doping but this will effect the optical properties. Mobility is the main factor to be increased for higher conductivity without effecting the optical properties. The mobility is limited and the literature values do not vary much. Structural properties change very dramatically (grain size and orientation) due to preparation parameters. It was found that increasing the temperature of the substrate leads to increase grain size. The optimum values of n are found to be between 1×10^{20} to $5 \times 10^{20} \text{ cm}^{-3}$ for mobility to be as large as possible. The transmission and reflection does not change in most of the literature and are equal to around 80% (T%) and 10% (R%) in the range of 400 to 900 nm.

CHAPTER 3

EXPERIMENTAL: CHARACTERIZATION METHODS AND TECHNIQUES

3.1 Structural Properties

3.1.1 Film Thickness and Surface Roughness

Accurate measurements of thickness and surface roughness are very important because of the dependence of optical and electrical measurement on these physical properties. Many different methods can be used for this purpose. In our routine measurements, we use a surface profiler (Tencor® P-10). In addition, ellipsometry provides a good estimation of thickness and roughness, which usually agrees with profiler measurements. We can also find the thickness by using optical measurements of two neighboring interference fringes reflectance maxima or transmittance minima. This method can be applied for samples with high thickness uniformity. It happens often that this method gives results different from those for the two previous methods.

In order to measure the sample using the profiler, a step between the substrate and the tin oxide film surface was produced by etching the tin oxide layer using a solution of 10% concentration hydrochloric acid with zinc powder. This combination produces atomic hydrogen, which attacks the stable tin oxide. The reaction is allowed to occur on the

surface of the tin oxide for approximately one minute. A position of the film is covered by a suitable tape, for step preparation. The reaction does not attack the underlying glass.

3.1.2 Grain Size and Orientation

X-ray diffraction (XRD) was used to investigate the crystalline properties of fluorine-doped tin oxide. We used x-ray (Rigaku model Ru-200) with wavelength equal to 0.1541 nm, 2θ range from 15° to 60° with 0.05° step sizes, and interval of two seconds. In addition, the preferred crystallographic planes for each sample can be found by XRD.

The grain size can be estimated by using the Scherrer formula [32]:

$$D = \frac{0.9\lambda}{B \cos(\theta)} \quad (3.1)$$

where λ is the wavelength of the diffracted beam and θ is the angle of the diffracted peak. B is the peak broadening in radians at half its maximum intensity and can be estimated from the relation:

$$B^2 = B_m^2 - B_s^2 \quad (3.2)$$

where B_m is the measured breadth of the diffraction line and B_s is the instrumental peak broadening. In our XRD, B_s equals to 0.17° for $2\theta \leq 60^\circ$.

Scanning electron microscopy (SEM) was used to show a grain image of $\text{SnO}_2:\text{F}$. In addition, we used an atomic force microscope (AFM) for imaging of grains. AFM can capture the grain in three dimensions and the roughness can be calculated.

3.2 Electrical Properties

3.2.1 Sheet resistance and Bulk Resistivity

The resistivity (ρ), sheet resistance, carrier concentration, and mobility of the TCO films can all be measured using a combination of 4-point probe, Van der Pauw method, and Hall effect measurements.

Sheet electrical resistance is one of the two most important characteristics defining the quality of TCO films; the other is the optical transmittance. Sheet resistance, R_{sh} , and bulk resistivity, ρ , were measured routinely on all the films produced, and mapped over the film area. For these measurements the four-point probe method was used (see Figure 3.1).

Distance between neighboring collinear electrode tips was the same, $s=1$ mm. Thus the area characterized with each measurement was of the size about $3 \text{ mm} \times 3 \text{ mm}$, while the sample area was usually of $100 \times 100 \text{ mm}^2$. Current, I , enters the sample through probes 1 and 4, and voltage, V , is measured between probes 2 and 3. According to the general theory [33], if the sample sizes in all three dimensions are much greater than the interprobe distance (semi-infinite medium approximation), the bulk resistivity of a material can be calculated as

$$\rho = 2 \pi s (V/I), \quad (3.3)$$

If the samples cannot be considered as semi-infinite at least in one dimension, Eq. (3.3) must be corrected for finite geometry. For an arbitrary shaped sample the resistivity is given by

$$\rho = 2 \pi s F (V/I), \quad (3.4)$$

where F is a correction factor, which corrects for edge effects, for thickness effects, and for probe placement effects. For our samples, the film thickness is much lower than the probe spacing, $t \ll s$, the sample sizes in the two other dimensions are much greater than the distance between the probes; the probes were placed on the film surface not closer than $4s$ to its edge. Under these conditions correction factor is:

$$F = (t/s)(2\ln 2)^{-1},$$

and resistivity is calculated as

$$\rho = (\pi/\ln 2) t V/I = 4.532 t V/I, \quad (3.5)$$

It is seen that to determine bulk resistivity, one needs also to measure the film thickness. Sheet resistance, R_{sh} , is defined as a resistance of a square-shaped piece of the film (it is the same for any square size). It is defined as $R_{sh} = \rho/t$ and hence can be determined from the four-point probe measurements using the formula:

$$R_{sh} = 4.532 V/I \quad (3.6)$$

For four-point probe measurements we used an Alessi Model A 4P Series Four Probe Head, Keithly 225 current source and Keithly 181 Nanovoltmeter. The results of repeated measurements on the same sample were highly reproducible. It should be mentioned also that the measurements were not destructive and could be applied to samples of arbitrary shape and sizes unless the latter were too small (comparable to the four-point probe head).

For the sheet resistance and bulk resistivity measurements we also used another method and technique which will be described below together with the Hall coefficient and Hall mobility measurements.

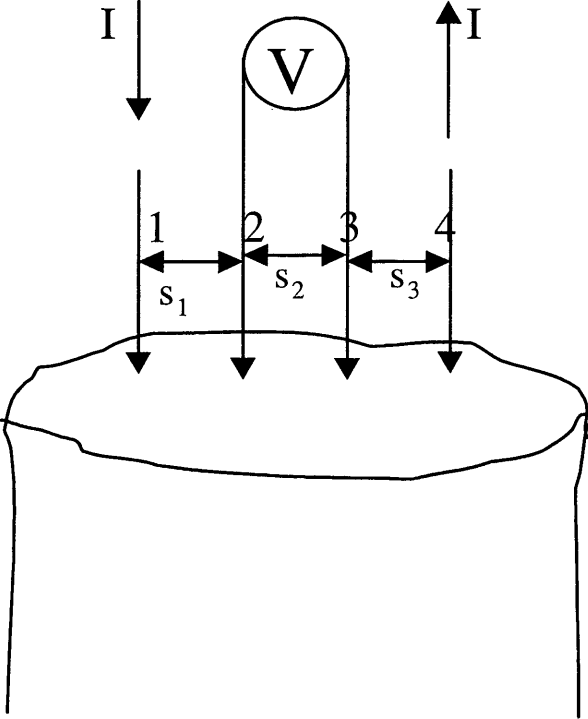


Figure 3.1. A collinear four-point probe.

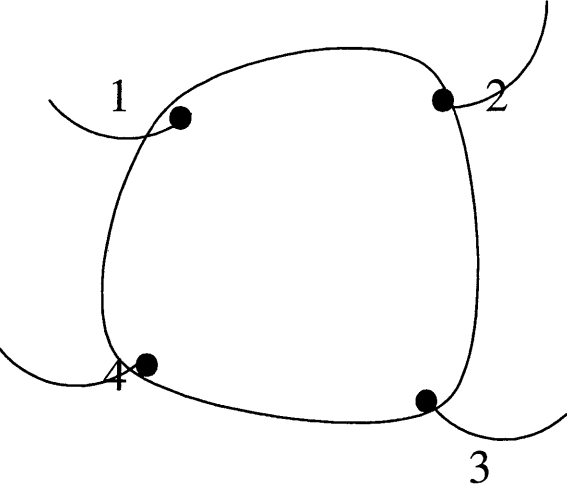


Figure 3.2. A lamella-type van der Pauw Hall sample.

3.2.2 Hall Effect

Measurement of the Hall effect is the most direct and common method used to determine the carrier concentration in semiconductors. The physical nature of the effect is as follows. Let us consider a rectangular prism of an isotropic and spatially uniform semiconductor with the electric field E_x applied parallel to one of its edges. The electric current, I_x , which is flowing in the same direction, will be deflected along the y-axis after the magnetic field, B_z , is applied to the sample. If the electrical circuit is disconnected in the y-direction, then this transverse current will charge the opposite sides of the sample providing an electrical field E_y . This field creates the transverse current in opposite direction, so that in the stationary state $I_y=0$.

For the isotropic and uniform medium the Hall effect is described by the equation:

$$E_H \equiv E_y = R_H j_x B_z, \quad (3.7)$$

where E_H is the Hall electric field, j_x is the x-component of the current density, and R_H is the Hall coefficient which is related to the free electron concentration, n , in the n-type material by the equation:

$$R_H = -A_H/q n$$

Here q is the electron charge magnitude and A_H is the so called Hall factor, a numerical coefficient which varies in a narrow range around 1 depending on the specific features of the band spectrum, electron gas degeneracy degree, and scattering mechanism. It will be shown in Chapter 5 that for the heavily doped SnO_2 with strongly degenerate electron gas, the Hall

factor, A_H , is equal to 1, and hence the free electron concentration can be determined exactly from the Hall coefficient measurement:

$$n = -(qR_H)^{-1} \quad (3.8)$$

We used for this purpose a Bio Rad HL 5500 PC Hall Effect Measurement System, which is based on the van der Pauw method. This method (see [33]) was developed for irregularly shaped samples and is usually used for characterization of semiconductor wafers or thin films. A lamella-type van der Pauw sample with the attached electrical probes is shown at Figure 3.2. If the current, I , flows through the probes 1 and 2, and voltage, V , is measured between the probes 3 and 4, then the Hall coefficient is determined by

$$R_H = t \Delta V / (2B I), \quad (3.9)$$

where $\Delta V = V(\text{for } +B) - V(\text{for } -B)$, that is difference in V values measured for two opposite polarities of the magnetic field which is directed normal to the film/wafer plane.

The film resistivity is also measured by the same system and is given by

$$\rho = 0.5 (\pi t / \ln 2) (R_{12,34} + R_{23,41}) \quad (3.10)$$

for the symmetrical samples like circles or squares. Here $R_{12,34} = V_{3,4} / I$ (voltage is measured between contacts 4 and 3, while current enters the sample through contact 1 and leaves through contact 2). $R_{23,41}$ is similarly defined. We performed R_H and ρ measurements on the square shaped samples $1 \times 1 \text{ cm}^2$ cut from the whole $4 \times 6 \text{ cm}$ sample. Contacts were provided by copper wires soldered with indium/tin pellets to the corners of the sample. The size of the contact spots was made as small as possible, less than 0.5 mm, to increase the accuracy of measurements which drops as the ratio of the contact area to the sample area increases.

Accuracy also drops if the contact is shifted from the circumference toward the center of the sample. The Hall mobility in the van der Pauw geometry is given by the same expression as the bar geometry, namely by

$$\mu_H = |R_H|/\rho \quad (3.11)$$

Because the Hall factor in our material is equal to 1, the Hall mobility in a single crystal is equal to the drift mobility. Indeed, $|R_H| = (qn)^{-1}$ and $1/\rho = \sigma = q \cdot n \cdot \mu$. In the case of a polycrystalline material and for samples with some defects like microcracks, voids, etc., the measured value of resistivity can be higher than that for the single crystal. Hence the Hall mobility can be lower than the real mobility inside the grains. This issue will be discussed later in this chapter and also in Chapter 5.

3.2.3 Seebeck Effect (Thermopower)

Measurements of the Seebeck coefficient, S , which defines the material properties with respect to the Seebeck effect (thermopower), are also used to determine the carrier concentration. The Seebeck coefficient value depends on carrier concentration, but not as simply as the Hall coefficient. The expression for S includes other fundamental parameters such as an effective mass and scattering parameter, which must be defined with some independent methods. It is practical to establish empirically the $S(n)$ dependence for the given material on a series of samples with varying n values determined by the Hall effect measurements. Once this correlation is established reliably, it can be used for concentration measurements by means of the Seebeck effect instead of the Hall effect. The advantages of

this method will be discussed later. Our comparative studies of the Hall and Seebeck coefficients were aimed both at obtaining the correlation curve and at basic studies of band parameters and scattering mechanisms in our material.

The physical nature of the Seebeck effect can be explained as follows. If a temperature gradient, ∇T , is applied to a sample, free electrons migrate (diffuse) from its hot edge to the cold one, charging the former positively and the latter negatively. Thus the Seebeck electric field appears which causes electrons to drift in the opposite direction of the diffusion current. If the electric circuit is disconnected, diffusion and drift electron flows compensate each other, so that a stationary state is established with no net current. Under this condition the Seebeck effect is described by the equation:

$$\mathbf{E} = S \cdot \nabla T, \quad (3.12)$$

where S is the Seebeck coefficient of the sample material.

To observe the Seebeck effect and measure the Seebeck coefficient, one must assemble the electrical circuit as in Figure 3.3. The sample of the material under investigation (1 in Figure 3.3) is connected with two conductors of a different material (2), which is usually a metal or alloy with a well-defined S coefficient. These two conductors are connected to the high-input resistance voltmeter, which provides the condition $I \approx 0$. Contacts of the conductors with a voltmeter are maintained at the same temperature (usually the room temperature), so that $T_c = T_d$. The junctions between materials 1 and 2 are maintained at different temperatures: $T_b \neq T_a$. The measured signal is defined by

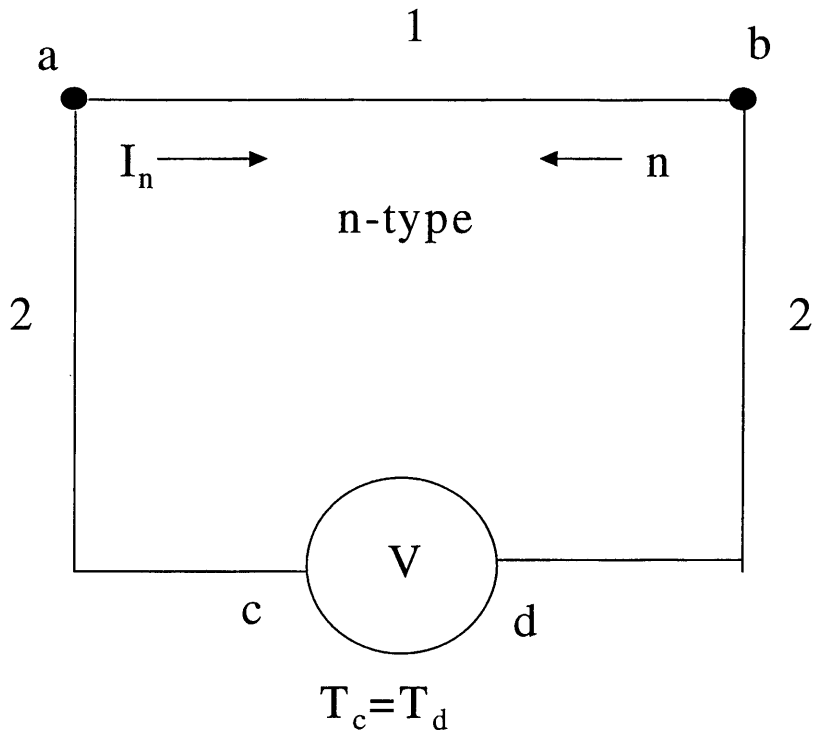


Figure 3.3 Measurement of Seebeck coefficient.

$$\begin{aligned} \Delta V = V_d - V_c &= \int_d^c \mathbf{E}(x) dx = \int_d^c \mathbf{S}(x) \frac{dT}{dx} dx = \int_{T_d}^{T_b} S_2(T) dT + \int_{T_b}^{T_a} S_1(T) dT + \int_{T_a}^{T_c} S_2(T) dT \\ &= \int_{T_b}^{T_a} S_1(T) dT + \int_{T_a}^{T_b} S_2(T) dT = \int_{T_b}^{T_a} [S_1(T) - S_2(T)] dT \end{aligned} \quad (3.13)$$

For a small temperature difference between junctions "a" and "b", Eq.3.12 can be rewritten:

$$\Delta V = [S_1(\langle T \rangle) - S_2(\langle T \rangle)](T_a - T_b), \quad (3.14)$$

where $\langle T \rangle = 1/2 \cdot (T_a + T_b)$ is an average temperature of the sample of material 1.

From the consideration above the following conclusions can be made:

- (a) The Seebeck effect can be observed only if the circuit consists of two different materials; indeed, $\Delta V = 0$ if $S_1 = S_2$.
- (b) Only those regions of the samples contribute to the measured Seebeck voltage where $T_a - T_b \equiv \Delta T \neq 0$.
- (c) It does not matter how the temperature gradient is distributed within the sample; the voltage measured depends only on the temperature difference between the junctions. That means that the measurements can be performed on the sample of an arbitrary shape, non-uniform thickness, etc.
- (d) the Seebeck coefficient for the material under investigation (1 in Figure 3.3), $S_1 \equiv S_m$, can be determined only with respect to the material of the reference electrodes (2 in Figure 3.3) with $S_2 \equiv S_r$:

$$S_m = \Delta V / \Delta T + S_r \quad (3.15)$$

For this reason one must use a material with a well-defined and stable Seebeck coefficient for the reference electrodes.

Based on these conclusions we have designed and constructed some rather simple equipment for measuring the Seebeck coefficient on the thin films of TCO deposited on

insulating substrates (glass). Figure 3.4 presents the tools and the principal scheme of the measurements. Two massive copper blocks are placed on the film surface at some distance from each other. One of the blocks is supplied with a heater, which provides its heating above room temperature. The temperature of the other block is lower and does not differ remarkably from room temperature because of very low thermal conductivity of glass and high heat capacitance of the block. The temperature difference between the blocks is measured by means of the type-E differential thermocouple and auto-ranging microvoltmeter DMM (Keithly 197A). ΔT was maintained in the range about 10°C . For the Seebeck voltage, ΔV , measurement, the copper blocks were connected with copper wires to the high input resistance microvoltmeter (Keithly 192 programmable DMM). The Seebeck coefficient of the film material S_m was determined by using Eq. 3.15 with the reference electrode (copper) Seebeck coefficient $S_r=S_{\text{Cu}}=2.09 \mu\text{V}/^{\circ}\text{K}$ [34 and 35].

Massive copper blocks due to their high weight provided good electrical and thermal contact between them and underlying film area. The latter was equipotential and isothermal. That means that we measured Seebeck coefficient of the material between the edges of the blocks. Locality of the measurements was defined by the distance between blocks and usually did not exceed 5 mm. To check how the cylindrical shape of the blocks influences the results of measurement, we performed measurements on the same films using rectangular copper blocks placed on the film surface so that the edges of the blocks were parallel to each other. No remarkable difference in the results was observed. Relocating the copper blocks on the film surface allowed us to map the Seebeck coefficient over the sample

area. It was a method to check the lateral uniformity of the film properties in addition to mapping of sheet resistivity.

To verify accuracy of the Seebeck coefficient measurements using our equipment we used foils of standard materials: constantan and nickel. Measurements at different ΔT , from 5 to 20°C, were in a good agreement with each other and obtained values of S within less than 1% of the handbook data [36-38].

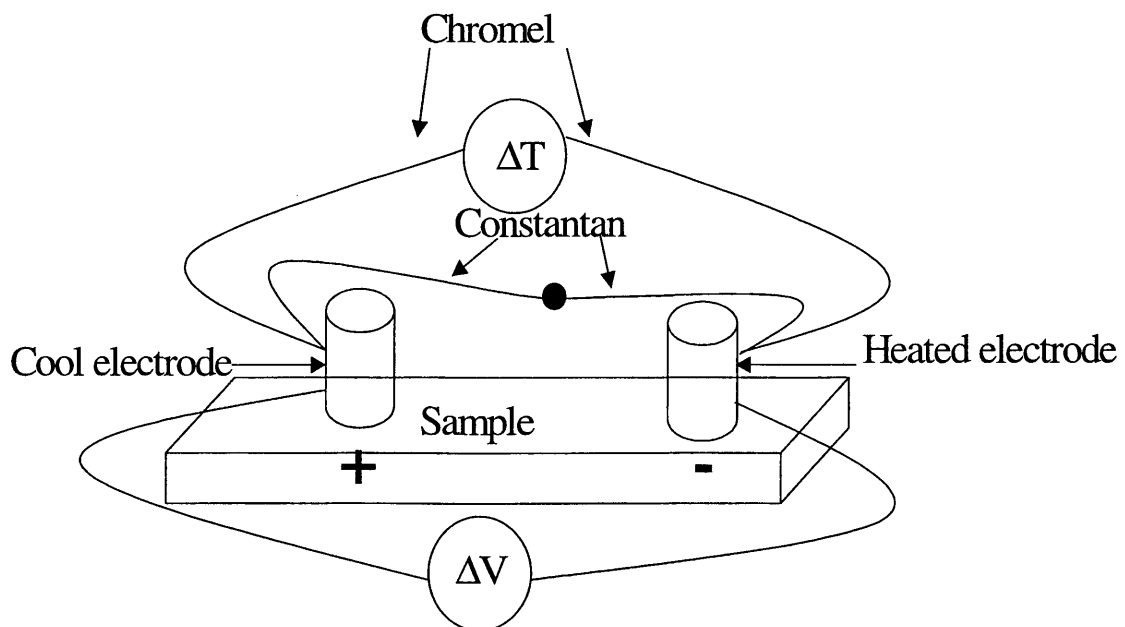


Figure 3.4 Tools for measuring Seebeck coefficient for our samples.

To obtain the dependence $S(n)$ we selected the samples with high spatially uniformity, both over the sample area and across the film thickness. The first one was checked by mapping sheet resistivity (four-point probe method) and the Seebeck coefficient. The second one was estimated by ellipsometry measurements (see Sec. 3.3.2). The model we used for treating the raw ellipsometry data provided an opportunity to detect the non-uniformity in plasma and collision frequencies, which depend on carrier concentration and mobility, respectively.

To demonstrate the importance of uniformity, let us consider a film with a uniform carrier concentration distribution and a mobility that is varying across the film thickness (see [39]). The measured Hall and Seebeck coefficient can be written in a form

$$R_{HM} = -1/q \cdot \langle n \cdot \mu^2 \rangle / \langle n \mu \rangle^2$$

$$S_M = \langle S(n) \cdot n \cdot \mu \rangle / \langle n \cdot \mu \rangle$$

Here $\langle \dots \rangle$ symbolizes averaging over the film thickness:

$$\langle F(z) \rangle = \frac{1}{t} \int_0^t F(z) dz,$$

where z is a coordinate of the point on the axis perpendicular to the film plane, and t is the film thickness. Because carrier concentration is constant, which means that S is also constant to the first approximation, expressions for R_{HM} and S_M take form:

$$R_{HM} = - (1/qn) \cdot \langle \mu^2 \rangle / \langle \mu \rangle^2$$

$$S_M = S(n) \cdot \langle \mu \rangle / \langle \mu \rangle = S(n)$$

We have found that mobility measured on thin films, $t \leq 100$ nm, were much lower (up to the order of magnitude) than mobility measured on thick films with $t \sim 500$ nm. A possible reason is the poorer morphology of very thin films. If the morphology of the bottom layer does not change or changes slightly while deposition continues, a thick film can be considered approximately as a two-layer structure: the bottom layer of low mobility μ_1 , and thickness t_1 , and the top layer of high mobility μ_2 and thickness t_2 . For this two-layer structure

$$R_{HM} = -\frac{1}{qn} \frac{(1 + t_1/t_2)[1 + (\mu_1/\mu_2)^2(t_1/t_2)]}{[1 + (\mu_1/\mu_2)(t_1/t_2)]^2}$$

Let us assume that $\mu_1/\mu_2=0.1$ and vary the relative top layer thickness. Table-3.1 presents the ratio of the Hall concentration derived from the Hall coefficient measurement to real concentration, n_H/n , as a function of t_2/t_1 .

Table 3-1 Ratio of the measured Hall concentration to the real concentration in the bilayer films. Carrier concentration is the same in both layers. Ratio of mobility values is assumed to be $\mu_1/\mu_2=0.1$

t_2/t_1	0.0	0.02	0.05	0.1	0.2	0.5	1.0	2.0	5.0	10.0
n/n_H	1.0	2.12	2.80	3.025	2.8	2.12	1.67	1.37	1.16	1.08

It is seen from the table that the measured Hall concentration could be considerably lower than the real concentration while the measured Seebeck coefficient corresponds to the

real concentration. It could be easily shown that for constant mobility and varying carrier concentration the measured Hall concentration will be equal to the average concentration in the film, while the measured Seebeck coefficient will correspond to concentration lower than the average one, or the Hall concentration, if $S \propto n^\alpha$, and $\alpha > -0.5$. For $\alpha < -0.5$, the measured S value will correspond to the concentration higher than the Hall one (see [39]). If both carrier concentration and mobility vary over the film thickness, one can obtain the experimental S(n) dependence, which can deviate considerably from that for the uniform material, or a significant spread of the experimental points around the latter.

The results of comparing the Seebeck coefficient data with the Hall carrier concentration are presented in Figure 3.5. After obtaining this dependence we used it for measurements and mapping the carrier concentration over the film area.

3.3 Optical Properties

3.3.1 Spectrophotometer: Transmission, Absorption, and Reflection Spectra

The spectrophotometer (Cary 5G UV-Vis-NIR) used in our studies has a wavelength range from 250 nm to 2500 nm, which can be extended in the IR region by installing additional accessories. Both the total and diffused component of reflectance can be measured for transmission and reflection by using a different position of the sample port and an integrating sphere. The Spectrophotometer consists of two incident light beams (sample and reference), an integrating sphere, and a detector. There are two sources of beams: a

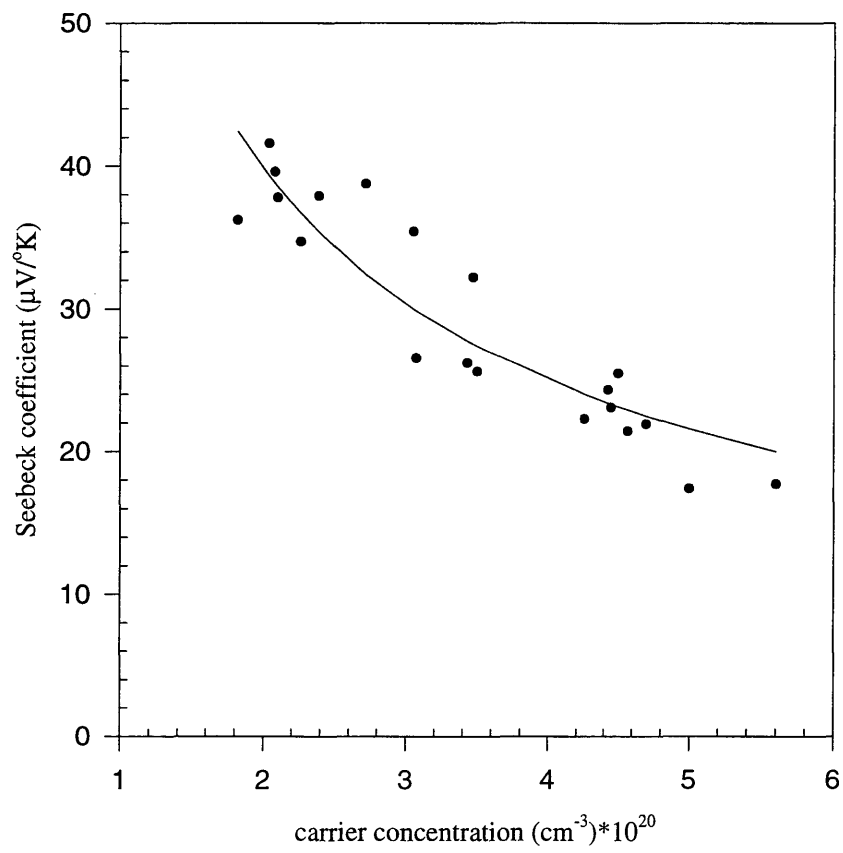


Figure 3.5 Carrier concentration versus Seebeck coefficient for tin oxide samples.

quartz halogen lamp for visible/IR region and a deuterium lamp for UV region. These beams have a full dimension (13×5 mm) and can be reduced to 9×5 mm. The UV-Visible detector is R298 photomultiplier tube while NIR detector is an electro-thermally controlled lead sulfide photocell.

In the infrared region (high wavelength or low energy), there is a high reflection due to excitation of free carriers. This occurs at wavelength higher than the plasma wavelength. A graph of energy (E (eV)= $1240/\lambda$ (nm)) against reflectance will provide a sharp increase in the infrared region in which the extrapolation of the curve to zero reflectance will be approximately at the plasma frequency (in eV units). Figure 3.6 presents reflection measurements of different samples with different carrier concentrations. From the figure, we were able to estimate the plasma frequency of each sample as in table 3-2. It should be noticed that the plasma frequency shifts to higher energy (shorter wavelength) as the carrier concentration increases, which is in agreement with the Drude model. Most of the reflectance measurements provide a good agreement with ellipsometry measurements.

Table 3-2 Plasma frequency for different samples with different carrier concentration by using reflection measurements.

sample #	carrier concentration ($\times 10^{20}/\text{cm}^3$)	plasma frequency (eV)
1	4.43	0.75
2	3.07	0.65
3	2.72	0.60

2D Graph 1

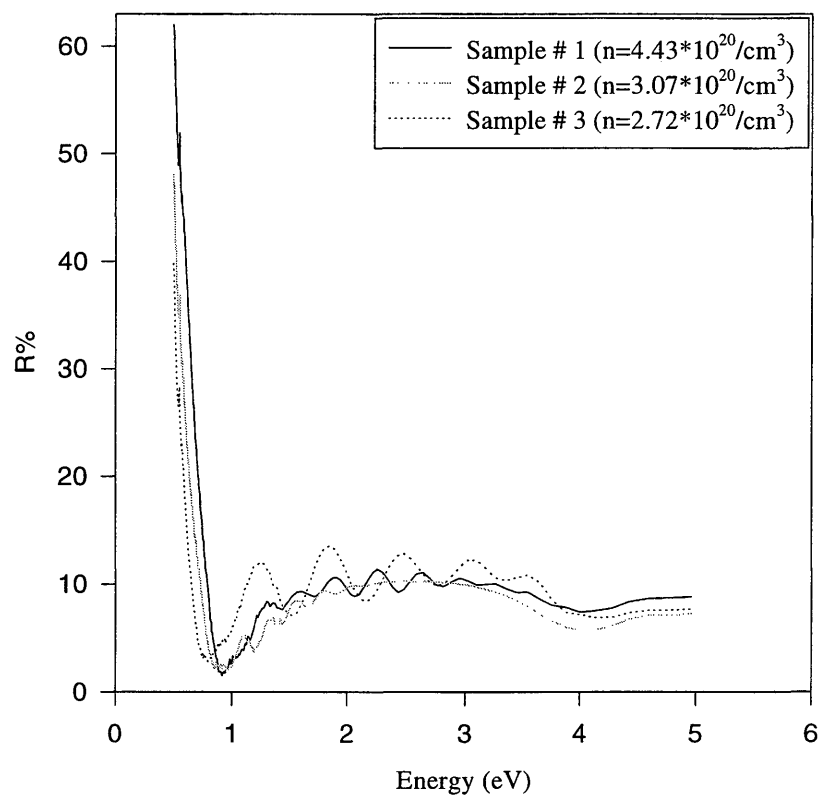


Figure 3.6. Reflection measurements for some typical tin oxide samples.

As we did before for $S(n)$ dependence, a graph of carrier concentration measured by the Hall method against plasma frequency squared measured by reflection provides us a straight line as shown in figure 3.7. This indicates that the effective mass does not depend on carrier concentration in our range (1×10^{20} - $5 \times 10^{20}/\text{cm}^3$) which supports our assumption of the parabolic band structure (see chapter five).

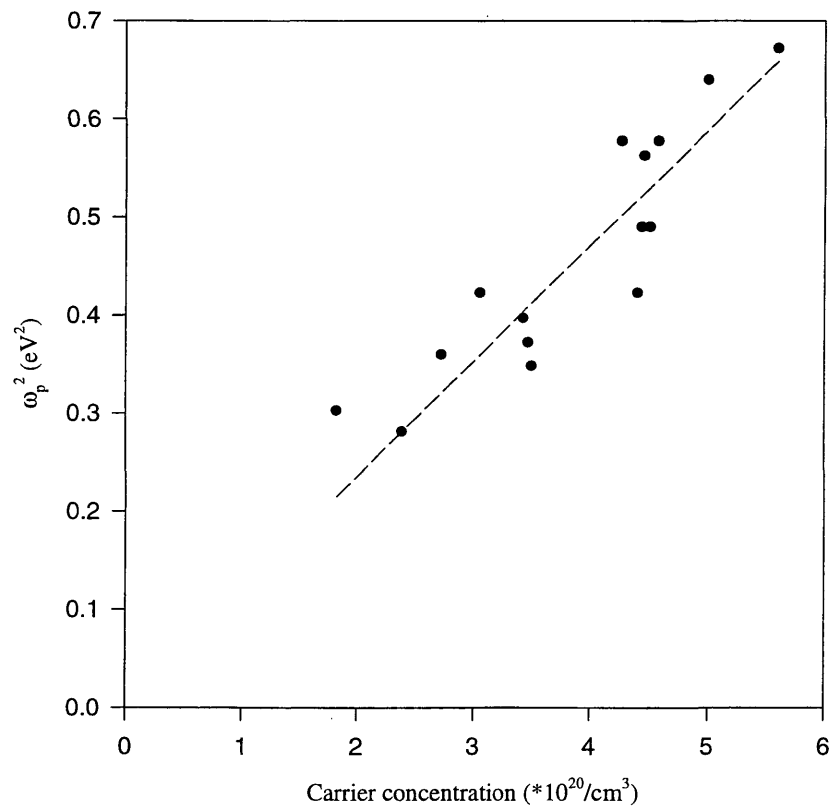


Figure 3.7. Plasma frequency for some tin oxide films by using reflection measurements.

Carrier concentration can be calculated from plasma frequency by using equation (2.8) where m^* and ϵ_∞ can be found for tin oxide either from any reference data, or by using the empirical dependence presented by figure 3.7. This simple and nondestructive method provides measurements (estimate) of carrier concentration. The limit on this method comes from the limitation of our wavelength range in the IR region (2500nm). As mentioned, uncertainty in the values of m_c^* and ϵ_∞ will effect the accuracy of carrier concentrations obtained by this method.

From transmission (T) and reflection (R) measurements, it is possible to calculate the absorption coefficient (α). There are many different relations between α , T, and R. The more accurate relation between T, R, and α which we will use [40 and 41] is

$$T = \frac{(1 + T - R)^2 e^{-\alpha t}}{(1 + T)^2 - R^2 e^{-2\alpha t}} \quad (3.16)$$

The diffused component (T and R) is assumed to be very small compared with the specular component. For films with low optical transmission and $\alpha t \gg 1$, which is true in the region around the band gap, the absorption coefficient can be calculated by using the relation:

$$T = (1 - R)^2 e^{-\alpha t} \quad (3.17)$$

3.3.2 Ellipsometry: Dielectric Constant, Plasma Frequency, and Collision Frequency

A variable Angle Spectroscopic Ellipsometer (a © J. A. Woollam Co. Inc. VASE® system) was used for our samples measurements. Several angles of incidence (usually 65°, 70°, and 75°) and a large range of wavelengths (usually 280nm to 1700nm with 10nm

increments) generated a large amount of data for more accurate results. Ellipsometry is based on measuring the change on polarization state of the reflected light from the surface of the sample.

The total electric field vector can be presented by [33]:

$$E = E_p \hat{p} + E_s \hat{s} \quad (3.18)$$

where E_p and E_s are the parallel and perpendicular (to the plane of incident) components of the electric field. We can introduce the reflectance coefficient R_p as the ratio of the reflected E_p to the incident E_p and the reflectance coefficient R_s as the ratio of the reflected E_s to the incident E_s . From these two coefficients, we can define the ellipsometric angles ψ and Δ as follow

$$\rho = \frac{R_p}{R_s} = \tan(\psi) \exp(i\Delta) \quad (3.19)$$

$$\text{or } \psi = \tan^{-1}(R_p / R_s) \quad (3.19a)$$

$$\text{and } \Delta = \Delta_p - \Delta_s = \text{differential phase change} \quad (3.19b)$$

These two measurable angles are the most commonly used in ellipsometry and usually can be determined by using what is called null ellipsometry (source - polarizer - compensator - sample - analyzer - detector).

There are many different models [42 and 43] that correlate these angles, Fresnel coefficient, complex dielectric constant or index of refraction (real and imaginary part), and/or thickness. Designing a particular model that fits the characterization of the sample,

and fitting its optical constants to the raw data obtained from ellipsometry; we can then obtain the desired information on film thickness and the optical properties of each layer in the sample. Unknown parameters in the model can be varied until a best fitting is obtained which minimize the root mean square error (RMSE) between the created model data and the raw data.

There are many layers involved for the TCO samples characterized in this method: the glass substrate, the tin oxide layer, the rough layer on the surface and sometimes the diffusion barrier between the glass and tin oxide. In order to eliminate back surface scattering which complicates the model, the backside of the substrate was roughened using sandpaper until opaque. The TCO roughness layer was simulated using 50% of the surface material and 50% voids. Using several angles of incident beam along with a wide range of wavelengths generates a large amount of data that leads to a higher accuracy fit of the model describing the sample. Increasing the number of layers of a sample will result in complicated models.

Using a Drude model for the SnO₂ layer, the plasma frequency and collision frequency can be obtained, which can be used to estimate the carrier concentration and the mobility of the sample. Since the SnO₂ layer properties can change throughout the material, a linearly graded Drude model from the bottom to the top of the layer was used in most cases. This can yield different carrier concentrations and mobilities for the top and bottom of this layer. The parameters allowed to vary in the Drude model were the thickness of the SnO₂ and roughness layers, along with ω_c , ω_p , and ϵ . If a diffusion barrier

was present, then its thickness could also vary. The optical constants of the glass substrate were determined separately and not allowed to vary. The main model used was a linearly graded Drude model, but a second slightly simpler model was also used. The second model involved only a single Drude model to which was added a linearly graded void percentage from the bottom to the top of the samples.

Finding ϵ_1 and ϵ_2 from ellipsometry, we can use Drude model as in chapter 2 to get:

$$\epsilon_1 = \epsilon_\infty - \omega\epsilon_2 / \omega_c \quad (3.20)$$

A plot of ϵ_1 versus $\omega\epsilon_2$ gives a straight line and can be used to obtain ϵ_∞ and ω_c from the slope and intercept respectively. From equation (2.5) and (2.8) we can write:

$$\epsilon_1 = \epsilon_\infty - \frac{\omega_p^2 \epsilon_\infty}{\omega^2 + \omega_c^2} \quad (3.21)$$

A plot of ϵ_1 against $\frac{1}{\omega^2 + \omega_c^2}$ will be a straight line in which the slope will provide us with the plasma frequency.

ϵ is related to the index of refraction (n) and extinction coefficient (k) as follows:

$$\epsilon(\omega) = (n + ik)^2 \quad (3.22)$$

From equations (2.4) and (3.22) we have

$$n^2 - k^2 + 2ink = \epsilon_1 + i\epsilon_2$$

which leads to $\epsilon_1 = n^2 - k^2$ and $\epsilon_2 = 2nk$

Solving these two equations leads to:

$$n = \sqrt{\frac{\epsilon_1}{2} + \frac{1}{2}\sqrt{\epsilon_1^2 + \epsilon_2^2}} \quad (3.23)$$

and

$$k = \sqrt{\frac{1}{2}\sqrt{\epsilon_1^2 + \epsilon_2^2} - \frac{\epsilon_1}{2}} \quad (3.24)$$

From these two equations, it is possible to calculate n and k as functions of wavelength λ , which leads to the determination of the reflectance and absorbance of a surface [15]. What we have to know is only the carrier concentration n , effective mass m^* , ϵ_∞ , and mobility μ . As indicated before, the mobility correlates with relaxation time τ by the relation $\tau = \mu m^*/e$. ϵ_∞ can be measured by the high frequency capacitive response.

For a normal incident electromagnetic wave from vacuum into absorbing medium, the Fresnel reflection coefficient can be found to be [43]

$$r = \frac{1 - n + ik}{1 + n - ik} \quad (3.25)$$

which gives, for reflectance of the surface

$$R = rr^* = \frac{(1 - n)^2 + k^2}{(1 + n)^2 + k^2} \quad (3.26)$$

For multi-layer films, such as tin oxide with diffusion barrier on top of absorbing glass, a very complicated formula can be found for T and R [43].

Carrier concentration can be found for a heavily doped semiconductor in the near infrared region (Drude theory) as:

$$n = \frac{m_c^* \epsilon_\infty}{4\pi q^2} \omega_p^2 \quad (3.27)$$

where m_c^* is the “effective mass of conductivity, or electric susceptibility effective mass”

and q is the charge of the electron

The mobility of the carriers is calculated from the collision frequency (ω_c) by means of the equation:

$$\mu = \frac{q}{m_c^* \omega_c} \quad (3.28)$$

It should be mentioned that this mobility, which is determined from ellipsometry data, is a characteristic of the film substance and is not influenced by the presence of inter-grain boundaries, voids, or micro-cracks.

There are many sources of errors in determining n and μ from ellipsometry. The applied fitting model can change the results (sometimes up to 20%). The error in using the correct effective mass of conductivity can also add a reasonable error in our calculation. In addition, the non-homogeneity between the top and bottom of the sample can give different results, differing by as much as a factor of 2.

Characterization of TCOs by VASE is consistent with numerous other methods of characterization applied here. Ellipsometry not only confirms what can be measured by other means, but also adds its own unique aspects of characterization including variation of optical properties over single film thickness. Ellipsometry is in general a non-

destructive characterization method, which can in many cases easily be adapted to in-situ measurements to monitor film growth.

By using this technique, many samples were measured and compared with other measurements. We draw a graph of carrier concentration measured by Hall measurement against the square of plasma frequency measured by ellipsometry. As in figure 3.8, a linear relation between these values indicate that the effective mass does not depend on carrier concentration in our range (1×10^{20} - $5 \times 10^{20}/\text{cm}^3$) which supports our assumption of the parabolic band structure.

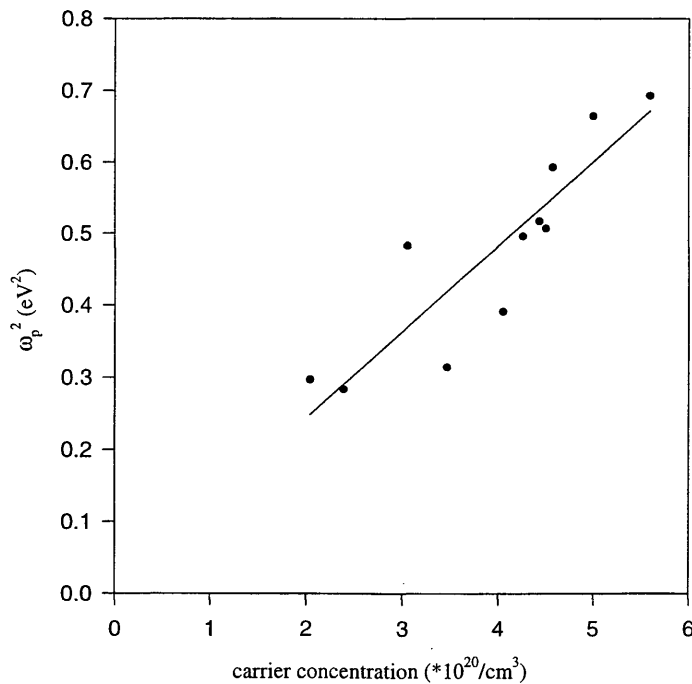


Figure 3.8. Ellipsometry measurements of plasma frequency for some tin oxide films.

3.4 Comparison of Different Methods of Characterization

For high scale manufacturing of TCOs, routine testing techniques include sheet resistance and spectral transmission measurements. At the stage of research and development one needs much more detailed information on the properties of the films in connection with the varying preparation conditions. For example, the grain size and the roughness of the film surface influence not only optical and electrical properties of the film but also performance and stability of the devices fabricated on the TCO-coated substrate. Then, optical and electrical properties are always correlated, and in general optimal performance requires a compromise between the two. For applications where high transparency and conductivity are required, the Drude theory of free electrons can be used to show that it is desirable to maximize the ratio of electron mobility to carrier concentration. Measurements of sheet resistance or even bulk resistivity themselves do not allow us to separate these parameters, and we need additional measurements. Resistivity in polycrystalline materials can be greatly influenced by the presence of the grain boundaries, gaps between grains, voids, etc. It is desirable to estimate the influence of these factors. It was shown above that various methods and techniques can be used for determination of the same parameters, e.g., the Hall and Seebeck effects and plasma frequency for measurement of the free carrier concentration, or Hall plus resistivity and collision frequency for determination of the carrier mobility, etc. In this section we will compare various methods for TCO SnO₂ thin film characterization and discuss their advantages and shortcomings based both on the theory and on our own experience of their application.

3.4.1 Carrier Concentration

As shown in Sections 3.2.2 and 5.1.2, the Hall effect measurement is the most direct method for the free carrier determination. At the same time, this method is often destructive (we need to cut from the whole produced plate a small sample of a regular shape and solder to it electrical contacts). It should be also mentioned that accuracy of the parameters determined by these measurements (carrier concentration, resistivity, and mobility) could be influenced significantly by the ignorance of the sample geometry, by non-uniformity of composition or structure, and by the roughness of the sample surface. In the presence of voids, microcracks or scratches, parameters defined by measurements can deviate dramatically from those for the substance of the sample. In the case of polycrystalline materials, grain boundaries regions can manifest high resistance. If so, the mobility determined from Hall effect and sample resistance measurements can be much lower than the real mobility of intragrain material.

Seebeck effect measurement is an indirect method for the carrier concentration determination. It could be used routinely if comparative measurements of the Hall and Seebeck effects are conducted on the series of high quality samples with different carrier concentrations for calibration. If we have a reliable empirically established correlation between the Seebeck coefficient and the Hall carrier concentration, then we can replace the Hall measurements by the Seebeck measurements.

Some important features and advantages of the Seebeck coefficient measurements should be mentioned and discussed here:

1. The Seebeck coefficient measurements do not demand some special geometry of the sample and can be performed on the samples of an arbitrary shape and size and even on the samples of non-uniform thickness.
2. The measured Seebeck coefficient is not influenced significantly by the voids, microcracks, grain boundaries. For samples containing such kinds of defects, information obtained about the carrier concentration can be more reliable than that obtained from the Hall effect measurements.
3. Only those portions of the sample material, where the temperature gradient exists, contribute to the measured Seebeck voltage (ΔV). For our arrangement where the entire sample is held at room temperature, except the region close to the heated copper block, only the material located in the vicinity of the block contributes to the measured signal. Thus, if the block is sharpened (thermoprobe), we are able to measure the local Seebeck coefficient. The spatial resolution is on the order of the size of the contact between the block and a sample. It could be easily made less than 1 mm. By relocation of the thermoprobe on the film surface we can map the Seebeck coefficient (and hence the carrier concentration) distribution over the sample area.
4. This method is not destructive: the measurements can be performed on the produced plate; putting of the reference electrodes (copper blocks in our equipment) on the sample surface and relocating them does not damage the film.

5. Each measurement of the local Seebeck coefficient takes a short time if the temperature of measurements is close to room temperature and the tools for measurement are like those described in Sec. 3.2.3.

Carrier concentration can be also determined using the data on plasma frequency, ω_p . This method is indirect, contrary to the Hall measurements and similarly to the Seebeck measurements. The equation, which relates plasma frequency to the carrier concentration, is simpler than that for the Seebeck coefficient. The only parameter we need to know to calculate the concentration from the ω_p data is the effective mass. If this parameter is not well defined, an empirical approach can be used as in the case of the Seebeck effect. Comparative measurements of plasma frequency and the Hall concentration should be conducted on a series of high quality samples with varying carrier concentration to obtain empirical $n(\omega_p)$ dependence.

Plasma frequency can be determined from a sharp increase in the reflectance spectrum. Our studies demonstrated that the reflectance increase for heavily doped SnO_2 samples is quite sharp, increasing the accuracy of ω_p determination. More accurate data can be obtained when modeling the reflectance and transmittance spectra based on the Drude model. Including the Lorentz oscillators into the model should in principle improve the theory and experiment fitting, but in our studies no considerable manifestations of the Lorentz oscillators were observed.

To determine ω_p we used not only a spectrophotometer but also multi-angle spectral ellipsometry. Ellipsometry is a very sensitive surface and thin film measurement technique

that uses polarized light. It derives its sensitivity, which is greater than a simple reflection measurement, from determination of the relative phase change in a beam of reflected polarized light. Also, ellipsometry is more accurate than intensity reflectance because the absolute intensity of the reflected light does not have to be measured. By using a proper physical model and special software the plasma frequency was derived along with other parameters from the raw ellipsometry data. There was good agreement between parameters obtained with ellipsometry measurements and those obtained from the reflectance spectra. The modeling we used for ellipsometry provided an opportunity also to reveal non-uniformity in ω_p over the film thickness. This was used to screen samples when we selected the uniform samples for the comparative Hall, Seebeck and plasma frequency studies. In general this method can be used if non-uniformity is the issue to be detected and studied.

As compared to the Seebeck effect the optical methods have some shortcomings. While the former can be applied to samples of unlimited sizes, the equipment used for optical characterization puts some limitation on the sample size. Samples with area not higher than 2"×4" could be tested in our spectrophotometer and for the ellipsometry the limitation was 12"×12".

Spatial resolution, for the Seebeck measurements, is determined by the sharpness of the thermoprobe tip. The diameter of the contact spot can be easily made less than 1 mm. As to optical testing the spatial resolution is limited by the light beam cross section. For our spectrophotometer the size of the latter was 1"× 2", for the ellipsometry 1/2"×1/4". The

measurements and the raw data treatment are much easier for the Seebeck measurements. The equipment/tools for these measurements is much simpler, less expensive and more durable. A more fundamental limitation on the optical method application comes from the spectral range of the instruments we use. Our instruments cover visible light range, near UV and near IR ranges, e.g., the spectral range of our spectrophotometer is of 250 to 2500 nm. For the SnO₂ samples with carrier concentration in the range of 1×10^{20} to $6 \times 10^{20} \text{ cm}^{-3}$, the plasma frequency could be measured with an acceptable accuracy. As the concentration decreases, the plasma frequency shifts farther to the IR range ($\omega_p \propto n^{1/2}$) and the accuracy drops. For the concentrations below $1 \times 10^{19} \text{ cm}^{-3}$, measurements of ω_p become unreasonable unless we use a spectrophotometer for the far IR.

3.4.2 Carrier Mobility

Usually mobility, μ , is defined as

$$\mu = (q \cdot n \cdot \rho)^{-1}$$

where n is the carrier concentration, ρ is the measured electrical resistivity, and q is the electron charge magnitude. Concentration can be determined by the Hall, Seebeck and plasma frequency measurements as discussed above. In Sec. 3.2 we described the ρ measurements in the four-point probe and van der Pauw geometry. Other geometries of the sample and probe location can be also used. Usually these measurements are direct current (DC) measurements. Unfortunately, if the sample structure is not perfect, especially if the sample is not a single crystal, imperfections can contribute much the measured ρ value.

The presence of voids, microcracks, non-uniformity of the film thickness or even the surface roughness increase the resistance of the sample and lead to underestimation of the carrier mobility of the substance. In a polycrystalline material, grain boundary regions can be much more resistive than the material inside the grains. Studies of CdTe and CdS thin polycrystalline films conducted in our laboratory have shown that the mobility determined through DC measurements of resistivity can be by orders of magnitude lower than the real mobility of the carriers inside the grains. This difference is due to the presence of a potential barrier (depleted region) at the grain boundary. The electrical equivalent circuit for the grain boundary region contains a resistor and capacitor connected in parallel. Based on this model the AC measurements were used in our laboratory to separate the individual contributions to the measured resistivity of the grain boundaries and of the intragrain material. Indeed the grain boundary resistance at high frequencies is shunted by the grain boundary capacitance and becomes much lower than the intragrain resistance. Unfortunately this method could not be applied to the TCOs where the resistance of the grain boundaries turned out to be very small (see Chapter 5) and the shunting by capacitance is not effective.

Another approach for the real intragrain material mobility measurement was used in this research which was based on optical characterization of the material. Carrier mobility can be calculated if the effective mass value and collision time (momentum relaxation time) are known;

$$\mu = q \tau / m^*$$

We have determined in our studies the electron effective mass of SnO₂ (see Chapter 5) which is in a good agreement with the literature data. Collision time was determined by the spectroscopic ellipsometry measurements as a reciprocal of the collision frequency: $\tau = \omega_c^{-1}$. To distinguish the mobility value obtained in this way we designate it as μ_{opt} contrary to the Hall mobility, μ_H .

Collision frequency is defined by all the collision (scattering) processes which lead to the dissipation of the electron momentum, hence μ_{opt} is a real mobility inside the grain material. Grain boundaries do not influence this parameter if the grain size is much greater than the mean free path length. Hall mobility is determined by measurement of the concentration Hall coefficient as described above and also the DC resistivity of the sample. The latter includes the contribution of grain boundaries and other macroscopic defects, hence μ_H can be much lower than μ_{op} . To make the difference clearer let us consider measurements on the powder of some highly conducting material. It is clear that measured resistance of a powder sample is much higher than that of the bulk single crystal of the same shape and volume. As to the collision frequency determined by optical measurements, it will be the same as a crystal if the grain size in the powder is much greater than the electron mean free path.

Which of the two methods for the mobility determination should be used, depends of the objectives of the material characterization. The optical mobility and optical resistivity, $\rho_{opt} = (q \cdot n \cdot \mu_{opt})^{-1}$, are the real mobility and resistivity of the intragrain material. The DC

resistivity is a characteristic of the film itself with all the structural defects like grain boundaries, voids, etc. and defines the TCO quality with respect to technical applications.

3.4.3 Structural Properties (Film Thickness and Surface Roughness)

The preferential crystallographic orientation of the SnO₂ films was characterized by means of XRD. Our studies of optical and electrical properties of the films did not reveal any remarkable influence of the orientation on these properties. Hence we do not see so far any reason for this kind of characterization.

Granular structure was characterized by means of SEM and AFM imaging of the top film surface and by means of XRD (broadening of the characteristic lines). AFM has much better spatial resolution than SEM and therefore reveals tiny details of the granular structure. When comparing the SEM and AFM images one can see some features in the latter that could be interpreted as manifestations of grains of a very small size (an order of magnitude lower than for those seen in both kinds of images). But it is unclear whether these tiny features are not the images of the grains located deeper in the film and partially shadowed by the grains located higher. It seems that SEM images themselves can detect the differences in the grain size which correlate with the differences in electrical properties. Indeed the increase in the resistivity and reflectivity haze observed in thin films as compared to thick ones correlates with a decrease in the grain size demonstrated by the SEM images. Broadening of the XRD lines is defined not only by the grain size but also by the non-uniform strains common for the polycrystalline films. Then, even if this

method provides an opportunity to estimate an average grain size the latter is the size in the direction normal to the film plane. It could be greater or smaller than that in the plane, while only the latter can influence electrical properties (sheet resistance) of the film. It seems that with respect to structural characterization of the SnO₂ films, SEM imaging is the most affordable and useful among the methods discussed above.

As was mentioned in Sec. 3.1. film thickness and roughness were measured by means of the Surface Profiler and also by using the ellipsometry measurements. The results obtained by these methods are in a satisfactory agreement with each other for the films with a thickness in a range which is typical for the technical applications, that is above 350 nm. For films with thickness of around 100 nm, agreement was much worse. It is difficult right now to conclude which method is more accurate, but reproducibility was better for the ellipsometry measurements. Another preference of the ellipsometry is that this is a non-destructive method while measurements with the profiler demanded removal of some portion of the film to provide a step whose height was measured by the profiler.

3.5 Summary

The variety of methods and techniques we used for the SnO₂ thin film characterization provided a vast information on structural, optical and electronic properties of the material.

The information provided by different methods is supplementary and overlapping in many respects. This allows checking the accuracy of the data obtained and validity of conclusions.

The same parameters of the films, like resistivity, optical transmission, carrier concentration, film thickness, etc., can be derived using different methods and techniques. All of them have their own advantages and shortcomings. Which method should be used for determination of this or that parameter depends on the objectives of testing and studies.

Among all the techniques used for characterization, the multi-angle spectroscopic ellipsometry seems to be the most informative and promising. It provides an opportunity to determine simultaneously a great number of parameters of the film: thickness, surface roughness, spectra of optical transmission, reflectance and absorbance, mobility and carrier concentration. The options provided by this technique should be studied more thoroughly in future, in particular to clarify the possibility to monitor processing in situ.

CHAPTER 4

EXPERIMENTAL: SnO₂:F THIN FILM GROWTH AND PROPERTIES

4.1 Films Growth Using APCVD

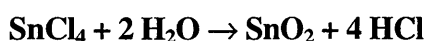
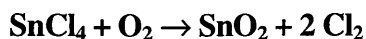
4.1.1 CVD Method Basics: Chemistry of Deposition Process

CVD is a processing technique which introduces different chemical constituents into intimate contact in order to induce a thermally activated reaction to facilitate deposition of a compound on a substrate. There are two kinds of reaction products: one is deposited on the substrate while the other volatile compounds must be drawn away. In APCVD, which is the atmospheric pressure version of CVD, the reactants are brought in a physical vapor form into a heated substrate via an injector mechanism.

The main components of the system are a furnace, source and effluent gas handling systems, and gas injectors. APCVD can produce thin films of materials which function as insulators, or conductors, optical enhancement coatings, and mechanical and/or chemical barriers. It is possible to achieve high material deposition rates with equipment costs that are competitive with other methods of deposition in which processing occurs in high vacuum such as sputtering.

In addition to tin tetrachloride (SnCl₄), tin oxide films have been produced by CVD using tetramethyltin (Sn(CH₃)₄) [44-46], dimethyltin dichloride ((CH₃)₂ SnCl₂) [47], and

dibutyltin diacetate ((C₄H₉)₂Sn(OOCCH₃)₂) [48 and 49]. H₂O and O₂ are the main oxidizing agents used. The most common reactions used to obtain SnO₂ thin films are:



In these reactions the source materials are in liquid form. Vapor is extracted from the liquid via bubbling an inert gas, usually nitrogen, through the heated liquids contained in a vessel bubbler.

There are many requirements for the deposition of high quality materials with APCVD. First, the reactants should be available and appropriate to produce the desired compound material at practical temperatures. Second, the uniformity of material deposition can be controlled by through growth temperature and reaction flow. The control of thermal conditions, which is impacted by furnace design, substrate, and its transport considerations, is necessary for uniform activation of reaction, while reaction flow, which is usually designed to be laminar in planar geometry, is necessary for uniform development of reaction and is impacted by injector, exhaust, and transport designs. Finally, several other general considerations are important including strict control of reactants and reaction, interaction between substrate and process, and effluence handling to remove the waste or the gaseous products which can be poisonous, corrosive, and/or flammable. The substrate temperature should be above the vaporization temperature of the reactants and below the temperature at which damage of the film occurs [4].

To produce FTO, HF or Freon is introduced to the previous reactions:



where CH_3OH is introduced to moderate the reaction by generating oxygen vacancies and n_1 to n_6 are numerical coefficients.

4.1.2 APCVD System Used for Deposition

We have grown films in a Watkins-Johnson system model 4CVD-75 for atmospheric pressure chemical vapor deposition (APCVD). It has the following features: 4 inch-wide furnace, single injector with 5 centimeter long dispenser, four bubblers, muffle type furnace and above 700 °C temperature capability. It mainly consists of furnace, injector, bubblers, and exhaust system as shown in figure 4.1. The main control parameters are the gas flow rate, the substrate temperature, the geometry of the deposition apparatus, and the gas composition. Our goal is not only to produce high conductivity and high transparency films, but also to improve the uniformity and reproducibility of our samples. For this purpose, many improvements of the conventional apparatus were done which led to improved properties of our samples as will be discussed later. A four-inch wide continuous belt transports the substrate through the furnace. The belt speed is adjusted from 0.5 to 15 inches per minute by means of a motor controller in order to produce different thicknesses at given deposition rate. It is connected to an ultrasonic cleaner and air dryer for continuous belt cleaning.

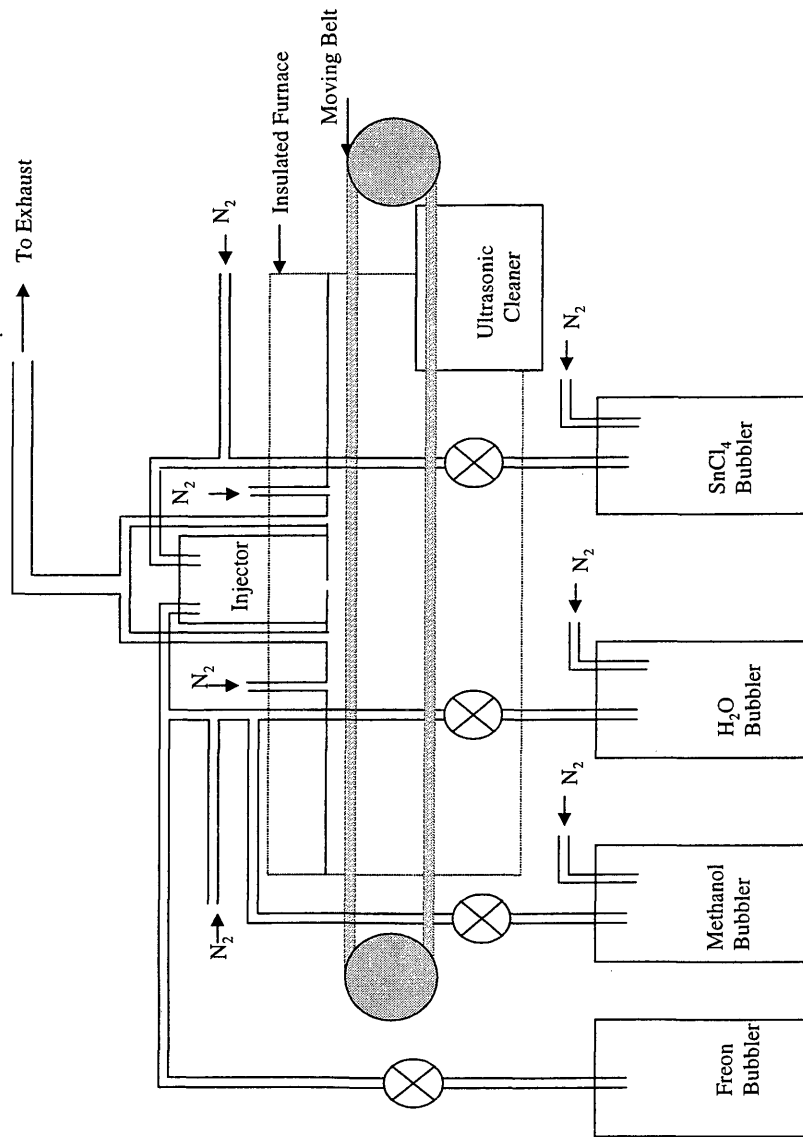


Figure 4.1. The APCVD system we used for production of tin oxide films.

It was found that the lack of uniformity in our deposited films is due to the uneven temperature distribution over a substrate during the deposition because of the non-uniform distribution of temperature across the belt. Aluminum oxide ceramic plates, which have high thermal conductivity, are now used to carry the substrate and provide better temperature uniformity all over the glass substrate. Large area uniform (5%) tin oxide thin films (≈ 500 nm) in a large-scale production with good properties can now be deposited reproducibly.

4.1.3 Effect of the Main Processing Parameters and Improvement of the system Design

4.1.3.1 Temperature

The furnace is used to increase the substrate temperature and consists of four regions (zones) with independent temperature control. Commonly, the first region is for preheating the substrate and the fourth one for cooling the sample gradually, by water recirculation, to prevent cracking or bending the substrate glass. The temperature difference between the second and the third regions is very small and sets the substrate temperature during the deposition. The furnace is completely thermally insulated in all directions and can provide temperature up to 700°C .

The injector which is located inside the furnace is the region where the reactant gases join. The reaction occurs at high temperature, therefore it is important to keep the injector at low temperature (150 to 200°C) by air cooling throughout the injector. Otherwise, the reaction will occur inside the injector instead of the substrate passing

beneath it. In addition, overheating the injector will cause distortion and corrosion problems. The injector temperature should not be too low in order to prevent the gases from condensing inside the injector. Uniform temperature distribution inside the injector plays a major role in film uniformity. For this reason, we also put ceramic plates immediately under the injector in favor of blocking the injector from overheating and non-uniform temperature distribution inside the injector. Gas flow simulation showed that airflow inside the injector was not distributed uniformly. Since the reactant gases have direct contact to the inner surface of the injector, a non-uniform profile of injector temperature will alter the flow pattern and hence offset the improvement of gas flow uniformity. Therefore, a new injector (figure 4.2) was designed and installed to improve the temperature uniformity inside. Table 4-1 lists the optimal temperature settings of SnO₂:F deposition.

Table 4-1. The range of best-applied temperature of SnO₂:F deposition.

Substrate	550 - 600°C
Injector	180 - 240°C
H ₂ O Bubbler	80 - 90°C
CH ₃ OH Bubbler	50 - 60°C
CH ₃ OH/H ₂ O Line	100°C
SnCl ₄ Line	75°C
SnCl ₄ Bubbler	57 - 70°C

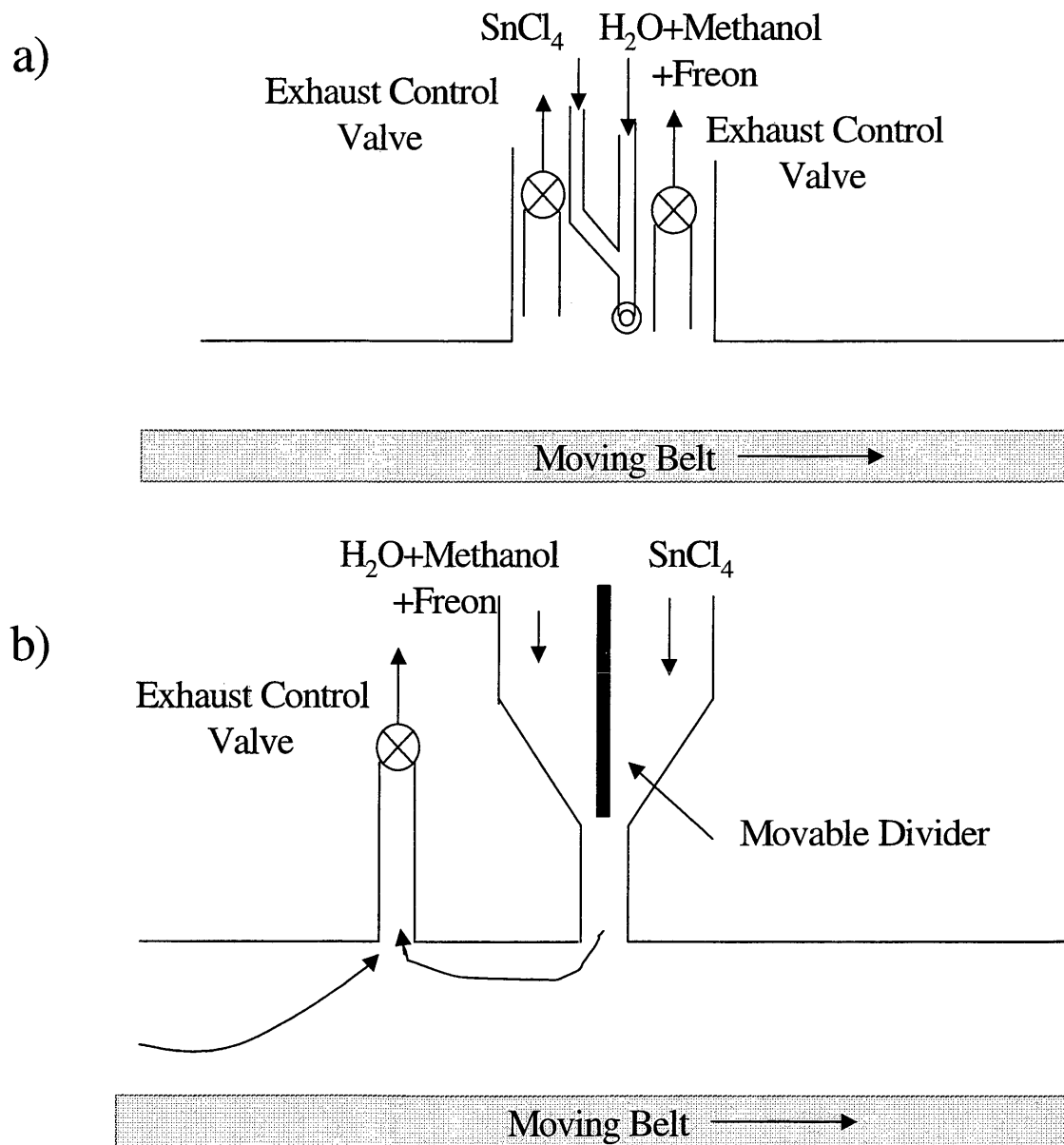


Figure 4.2 Illustration of old (a) and new (b) injector.

4.1.3.2 The Gas Composition and Rate

There are three bubblers connected to the injector through heated pipes for condensation protection. SnCl_4 and H_2O are used as precursors, methanol as catalyst, and Freon (Difluoroethane) as a doping source. These source materials are in the liquid phase in reservoirs. The vapor pressure of the liquid chemical sources was carefully controlled by immersion of the bubbler vessels inside oil filled cans. Heating the liquid leads to evaporation and dry nitrogen is then used as a carrier for the chemical vapors. The reservoir temperature, the nitrogen mass flow sensors, and the pipe temperatures control the amount of reactant chemicals. Additional nitrogen lines are added downstream from the reservoir outlets so that total gas flow into the injector can be varied without affecting the chemical composition or flow. In table 4-2, the N_2 and freon flow rates are shown for producing the best TCO films.

Table 4-2. The gas flow for the best TCO films. The location the gas flows is shown in figure 4.1

N_2 Flow for H_2O Bubbler	300 - 500 SCCM
N_2 Flow for CH_3OH Bubbler	40 - 80 SCCM
N_2 Flow for $\text{H}_2\text{O}/\text{CH}_3\text{OH}$ Line	680 - 900 SCCM
N_2 Flow for SnCl_4 Bubbler	300 - 500 SCCM
N_2 Flow for SnCl_4 Line	200 - 360 SCCM
Freon Line	50 - 75 SCCM

4.1.3.3 Exhaust System

After the reaction, the products of the reaction and any unreacted gases should be removed in order to prevent further uncontrolled reactions on the substrate or on the injector. This requires a negative pressure exhaust system, which is another critical condition. The pressure was monitored by measuring the pressure difference across a 4-mm diameter orifice installed in the system. In order to adjust the pressure, an air intake valve in both sides of the orifice was used. The exhaust system pulls these gases, mainly hydrochloric acid, and transports them into a fume scrubber. The scrubber is a water spray type, which helps to decrease the vapor concentration and produce the venting draft. The scrubber also is provided with a pump for circulation for more safety issues. Exhaust flow should be optimized because an excess exhaust flow will greatly reduce the deposition rate and produce turbulence of gas flow patterns leading to poor reproducibility of the deposited films. Using computational fluid mechanics modeling, Dr. Wolden [50] was able to predict the optimal total exhaust gas (from the nitrogen curtains and injector) flow to be 2 to 3 times the total flow of injected gas and this has been confirmed by the deposition experiments.

From all these parameters, it can be seen how much effort is required in order to optimize the tin oxide properties to be used in photovoltaic solar cells.

4.1.4 Diffusion Barrier

The main reason for using soda lime glass (SLG), rather than other types of substrate, in commercial applications of solar cells is its low-cost and good transparency.

However, SLG contains a large amount of alkali-metal oxides (around 15% [51 and 52] mainly sodium oxide (Na_2O)) which can cause the conductivity of TCO to deteriorate. There have been many reports on the mechanism of this reduction [48 and 52]. The prevailing view is that the sodium atoms in tin oxide act as trapping centers for electrons and that the electrons neutralize the sodium atoms or are bound around sodium atoms [48]. Another view is that the free carriers are scattered by small sodium chloride (NaCl) crystallites [52]. Though the diffusion of sodium can occur at room temperature, it becomes most effective when the glass is exposed to high temperature (more than 475°C) for more than 30 minutes.

To solve this problem, a diffusion barrier is placed between the glass and TCO films. The most critical characteristics of the diffusion barrier are an amorphous and tight structure in order to prevent the migration of sodium ions to the tin oxide. There are many types of materials that can be used, either insulators such as silica (SiO_2), alumina (Al_2O_3), titanium oxide (TiO_2), and silicon nitride (Si_3N_4), or conductors such as titanium nitride (TiN). These diffusion barrier materials help produce good TCOs with much lower resistivity (up to ten times) than without a diffusion barrier. It was found [30] that the resistivity of the film decreases as the barrier thickness increases up to 100 nm, beyond which no change will occur with further increase of the thickness.

In addition, a diffusion barrier can increase the transmission due to matching of the indices of refraction of the multilayer thin films. Glass has an index of refraction of about 1.52 and TCOs have indices of refraction between 1.9 and 2.0 in the visible portion

of the spectra. Any thin film (for example diffusion barrier) insert between glass and TCO with indices of refraction between 1.52 and 1.9 will increase the transmission. This can be calculated by using equation 3.26. The refraction index of aluminum oxide (Al_2O_3) is about 1.7 which, is a good choice to be used as diffusion barrier.

The diffusion barrier of uniform alumina, with thickness of 50-100 nm, was deposited on the substrate by reactive RF magnetron sputtering using a pure aluminum target in oxygen ambient. In order to get good uniformity in the sputtering system; we kept the belt moving go and back. Otherwise, the deposition will be concentrated immediately under the target and thinner on the sides. The films are very transparent to visible light and have small optical losses. Table 4-3 shows the basic deposition condition of Al_2O_3 .

4.1.5 Annealing Conditions

Post-deposition heat treatments of tin oxide films have shown [30] improvement of both the conductivity and transparency. This treatment can be done by annealing the sample at temperatures from 350-550°C for 30 - 120 minutes in argon, nitrogen, or vacuum environment. The mechanism of this improvement is believed to come from increasing the carrier mobility, grain size, and hence this can lead to a decrease of sheet resistance.

Table 4-3. Reactive RF magnetron sputtering conditions for deposition of Al₂O₃.

Base vacuum	8×10^{-6} torr
Target material	Industrial grade, pure aluminum
Target area	4"× 12"
RF power	13.56 MHz, 1500 Watts
Partial pressure of O ₂ /Ar	5 mill torr/ 0.5 mill torr
Total gas flow	20 SCCM
Substrate to target distance	60 mm
Deposition rate	0.5 nm/sec
Substrate moving speed	6"/min

The effects of annealing on tin oxide film properties vary, depending on the quality of the original films. It was found [26] that for a film prepared by APCVD with low optical absorption (4% at 550 nm) and sheet resistance equal to 12 Ω/\square , the resistivity decreased by about 50% when the film was exposed to a hydrogen plasma at 220°C for 10 - 120 seconds but no change in the optical absorption was observed. For a film with low sheet resistance (5 Ω/\square) and high optical absorption (11% at 550 nm), there is no change in resistivity or optical absorption for an exposure time of up to 120 sec. For both films after exposure for 120 sec., a sharp increase of both resistivity and optical absorption was observed. Mansfier et al. [27] found that for highly doped SnO₂:F films,

there is no change in the resistivity after heat treatment in air or argon because the carrier concentration is dominated by fluorine doping. H_2 annealing of SnO_2 at a higher temperature (500°C for 10 min.) decreases the total absorption by 20%-50% in the visible region but results in the formation of elemental tin [53].

Annealing the $SnO_2:F$ sample in an oxidizing ambient medium, air for example, leads to increased resistivity since it leads to reduce density of oxygen vacancies in the film [27]. It is very important to investigate the temperature range versus exposure time in order to achieve the optimized values for the resistivity and optical absorption. The ambient plasma plays a major factor and needs a comprehensive study to understand how it can effect the $SnO_2:F$ films properties. In addition, the heating and cooling rate can effect the quality of the sample where too fast heating or cooling can damage the film.

Annealing temperature, baking time, and the ambient gases are the three main factors that affect the sample during the annealing. In our studies, these three parameters were varied in order to get best TCO results. We studied samples with annealing temperature ranges from 375-450°C at a time range of 1.5 to 2 hours in N_2 or He_2 gas as in table 4-4. For these samples the properties will be discussed later.

4.2 Films Properties Dependent on the Processing Procedures

Three kinds of 4×4 substrate glasses are used for the coating: 2mm thick soda lime glass (SLG), 1.1-mm thick soda lime glass, and 1.1 mm thick Corning glass 1737F. SLG is preferred in manufacturing solar cells because of its low cost while Corning glasses are

used for comparison purpose (the Corning glass is about ten times more expensive than SLG). All these kinds of substrate provide good electro-optical properties. In the following sections we will compare results on the three substrates: # 2mmSLG, # 1mmSLG, and # 1.1mmCG. Tin oxide thickness of these samples is 700, 343, and 770 nm respectively.

Table 4-4. Annealing conditions for the substrate.

condition #	temperature (°C)	time (hr.)	inert gas
1	450	2	N ₂
2	385	1.5	N ₂
3	400	1.5	He ₂
4	375	1.5	He ₂

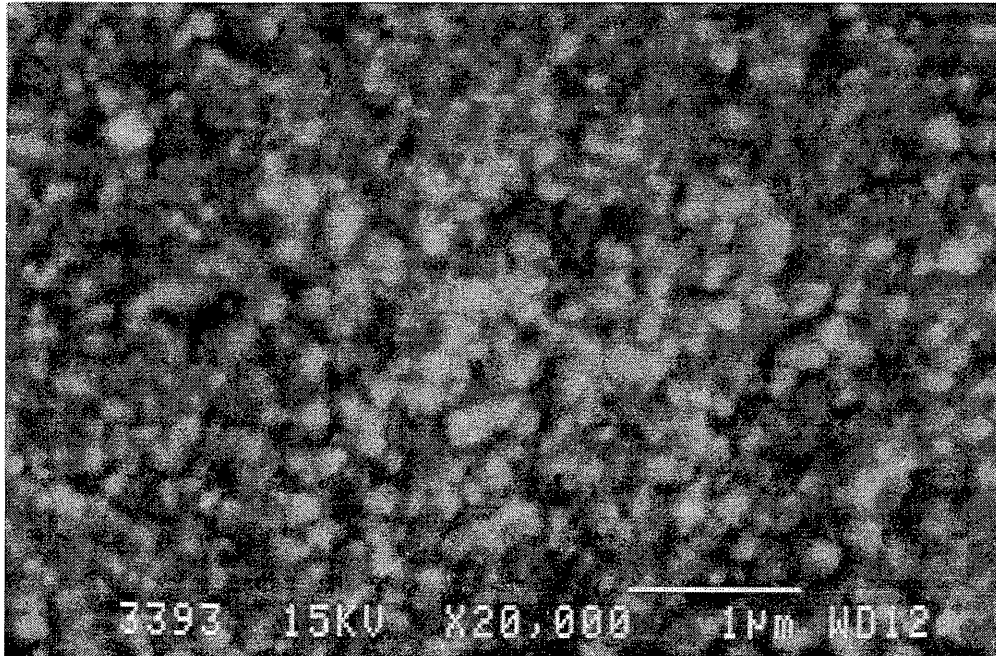
4.2 1 Structural Properties

Scanning electron microscopy (SEM) was used to show a grain shape and size for SnO₂:F. We observed two kinds of grains appearances for different substrates, circular and planar grains. For soda lime glass the circular grain size is about 150 - 200 nm while for Corning glass around 130 nm. For soda lime glass, planar grains are of the size of 140 nm × 300 nm and for Corning 140 nm × 330 nm. The smaller grains are preferred in our application because the porosity becomes lower. Although decreasing the grain size

usually leads to an increase in the grain boundary contribution to the sample resistivity, in our TCOs materials we have found that in heavily doped and sufficiently thick SnO_2 films the role of grain boundaries is not considerable. SEM images of all the samples studied demonstrated some dark spots that may be interpreted as pinholes. But, if so, these pinholes do not penetrate through the entire sample because their sizes are much lower than the thickness of the film (greater than two times). We did not notice any relation between the thickness and the grain size or the grain type for thickness between 350 to 850 nm. Figure 4.3 presents the images of sample 1mmSLG and 1.1mmCG. In sample 1mmSLG, the grains are circular with sizes of about 150 nm. For samples 1.1mmCG, the grains are planar with sizes of 300×150 nm.

X-ray diffraction (XRD) was used to examine the grains and the preference plane in tin oxide films. Planes (211), (101), (200), and (110) with d space of 1.7735 ± 0.0022 , 2.6612 ± 0.0027 , 2.376 ± 0.0036 , and 3.3723 ± 0.0027 Å respectively were the four most preferred planes in our samples. This is in a good agreement with tin oxide powder, which has preferred planes of (110), (101), (200), and (211) with d space of 3.351, 2.644, 2.369, and 1.765 Å respectively [13]. Most of our samples show a preferred grain orientation with (211) planes parallel to the substrates. A very small peak associated with SnO was detected for most of our samples. A typical result is shown in figure 4.4. For sample # 1mmSLG with B_m was determined by fitting a Person function to the experimental data, the grain size calculated by using equation 3.1 is equal to 27-34 nm.

a)



b)

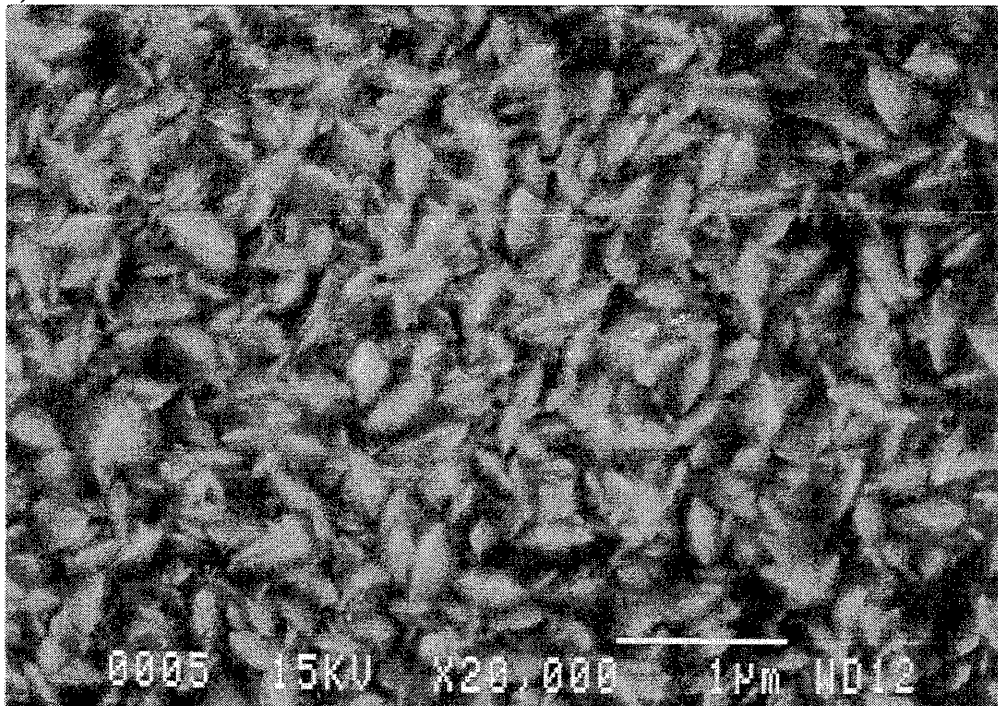


Figure 4.3 SEM images of sample 1mmSLG (a) and sample 1.1mmCG (b).

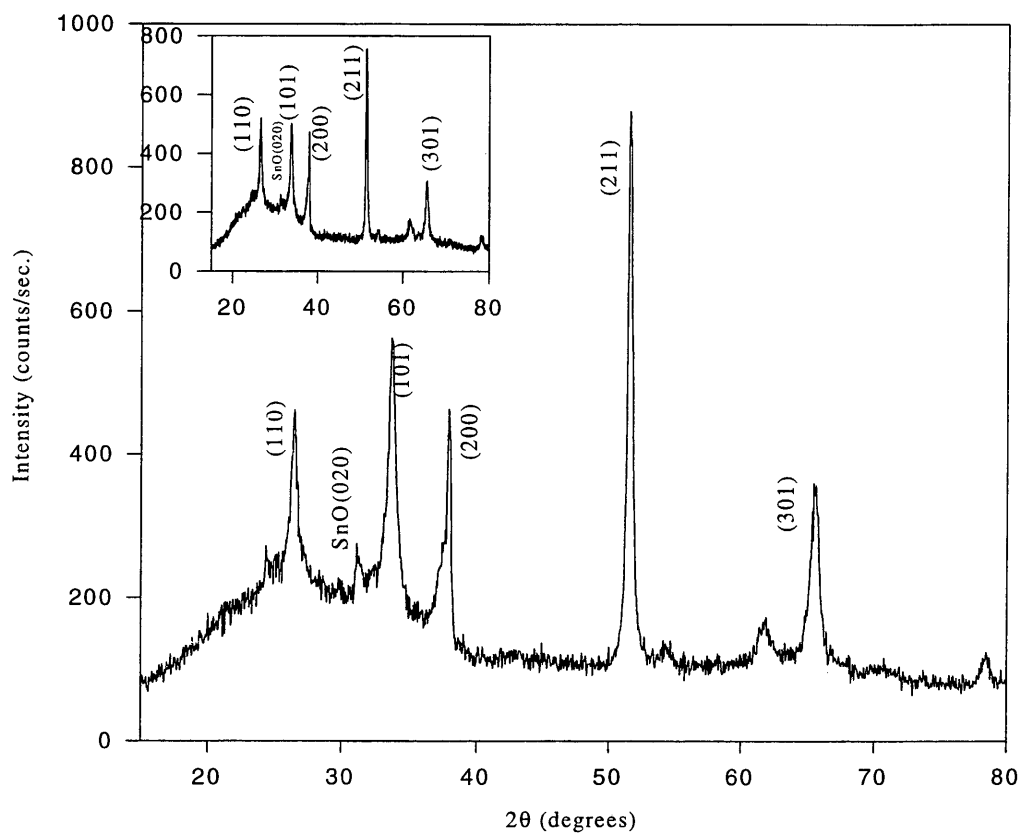


Figure 4.4 XRD of sample 2mmSLG before (large box) and after annealing (small box).

AFM provided a grain size of around 150 nm for sample 1mmSLG as in figure 4.5. In addition, the roughness of the same sample is about 16.5 nm, which is in a good agreement with ellipsometry measurement in which roughness was found of about 25 nm.

Thus from these measurements, XRD measurements show the grains height to be about 30 nm while SEM and AFM measurements give good agreement. The length and width of the grains is about 150 nm. Non-uniform stress can cause XRD line broadening that leads to an under estimation of the grain size.

SEM was also used to study grain sizes of SnO₂:F on both bare and alumina-coated glass substrates. The grains for both types of films have dimensions of about 150 nm to 200 nm as in figure 4.3a and 4-6. Films are compact and uniform and exhibit a textured morphology. There is no significant difference between the preferred orientation of films on substrates with diffusion barriers and that without diffusion barriers.

The surface morphology of the films was not affected by post-deposition annealing. In addition, a small change in the orientation was noticed when the samples were treated for post-deposition annealing. This can be seen also from figure 4.4, which presents a XRD graph of sample 2-2mmSLG before and after annealing.

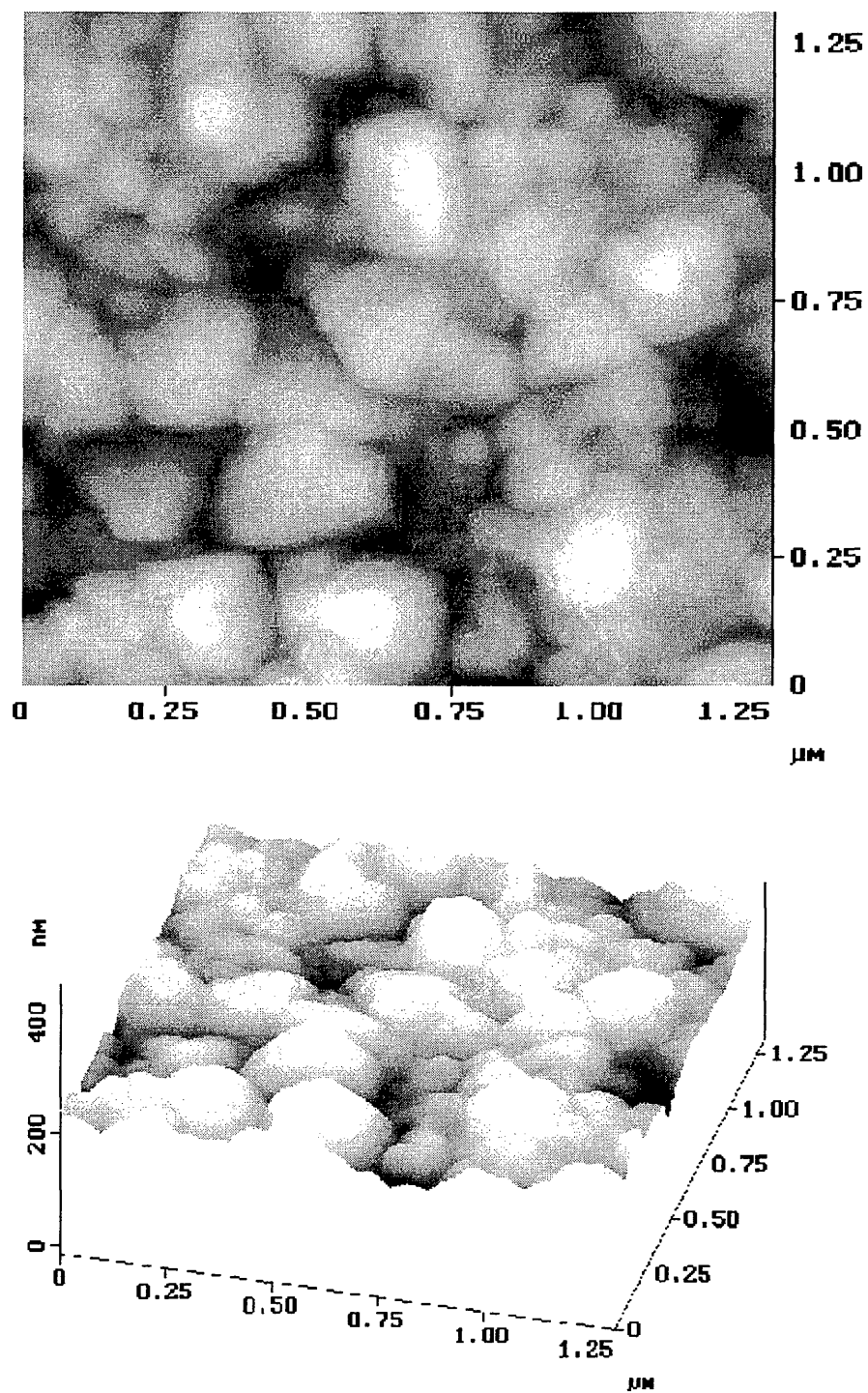


Figure 4.5 AFM image of sample # 1mmSLG.

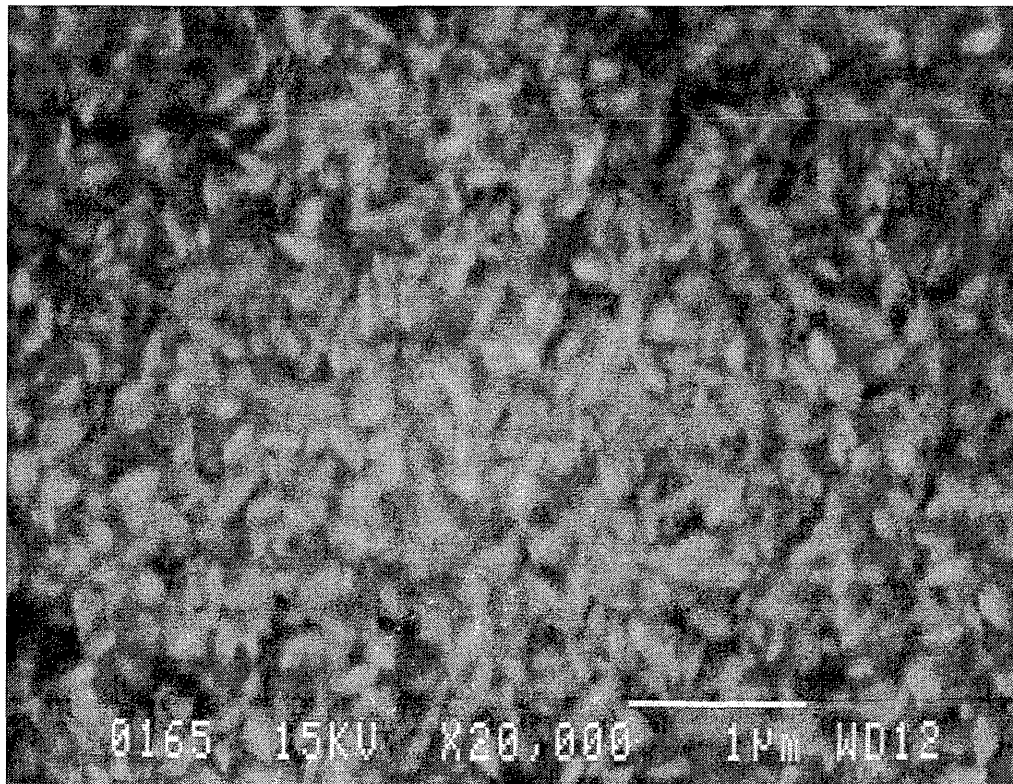


Figure 4.6 SEM image of sample 2mmSLG.

4.2.2 Optical Properties

Spectrophotometer measurements showed that the optical transmission of our samples in the spectral range of 400-1000 nm is about 80% with average reflectance of ~10% as in figure 4.7. Considering these values for soda-lime glass substrates, we may conclude that the optical absorption of tin oxide films is very low. It should be noticed that the reflectance plasma edge shifts to shorter wavelength as carrier concentration increases in agreement with Drude model.

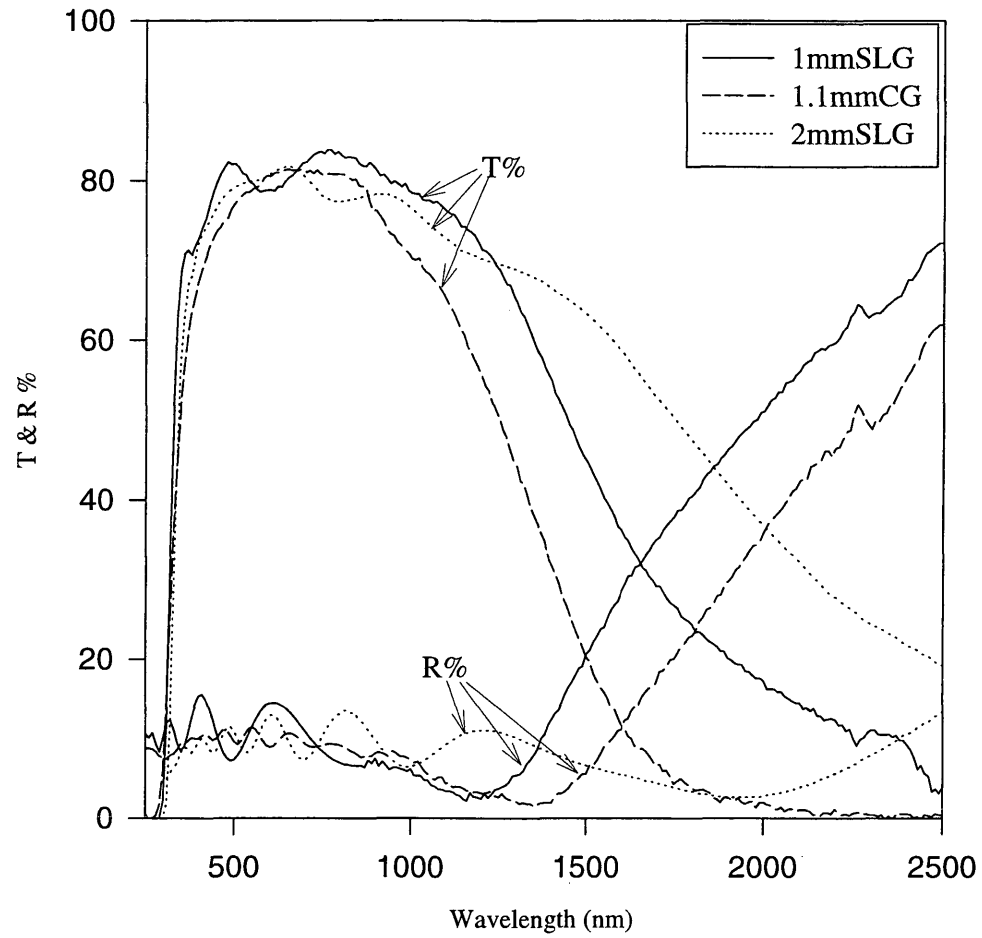


Figure 4.7 Transmission and reflection of some typical samples.

In order to take care of the effect of absorption of the glass, tin oxide absorption was calculated by using the relation:

$$A_T = 1 - T - R - A_G \quad (4.1)$$

where T and R are the total transmission and reflection of tin oxide plus the substrate and A_G is the absorption of the bare glass as in figure (4.8) and equal to:

$$A_G = 1 - T_G - R_G \quad (4.2)$$

where T_G and R_G is the total transmission and reflection of bare glass. As expected, the Corning glass transmission is higher than SLG and the thick SLG transmission is lower than the thin one. Figure 4.9 shows the tin oxide absorption of the three samples calculated from equation 4.1. It can be noticed from this figure that in the spectral region between 400-1000 nm, the absorption of tin oxide on Corning glass is higher than on the soda lime glass (both 1mm and 2mm thickness).

We can use the relation (3.16) to calculate the absorption coefficient:

$$\alpha = -\frac{1}{t} \left[\ln \left(\sqrt{A^2 + B} - A \right) \right] \quad (4.3)$$

where $A = \frac{(1+T-R)^2}{2 \times T \times R^2}$ (4.3a)

and $B = \frac{(1+T)^2}{R^2}$ (4.3b)

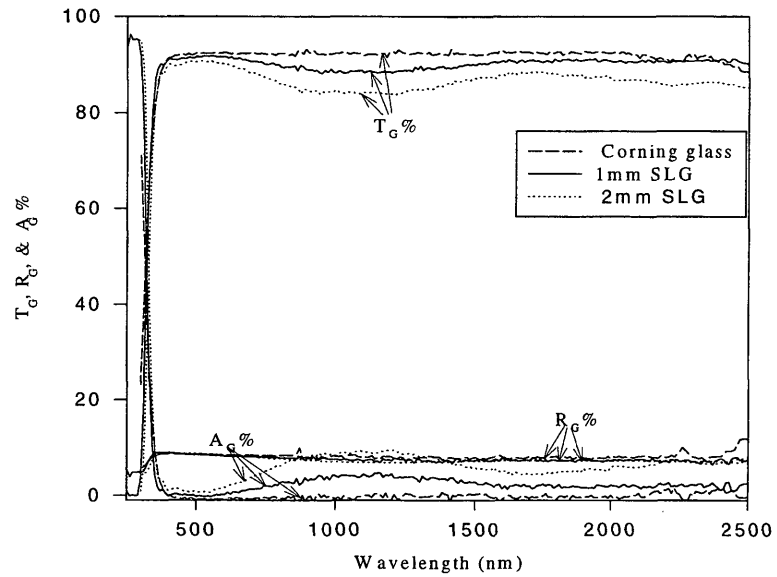


Figure 4.8 Transmission, reflection, and absorption of some substrates.

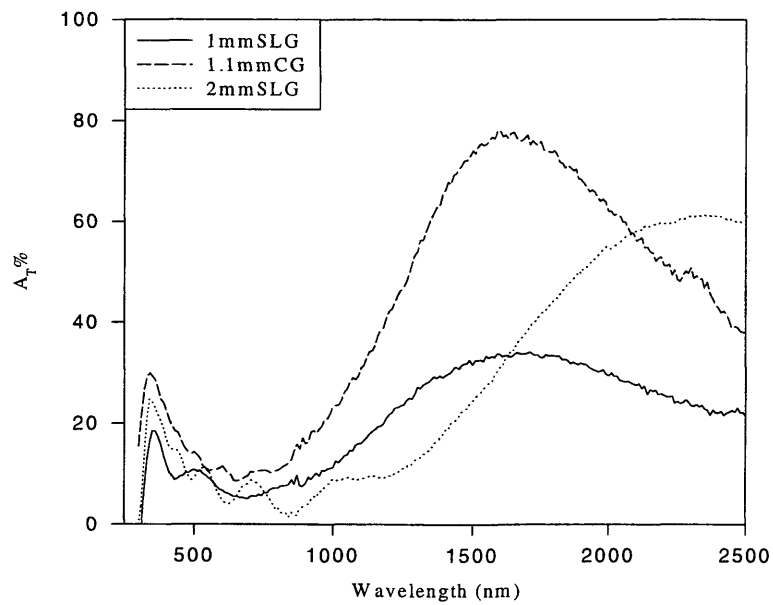


Figure 4.9 Absorption of tin oxide for some typical samples.

As in figure 4.10, the absorption coefficient is high for high photon energy. We will find the energy gap of SnO₂:F, using the relation:

$$\hbar\omega\alpha \propto (\hbar\omega - E_g)^{1/2} \quad (4.4)$$

and by drawing a graph of E versus $(\alpha E)^2$ (figure 4.11). By calculating the intersection of the graphs, we found the energy gap values to be equal to 3.97 eV for sample #2mmSLG, 3.98 eV for sample #1mmSLG, and 4.25 eV for sample #1.1mmCG.

Ellipsometry was used successfully to find index of refraction (n) and extinction coefficient (k) for samples 1mmSLG and 1.1mmCG. From k measurements, absorption coefficient can be calculated by using the relation:

$$\alpha = 4\pi k / \lambda \quad (4.5)$$

Figures (4.12) and (4.13) show a comparison between α using equation 4.3 and 4.5. From these graphs, one can see a good agreement between the data except for high energy where α derived from equation 4.5 goes to zero. This raises a doubt in k values that derived from ellipsometry at high energy (> 3 eV). In addition, it is possible to determine α from the transmission measurements only. By using two identical samples with different thickness d_1 and d_2 , we can use equation 3.17 to get the relation:

$$\alpha = \frac{1}{d_2 - d_1} \text{Ln} \left[\frac{T_1}{T_2} \right] \quad (4.6)$$

Figure (4.12) shows also α obtained by using the previous relation for sample 3392 with thickness equal to 370 nm, which was identical (same deposition

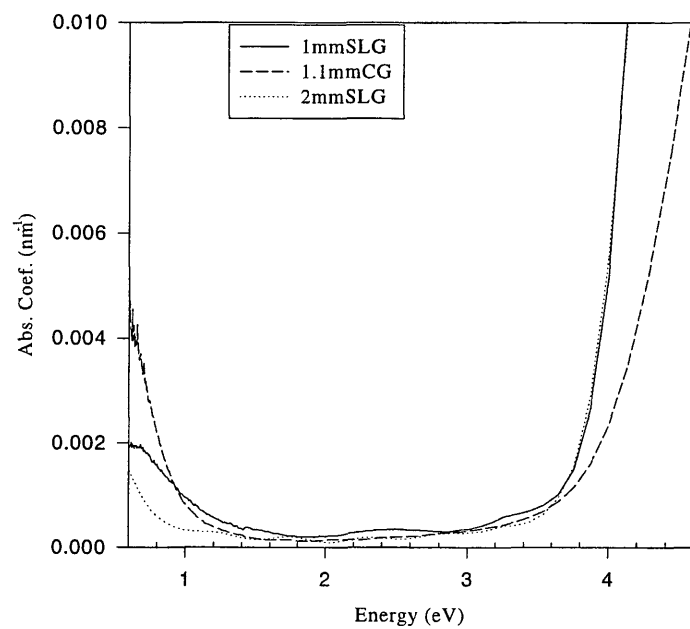


Figure 4.10. Absorption coefficient of the typical samples

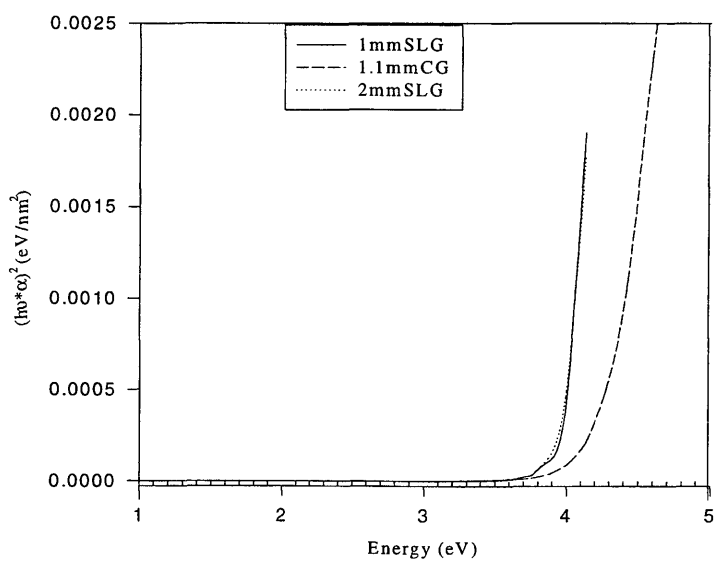


Figure 4.11. Square of absorption coefficient * Energy of the typical samples.

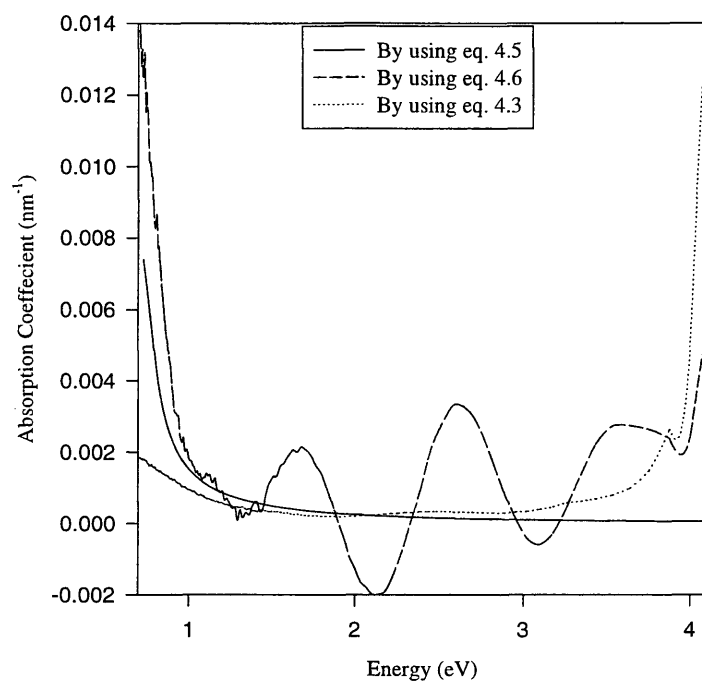


Figure 4.12 Absorption coefficient of sample 1mmSLG using different equations.

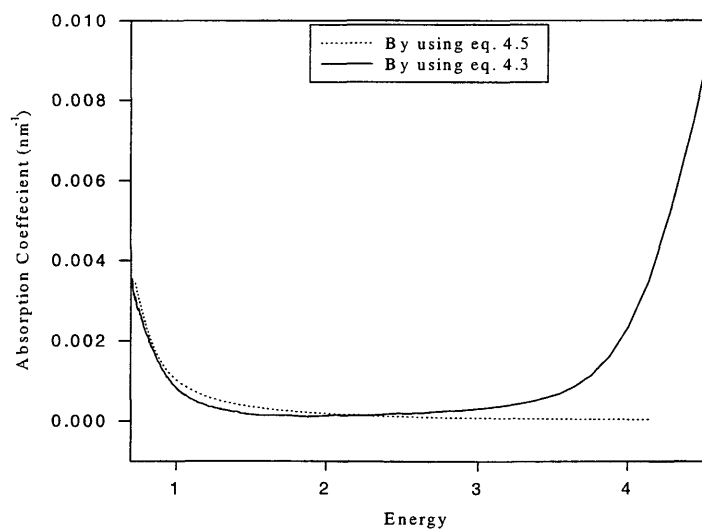


Figure 4.13. Absorption coefficient of sample 1.1mmCG using different equations.

parameters and conductivity) to sample 1mmSLG. The approximation of equation 3.17 and the uncertainty of determining the thickness for both samples can explain the negative values. This may be due to non-uniformity, roughness, or defects inside the film.

Being affected by annealing, optical properties of the samples depend on the existence of the diffusion barrier. Annealing films without alumina does not effect transmittance or reflectance. For films with alumina, there is an increase in transmission by about 2% but there is not a noticeable difference of reflectance.

4.2.3 Electrical Properties

By using a Bio-Rad Hall effect system and 4-point probe, we are able to measure the resistivity, sheet resistance, carrier concentration, and mobility. The film thickness was measured by surface profilometry. We were able to produce samples with sheet resistance of $7 \Omega/\square$ and resistivity of $5 \times 10^{-4} \Omega \cdot \text{cm}$ for film thickness of around 350 nm and transmission over 80% for wavelength between 500 – 900 nm. In general, our samples have carrier concentration of $1 \times 10^{20} - 6 \times 10^{20} /\text{cm}^3$, and mobility from 14 to 30 $\text{cm}^2/\text{V}\cdot\text{s}$. Table 4-5 displays the electrical properties of the three typical samples.

Measuring the free carrier concentration and mobility using Hall effect requires implies a very accurate calculation of the thickness including the roughness. Non-uniform films or films with high roughness will produce a misleading estimation of n and μ . In addition, the presence of cracks or voids will lead to less accurate results as

discussed earlier. For these reasons, other methods, independent of the thickness, of calculating free carrier and mobility were applied. Thermoelectric power (Seebeck coefficient) can provide us with a good estimation of n . These measurements were performed with a simple home-made apparatus and did not require cutting small samples from the whole deposited films, thus being non-destructive. In addition, ellipsometry and spectrophotometer provide data to be compared with the previous methods. All these methods provided us with very accurate data on free carrier concentration and mobility in addition to other important parameters, such as the plasma frequency and dielectric constant as we will discuss later.

Table 4-5 Electrical properties of three typical samples.

sample #	Sheet Resistance Ω/\square	Resistivity $\times 10^{-4} \Omega.cm$	Carrier Concentration $\times 10^{20} cm^{-3}$	Mobility cm^2/Vs
2mmSLG	38.4	26.9	1.48	15.7
1mmSLG	14.2	4.89	5.0	25.7
1.1mmCG	10.1	7.78	4.43	18.1

Samples with diffusion barriers were always found to be better in conductivity than those without diffusion barriers for the same deposition condition. The ratio reaches up to 10 times for high sheet resistance and it starts to decrease as the sheet resistance decreases.

It was found that annealing the sample at 375°C for 1.5 hours in He₂ gives the best improvement compared to the other annealing condition that we tried as is seen from table 4-6.

Table 4-6 Electrical property for two samples before and after annealing.

Sample #	ann. con.	diff. barr.	Thickness nm	Sheet. Res. Ω/\square	Resis. $\cdot 10^{-3}$ $\Omega.cm$	$N \cdot 10^{20}$ /cm ³	Mobility cm ² /V.s
2-81	none	yes	816.6	22.4	1.83	1.89	17.9
2-81	1.5hr 375°C	yes	816.6	20.4	1.67	1.85	20.13
2-165	none	no	598.4	38.4	2.3	1.73	15.65
2-165	1.5hr 375°C	no	598.4	32	1.92	1.84	17.7

4.3 Summary

In this chapter, we introduced basic information about the APCVD system which we used for depositing fluorine doped tin oxide thin films. Many discussions about the best deposition parameters (temperature, gas composition, and exhaust system) were presented including improving the conventional apparatus that were aimed of improving the film quality, uniformity, and reproducibility. Conductivity and maybe the transmittance can be improved by (1) inserting a diffusion barrier (aluminum oxide) between the substrate and the film and (2) annealing the sample at high temperature with

different time duration in different ambient gases. Interesting and important results were found in this subject and more work should be done in this topic, especially reproducibility.

In the second part of the chapter, we provided a comprehensive study of the TCOs electrical and optical properties. The properties of the fabricated films are presented and discussed. We studied the structure of the sample through SEM, AFM, and XRD. Electrical properties (mainly carrier concentration and mobility) are obtained by Hall measurements and optical properties (transmittance, reflectance, and absorption) are measured with spectrophotometer and ellipsometry.

CHAPTER 5

STUDIES OF BASIC ELECTRONIC PROPERTIES OF SnO₂ THIN FILMS

This chapter presents studies of SnO₂ thin films aimed at determination and discussion of the fundamental parameters of the electron system in this material which are relevant to one of the most important characteristics of TCOs, i.e., carrier mobility. Our approach is based on experimental studies and combined analysis of a variety of transport phenomena including AC conductivity in a high frequency (optical) range.

5.1 Theory of Electron Transport in Solids

In this section we will present the equations that relate the measured characteristics of a material to the fundamental parameters, such as carrier concentration, mobility, effective mass, collision time, mean free path length, and dominating scattering mechanism. These equations will have a rather simple form, which makes them easy to analyze and use in the following sections for the data interpretation, for numerical estimations and theoretical modeling. These equations are presented in many publications and textbooks, [e.g., in 39 and 54], and were derived based on some simplifications and approximations of the general theory. Before presenting and discussing these equations we must discuss validity of these

assumptions and approximations with respect to the specific properties of material we studied, that is thin films of the heavily doped SnO₂.

5.1.1 Approximations of the Theory and Verification of their Validity

5.1.1.1 Quasi-Continuous Electron Spectrum

When the film thickness is very small, one has to discuss a possible influence of the quantum-size effect. The electron spectrum will be quantized if the de Broglie wavelengths, λ , is comparable to the film thickness. The materials we studied were heavily doped (carrier concentration ranged from 1×10^{20} to $5 \times 10^{20} \text{ cm}^{-3}$). The electron gas is strongly degenerate at room temperature, which means that the Fermi level distance from the band edge, η , is much higher than $k_B T$ (k_B is the Boltzmann constant). In this case only those electronic states contribute to the transport phenomena whose energy is close to the Fermi level, or in the other words, whose wave vector \mathbf{K} is close to the Fermi surface in the \mathbf{K} -space. K_F values and corresponding de Broglie wavelengths, λ_F , can be estimated using the formulas:

$$K_F = (3\pi^2 n)^{1/3} \quad (5.1);$$

$$\lambda_F = 2\pi / K_F \quad (5.2)$$

For the concentrations mentioned above, that gives values of λ_F in the range of 25 to 43 Å. The typical thickness of the films studied were in the range of thousands of

angstroms. Thus quantum-size effect can be neglected and the spectrum can be considered as a continuous one.

5.1.1.2 Quasi-Classical Approximation

In this approximation the electrons are treated as particles with simultaneously well-defined space coordinates and momentum/velocity values. In this case we can use the Boltzmann equation formalism. We can then refer to the extensive literature on treatment of transport phenomena based of this approximation in other heavily doped semiconductors. Good agreement of theory to the vast experimental results has been reported for many semiconductor materials with fundamental characteristics similar to those of SnO₂, such as carrier concentration and mobility, effective mass, etc. In particular, Si, some III-V semiconductors, PbTe, and PbSe, can be mentioned.

5.1.1.3 Relaxation Time Approximation

Electric and heat currents are zero in the equilibrium state when the distribution of electrons over the band states is described by the Fermi-Dirac function:

$$f_o(E) = \frac{1}{\exp[(E - \eta)/k_B T] + 1} \quad (5.3)$$

External fields disturb the distribution from equilibrium and the scattering processes drives the distribution to equilibrium. The stationary non-equilibrium distribution $f(\mathbf{K})$ is formed under the action of these two factors. To define the non-equilibrium $f(\mathbf{K})$ the Boltzmann

equation can be used which in principle is an integro-differential one. The mathematical problem is simplified significantly if the so-called collision integral, I_{col} , which represents the scattering processes in the equation, can be reduced to a simple analytical form:

$$I_{\text{col}} \equiv \left[\frac{\partial f(\mathbf{K})}{\partial t} \right]_{\text{col}} = - \frac{[f(\mathbf{K}) - f_0]}{\tau(\mathbf{K})}$$

This means that after the external fields are switched off, the non-equilibrium distribution is relaxing according to the equation: $f(t) - f_0 = [f(0) - f_0] \exp(-t/\tau)$. The parameter τ is called the relaxation time and defines the rate of the equilibrium restoration.

The relaxation-time approximation is especially justified when scattering processes are elastic, that is if the change in the electron energy due to the collision is much smaller than the initial energy. That is the case for scattering by impurities, point defects, dislocations, and grain boundaries. In the case of phonon scattering relaxation-time approximation is always valid if the Fermi energy is much higher than the characteristic phonon energies. That is the case for our materials where Fermi energy ranges from 0.25 to 0.75 eV (see Sec. 5.2.3) and the maximum phonon energies are lower by an order of magnitude.

5.1.1.4 Isotropic Electron Spectrum

Analysis of electron transport is rather complicated if the $E(\mathbf{K})$ dependence is anisotropic, that is if the constant energy surfaces in \mathbf{K} -space are non-spherical. In this case the effective mass must be in general treated as a tensor that varies from one point in the \mathbf{K} -

space to another. As for relaxation time, it also depends on the \mathbf{K} magnitude and direction but can be treated as a tensor only for some special cases. For the isotropic spectrum, both m^* and τ are scalars and their magnitudes can depend only on the energy of the carriers or in other words on the magnitude of the wave vector. According to [55], the constant energy surfaces in SnO_2 are represented by ellipsoids of revolution with slightly different (about 10%) lengths of the ellipsoids axes. This very small difference enables us to use the isotropic approximation for SnO_2 without significant errors in calculated transport coefficients. There are two more reasons to make this assumption: (a) among the transport coefficients we studied only electrical conductivity/mobility is anisotropic, but the estimate of this anisotropy based on [56] does not exceed 20-25 %; the Hall and Seebeck coefficients are isotropic for the ellipsoidal constant energy surfaces; (b) our films do not have some well defined crystallographic orientation, hence even the conductivity should be averaged over the directions of the grain orientation and be macroscopically isotropic. Thus we assume that $E(\mathbf{K})=E(K)$.

5.1.1.5 Parabolic Electron Spectrum

$E(\mathbf{K})$ dependence in general can be considered as a parabola only in the vicinity of the band extremum that is close to the band edge. As K values increase, the E dependence on K becomes slower than K^2 . The higher the energy of carriers, the greater the influence of the non-parabolicity. For many direct-gap and narrow-gap semiconductors such as InSb, GaSb, or PbSe, $\text{Hg}_{1-x}\text{Cd}_x$, $\text{Pb}_{1-x}\text{Sn}_x\text{Te}$, non-parabolicity was studied in detail both

theoretically and experimentally (the latter in heavily doped materials or at elevated temperatures) and found well pronounced and important for transport phenomena (e.g. see [39 and 54]). One of the most prominent manifestations of the non-parabolicity is the growth of effective mass with Fermi level. For SnO_2 there were a few attempts to investigate non-parabolicity, but published data are controversial [31 and 57]. We have studied the effective mass dependence on the Fermi level position in a wide range of the latter (from 0.25 to 0.75 eV) by means of comparison of the measured Hall and Seebeck coefficients and plasma frequency (see chapter 3). We did not find any indication of the growth of effective mass with carrier concentration (Fermi level). Therefore we assume parabolic spectrum for materials we studied.

5.1.1.6 High Degeneracy of the Carrier Gas and Sommerfeld Approximation

With all the approximations discussed above, the theory comes to the following equations for electrical conductivity, the Hall and Seebeck coefficients in the n-type semiconductor:

$$\sigma = \frac{nq^2}{m^*} \langle \tau \rangle \quad (5.4)$$

$$R_H = -\frac{1}{qn} \frac{\langle \tau^2 \rangle}{\langle \tau \rangle^2} \quad (5.5)$$

$$S = -\frac{1}{qT} \frac{\langle (E - \eta)\tau \rangle}{\langle \tau \rangle} \quad (5.6)$$

Here $\langle \dots \rangle$ symbolizes averaging of the function of E over all the energy band states with a weight function $W = (-\partial f_o / \partial E) \cdot D(E) \cdot v(E)^2$, where $D(E) = [4\pi \cdot (2m^*)^{3/2} / h^3] \cdot E^{1/2}$ and $v = (2E/m^*)^{1/2}$ are the density of states function and electron velocity, respectively, and h is the Planck constant.

The distribution function f_o , as well as $(-\partial f_o / \partial E)$, drop to zero exponentially for $(E - \eta) / k_B T > 1$, hence the finite extent of a band is well simulated by the limit $E = \infty$ when integrating over the band spectrum. The lower band edge will be taken as an origin of energy scale ($E_{\min} = 0$). Thus the averaging of some function $\Theta(E)$ is described by the equation:

$$\langle \Theta(E) \rangle = \frac{\int_0^{\infty} \Theta(E) E^{3/2} \left(-\frac{\partial f_o}{\partial E} \right) dE}{\int_0^{\infty} E^{3/2} \left(-\frac{\partial f_o}{\partial E} \right) dE} \quad (5.7)$$

The function $(-\partial f_o / \partial E)$ drops exponentially to zero on both sides of $E = \eta$. Indeed,

$$\left(-\frac{\partial f_o}{\partial E} \right) = \frac{1}{4k_B T \cosh^2 [(E - \eta) / 2k_B T]}$$

Hence, in the case of high degeneracy, $\eta / k_B T \gg 1$, only the states with the energy close to the Fermi level contribute considerably to the integrals above. In addition,

$$\int_{-\infty}^{\infty} \left(-\frac{\partial f_o}{\partial E} \right) dE = f_o(-\infty) - f_o(+\infty) = 1 - 0 = 1$$

Thus the properties of $(-\partial f_o / \partial E)$ function are similar to those of the δ -function if one takes into account that, due to the rapid converging of the integral, replacement of 0 as a

lower limit by $-\infty$ does not change the integral value. The so-called Sommerfeld approximation is commonly used for calculation of the integrals like those in Eq. 5.7, in the case of high degeneracy:

$$\int \Phi(E) \left(-\frac{\partial f_o}{\partial E} \right) dE \approx \Phi|_{E=\eta} + \frac{\pi^2}{6} \frac{\partial^2 \Phi}{\partial E^2} |_{E=\eta} (k_B T)^2 \quad (5.8)$$

This approximation is valid under conditions: (a) $\eta/k_B T \gg 1$ and (b) $[\Phi(E)]^{-1} \partial^2 \Phi / \partial E^2 |_{E=\eta} (k_B T)^2 \ll 1$. The first condition corresponds to high degeneracy and the second one means smoothness of $\Phi(E)$ near the Fermi level. If both conditions are satisfied, we have to the first non-vanishing approximation:

$$\int \Phi(E) \left(-\frac{\partial f_o}{\partial E} \right) dE \approx \Phi|_{E=\eta} \quad (5.9)$$

If $\Phi(E) = (E - \eta) \cdot \Psi(E)$, then the second condition is not satisfied even if $\Psi(E)$ is a smooth function, and we can not neglect the second term in Eq. 5.8. In this case one obtains to the first non-vanishing approximation:

$$\int \Psi(E) \left(-\frac{\partial f_o}{\partial E} \right) (E - \eta) dE = \frac{\pi^2}{3} \frac{\partial \Psi}{\partial E} |_{E=\eta} (k_B T)^2 \quad (5.10)$$

It will be shown in Sec. 5.1.2 that Sommerfeld approximation can be applied with a very small inaccuracy to the analysis of the data for the samples of SnO_2 we studied.

5.1.2 Transport Coefficients for the Stationary External Fields

Equations 5.4, 5.5, and 5.6 were derived under the approximations 1 to 5 discussed above and also under the assumptions that material is spatially uniform and external fields are stationary. To come to the final formulas based on the sixth, Sommerfeld, approximation, we must first estimate an inaccuracy in calculations of σ , R_H , and S for our materials when using this approximation in a form of Eq. 5.9 (for σ and R_H) or Eq. 5.10 (for S).

For Θ being a power function of energy: $\Phi(E)=E^P$, one obtains from Eq. 5.8:

$$\int E^P \left(-\frac{\partial f_o}{\partial E} \right) dE \approx \eta^P \left(1 + \frac{\pi^2}{6} P(P-1)(k_B T / \eta)^2 \right) \quad (5.11)$$

To calculate $\langle \tau \rangle$, $\langle \tau^2 \rangle$ and $\langle (E-\eta)\tau \rangle$ in Equations 5.4, 5.5, and 5.6, using Eq. 5.7, one needs to know the energy dependence of τ . Assuming that $\tau(E)$ is a smooth function in the vicinity of the Fermi level we will approximate it in this region with a power function:

$$\tau(E) = \tau(\eta)(E/\eta)^r; r \equiv d \ln \tau / d \ln E \Big|_{E=\eta} \quad (5.12)$$

Parameter r value depends on the dominating scattering mechanism and usually is called "scattering parameter". Based on equations 5.7, 5.11, and 5.12, we obtain:

$$\langle \tau \rangle = \tau(\eta) \eta^{-r} \frac{\int E^{3/2} E^r \left(-\frac{\partial f_o}{\partial E} \right) dE}{\int E^{3/2} \left(-\frac{\partial f_o}{\partial E} \right) dE} = \frac{\tau(\eta) \eta^{-r} \eta^{r+3/2} \left(1 + (\pi^2/6)(r+3/2)(r+1/2)(k_B T / \eta)^2 \right)}{\eta^{3/2} \left(1 + (\pi^2/6)(3/2)(1/2)(k_B T / \eta)^2 \right)}$$

$$\langle \tau \rangle = \tau(\eta) \left[1 + \frac{\pi^2}{6} r(r+2) (k_B T / \eta)^2 \right] \quad (5.13)$$

The same procedure leads to the expression:

$$\frac{\langle \tau^2 \rangle}{\langle \tau \rangle^2} = 1 + \frac{\pi^2}{3} r^2 (k_B T / \eta)^2 \quad (5.14)$$

When deriving Equations 5.13 and 5.14, we used approximate relations: $(1+\alpha)/(1+\beta) \approx 1+\alpha-\beta$ and $(1+\alpha)^2 \approx 1+2\alpha$ for $|\alpha| \ll 1$ and $|\beta| \ll 1$.

According to our estimates, the lowest Fermi level value for the materials we studied is $\eta \approx 0.25$ eV which corresponds to $n = 1 \times 10^{20} \text{ cm}^{-3}$. At room temperature ($T = 300^\circ\text{K}$) $k_B T = 0.0258$ eV, hence the small parameter, $(k_B T / \eta)^2$, value does not exceed 0.0106. Our analysis of the measured Seebeck coefficient showed that the scattering parameter value is not greater than 1 ($r \leq 1$). Thus, neglecting the second term in square brackets in Eq. 5.13 leads to an error which is not greater than 5%. For the films with $n = 5 \times 10^{20} \text{ cm}^{-3}$ the estimated inaccuracy is lower by an order of magnitude. The same inaccuracy comes from neglecting the second term in the right side of Eq. 5.14. Thus, with a sufficient precision we can transform equations 5.4 and 5.5 to the simple form:

$$\sigma = (nq^2 / m^*) \tau(\eta) \quad (5.15)$$

$$R_H = -(qn)^{-1} \quad (5.16)$$

To derive the final equation for the Seebeck coefficient starting with Eq. 5.6, we must use on Eq. 5.10. With the $\tau(E)$ dependence in the form of Eq. 5.12, one obtains:

$$S = -(k_B / q) (\pi^2 / 3) (r + 3/2) (k_B T / \eta) \quad (5.17)$$

To estimate possible inaccuracy that comes from the Sommerfeld approximation, we have to compare this formula with the exact equation valid for the isotropic and parabolic band for arbitrary degeneracy:

$$S = -\frac{k_B}{q} \left(\frac{(r+5/2)F_{r+3/2}(\eta^*)}{(r+3/2)F_{r+1/2}(\eta^*)} - \eta^* \right) \quad (5.18)$$

where $\eta^* \equiv \eta/k_B T$ and $F_s(\eta^*)$ is the so called Fermi integral:

$$F_s(\eta^*) \equiv \int_0^\infty \frac{x^s}{\exp(x - \eta^*) + 1} dx \quad (5.19)$$

Numerical calculations for scattering parameter $r=1$ using Equations 5.18 and 5.17 showed that for $\eta/k_B T \geq 10$ the difference between the two calculated values of S is less than 2%. In addition to the transport coefficients, we will need equations that relate carrier concentration to the Fermi level for further analysis.

For the parabolic and isotropic model the carrier concentration is described by the equation:

$$n = \frac{4\pi(2m^*)^{3/2}}{h^3} \int_0^\infty E^{1/2} f_o(E) dE$$

With integration by parts we can come to the form that allows us to apply the Sommerfeld approximation:

$$n = \frac{8\pi(2m^*)^{3/2}}{3h^3} \int E^{3/2} \left(-\frac{\partial f_o}{\partial E} \right) dE$$

Using the Sommerfeld approximation in the form of Eq. 5.11, one obtains:

$$n = \frac{8\pi(2m^*)^{3/2}}{3h^3} \eta^{3/2} \left[1 + \frac{\pi^2}{8} \left(\frac{k_B T}{\eta} \right)^2 \right] \quad (5.20)$$

The correction term in the square brackets is less than 1.3% for $\eta/k_B T \geq 10$, which is the case for materials we studied. Thus we can use the simplified formulas:

$$n = \frac{8\pi(2m^*)^{3/2}}{3h^3} \eta^{3/2} \quad (5.21)$$

and

$$\eta = \left(\frac{3}{8\pi} \right)^{2/3} \frac{h^2}{2m^*} n^{2/3} \quad (5.22)$$

Substituting the last expression for η in Eq. 5.17, we obtain a useful equation that relates the Seebeck coefficient to the carrier concentration, effective mass, scattering parameter and temperature:

$$S = -27.2(k_B/q) \frac{(r + 3/2)m^*}{h^2} (k_B T) n^{-2/3} \quad (5.23)$$

Now let us summarize the results presented above with respect to what information on the fundamental parameters of material can be obtained from the measurements of electrical conductivity, the Hall and Seebeck coefficients. Hall effect measurements provide the carrier concentration value:

$$n = -(qR_H)^{-1} \quad (5.24)$$

Combination of conductivity or resistivity, σ or ρ , and the Hall coefficient, R_H , gives a mobility, μ , value:

$$\mu = |R_H| \sigma \quad \text{or} \quad \mu = |R_H| / \rho \quad (5.25)$$

Based on Eq. 5.15, mobility can be defined as

$$\mu = \sigma / qn = q\tau(\eta) / m^* \quad (5.26)$$

Mean free path length of a carrier, l , is the product of a mean free path times (relaxation time), τ , and the carrier velocity, v : $l = \tau v$, hence

$$l(\eta) = \mu m^* v(\eta) / q = \mu P(\eta) / q,$$

where $P(\eta)$ is a momentum value for the electron with the energy equal to the Fermi energy. It can be easily calculated from the known carrier concentration using the formula:

$$P(\eta) = (3/8\pi)^{1/3} \hbar n^{1/3}$$

Thus the mean free path length can be determined by measurements of R_H and σ using any of the two equations below:

$$l(\eta) = (3/8\pi)^{1/3} \hbar \mu n^{1/3} / q \quad (5.27)$$

$$l(\eta) = (3/8\pi)^{1/3} \hbar \sigma |R_H|^{2/3} / q^{4/3} \quad (5.28)$$

The expression for the Seebeck coefficient (Eq. 5.23) contains three fundamental parameters of a material: effective mass, m^* , scattering parameter, r , and carrier concentration, n . If two of them are known, the third one can be determined from S measurement. In our study we used this equation to derive the scattering parameter which is a signature of the dominating scattering mechanism. Carrier concentration was determined by the Hall measurements, and effective mass value was determined from comparison of the Hall and plasma frequency measurements (see following sections).

5.1.3 AC Electrical Conductivity (Plasma and Collision Frequencies)

In this section we will consider the electrical current induced by a time-dependent (non-stationary) electric field. We will base our analysis on the approximations discussed in Sec. 5.1.1 and proved to be valid for the heavily doped SnO₂. Namely, the electron spectrum is continuous and isotropic; dissipation of momentum occurs due to scattering of electrons by defects or phonons; scattering processes can be treated in the relaxation time approximation; the electron gas is degenerate. The latter means that only the electrons with energy close to the Fermi energy contribute to the electrical transport, hence dynamic properties (effective mass, m^*) and collision time, τ , or collision frequency, $\omega_c=1/\tau$, are the same for all those electrons. These approximations enable us to use the Drude model, which is commonly and successfully used for the AC conductivity and optical properties analysis in metals.

The electric current density, \mathbf{j} , is defined as

$$\mathbf{j} = -nq\mathbf{P} / m^*, \quad (5.29)$$

where \mathbf{P} is a net momentum per electron. In the absence of electric field this net momentum and electric current are zero. To find \mathbf{P} the equation of motion is used:

$$d\mathbf{P}/dt = -q\mathbf{E} - \mathbf{P}/\tau \quad (5.30)$$

Writing the oscillating electric field in the form $\mathbf{E}(t) = \text{Re} [\mathbf{E}(\omega)\exp(-i\omega t)]$ and seeking a steady state solution of the form $\mathbf{P}(t) = \text{Re} [\mathbf{P}(\omega)\exp(-i\omega t)]$, we obtain current density as

$$\mathbf{j}(t) = \text{Re}[\mathbf{j}(\omega) \exp(-i\omega t)]$$

$$\mathbf{j}(\omega) = -nq\mathbf{P}(\omega)/m^* = -\frac{nq^2}{m^*} \left(\frac{\tau}{1 - i\omega\tau} \right) \mathbf{E}(\omega)$$

It is seen that conductivity, which is defined as $\sigma(\omega) \equiv \mathbf{j}(\omega)/\mathbf{E}(\omega)$, is a complex value and depends on frequency of the electric field:

$$\sigma = \frac{\sigma_o(\omega)}{1 - i\omega\tau}, \quad (5.31)$$

where

$$\sigma_o = q^2 n \tau / m^* \quad (5.32)$$

is a stationary (DC) electrical conductivity, according to Eq. (5.15).

Here we must make two remarks about the validity of the consideration above.

1. The magnetic field \mathbf{H} , which accompanies the \mathbf{E} field in an electromagnetic wave, was ignored in Eq. (5.30) because the term in \mathbf{H} is smaller than the term in \mathbf{E} by many orders of magnitude.
2. The \mathbf{E} field in an electromagnetic wave varies not only in time but also in space. The theory we present here is a local one which means that for each point \mathbf{r} within a conductor one can write $\mathbf{j}(\mathbf{r},t) = \sigma(\omega) \cdot \mathbf{E}(\mathbf{r},t)$. This approach is valid only if the wavelength λ of the field is large compared to the electron mean free path l . Our experimental studies of SnO₂ provided an estimated value of l not higher than 5-6 nm, while the wavelengths in our measurements were in the range from 250 to 2500 nm. Thus, the local theory approach is valid.

High electrical conductivity in metals and heavily doped semiconductors, and its dependence on frequency, significantly influences optical properties of these materials, in particular the transparency and reflectivity spectra. The wave equation contains a complex dielectric constant $\epsilon(\omega)$ with contribution both from bound and free (conductive) electrons. Based on Equations 5.31 and 5.32, one obtains the expressions for the real and imaginary parts of the dielectric constant:

$$\text{Re } \epsilon = \epsilon' = n^2 - k^2 = \epsilon_{\infty} \left(1 - \frac{\omega_p^2}{\omega^2 + \omega_c^2} \right) \quad (5.33)$$

$$\text{Im } \epsilon = \epsilon'' = 2nk = \epsilon_{\infty} \left(\frac{\omega_p^2 \omega_c}{\omega(\omega^2 + \omega_c^2)} \right) \quad (5.34)$$

Here n and k are refractive index and extinction coefficient respectively, and ϵ_{∞} is the "high-frequency" dielectric constant due to the bound electrons. There are also two characteristic parameters that are totally defined by free (conductive) electrons. Those are the collision frequency, $\omega_c = 1/\tau$, and the plasma frequency, ω_p , which is a natural frequency of oscillations of the electron gas as a whole. The latter is given by

$$\omega_p = [4\pi q^2 n / (m^* \epsilon_{\infty})]^{1/2} \quad (5.35)$$

When the frequency of an electromagnetic wave comes close to the plasma frequency, then reflectivity and transparency of the material can change dramatically. If $\omega_c \ll \omega_p$, then to the first approximation

$$\epsilon \approx \epsilon' = \epsilon_{\infty} (1 - \omega_p^2 / \omega^2)$$

When ε is real and negative ($\omega < \omega_p$) the solutions to the wave equation decay exponentially in material; i.e. no radiation can propagate. However, when ε is positive ($\omega > \omega_p$) solutions become oscillatory, and the conductor should become transparent. Thus at $\omega = \omega_p$ there should be observed a sharp change in reflectivity (and transmission) which is known as "plasma reflectivity edge" and also in transparency. For the real conductors, ω_c/ω_p is usually not so small, therefore reflectance does not change so sharply when frequency crosses the ω_p value. However analysis of the measured optical spectra allows us to determine plasma and collision frequencies. That provides an independent method for measurement of carrier concentration and mobility if the effective mass is known. Indeed (see Eq. 5.35),

$$n = \omega_p^2 m^* \varepsilon_\infty / 4\pi q^2 \quad (5.36)$$

As to mobility, it can be calculated based on the measured value of $\omega_c = 1/\tau$ and equation (5.26) so that

$$\mu = (q/m^*)/\omega_c \quad (5.37)$$

5.2 Experimental Results and Discussion

5.2.1 Plasma Frequency and Seebeck Coefficient in the Films with Varying Electron Concentration (Dependence of Energy on the Electron Momentum)

The objective of studies presented in this section is to determine the effective mass value and its dependence (or independence) on the carrier concentration. The effective mass knowledge is important for further analysis of mobility and scattering mechanisms.

As to the $m^*(n)$ dependence, it is an indicator of whether we can use the parabolic approximation, hence whether the formulas presented in Sec. 5.1 could be applied to this analysis.

To analyze influence of non-parabolicity it is convenient to describe the dependence of energy, E , on electron momentum, P , in the form:

$$P^2 = CE[1 + \Gamma(E)], \quad (5.38)$$

where C is a constant and $\Gamma(E)$ is a positive, dimensionless function of energy, which is zero at $E=0$ (at the band edge) and increases with energy.

The effective mass that appears in the equations for the transport coefficients and Fermi level-concentration relation, is defined by the equation

$$\frac{1}{m^*} \equiv \frac{1}{P} \frac{dE}{dP} \quad (5.39)$$

Limiting value of the effective mass when energy drops to zero is

$$\lim_{E \rightarrow 0} m^* \equiv m_0^* = C/2$$

hence Eq. 5.38 can be rewritten as

$$P^2 / 2m_0^* = E[1 + \Gamma(E)] \quad (5.40)$$

Within the energy range, where the contribution of Γ can be neglected (parabolic spectrum), the effective mass is constant and equal to m_0^* , the density of states function is

$$D(E) = 4\pi(2m_0^* / h^2)^{3/2} E^{1/2} \quad (5.41)$$

and the carrier concentration at high degeneracy is defined by

$$n = (8\pi/3)(2m_o^*/h^2)^{3/2}\eta^{3/2} \quad (5.42)$$

In the range of higher energies, where Γ value is not negligible, one has:

$$m^* = m_o^* [1 + \Gamma(E) + Ed\Gamma/dE] \quad (5.43)$$

$$D(E) = 4\pi(2m_o^*/h^2)^{3/2} E^{1/2} [1 + \Gamma(E) + Ed\Gamma/dE] \quad (5.44)$$

$$n = (8\pi/3)(2m_o^*/h^2)^{3/2}\eta^{3/2} [1 + \Gamma(\eta)]^{3/2} \quad (5.45)$$

The last equation is valid for high degeneracy, under the same condition as Eq. 5.42. Since $\Gamma(E) > 0$ and $d\Gamma/dE > 0$, the effective mass value increases with energy, density of states increases with energy more rapidly than in the parabolic case, as well as the carrier concentration does with the Fermi level. Vice versa, the Fermi level increases with carrier concentration slower than in the parabolic case.

Let us now consider how non-parabolicity influences the expressions for the transport coefficients presented and discussed in Sec. 5.1. The expressions obtained in the Sommerfeld approximation (Eq. 5.8) neglecting the term $\propto (k_B T/\eta)^2$, such as R , μ , and ω_p , preserve their form:

$$R_H = -(qn)^{-1} \quad (5.16)$$

$$\mu = \sigma/qn = q\tau(\eta)/m^*(\eta) \quad (5.26)$$

$$\omega_p = \sqrt{\frac{4\pi n q^2}{m^*(\eta)\epsilon_\infty}} \quad (5.35)$$

However, dependencies of these parameters on Fermi level or concentration become different and more complicated because of change in $\tau(E)$ dependence as well as that of

effective mass. In contrast, for the Seebeck coefficient it is essential to preserve the second term in the Sommerfeld approximation (see Eq. 5.10). The new equation for the Seebeck coefficient contains $\Gamma(E)$, $d\Gamma/dE$, and $d^2\Gamma/dE^2$ terms calculated at $E=\eta$. Thus, to analyze the Seebeck coefficient we need first determine the $\Gamma(E)$ function.

We did that by means of measuring and comparing R_H and ω_p values on the series of the SnO_2 films with different doping levels. As the carrier concentration increases, the Fermi level goes up in energy, no matter whether the band is parabolic or not. The carrier concentration in this series of the samples determined by Hall measurements varied in a range of 1×10^{20} to $5 \times 10^{20} \text{ cm}^{-3}$, which provided considerable variation in the Fermi level position. Because of rather high n value and also based on thermopower measurements, one could conclude that the electron gas in all the samples is highly degenerate, so that we may use equations 5.16 and 5.35. The latter enabled us to determine the effective mass value from a measured value of ω_p using the n value determined from R_H , and high frequency dielectric constant, ϵ_∞ , which is very close to 4, according to the literature data and our own ellipsometry measurements.

Figure 5.1 presents $m^*(n)$ dependence determined in this way. It is seen that within the spread of the experimental points the m^* value is constant, which means that no considerable deviation from parabolicity takes place for our material in the carrier concentration range indicated above (and also in corresponding range of the electron energies). This is a very important result, which enables us to use the simple parabolic band theory in further analysis of the experimental data.

The effective mass value determined is $m^*=(0.28\pm 0.03)m_0$. According to [55] the longitudinal and transverse effective mass components (that is parallel and perpendicular to the revolution axis of the ellipsoidal constant energy surface) are: $m_{\parallel}^*=0.234m_0$ and $m_{\perp}^*=0.299m_0$. When averaged properly over all directions, that provides the value of the so called "effective mass of conductivity", m_c^* , which defines the plasma frequency and mobility for the ellipsoidal constant energy surface:

$$\frac{1}{m_c^*} = \frac{1}{3} \left(\frac{1}{m_{\parallel}^*} + \frac{2}{m_{\perp}^*} \right)$$

The result of calculation is: $m_c^*=0.274m_0^*$. It should be noted, that for the ellipsoidal constant energy surface the so called "density of states effective mass", m_d^* , is defined by

$$m_d^* = (m_{\parallel}^* m_{\perp}^{*2})^{1/3}$$

This mass is that included in the expressions for density of states, carrier concentration and Seebeck coefficient. Calculated for the same effective mass components, $m_d^*=0.276m_0$. Thus, m_d^* and m_c^* values coincide with each other closely and with our experimental m^* value. This verifies the isotropic spectrum approximation that we will use. We assume the effective mass value to be $0.275m_0^*$.

An independent confirmation of the parabolicity comes from the Seebeck coefficient, S , dependence on carrier concentration. The Seebeck coefficient, S , is proportional to $n^{-2/3}$ for parabolic bands in the case of high degeneracy. For the non-parabolic band $S(n)$ dependence changes and becomes more complicated.

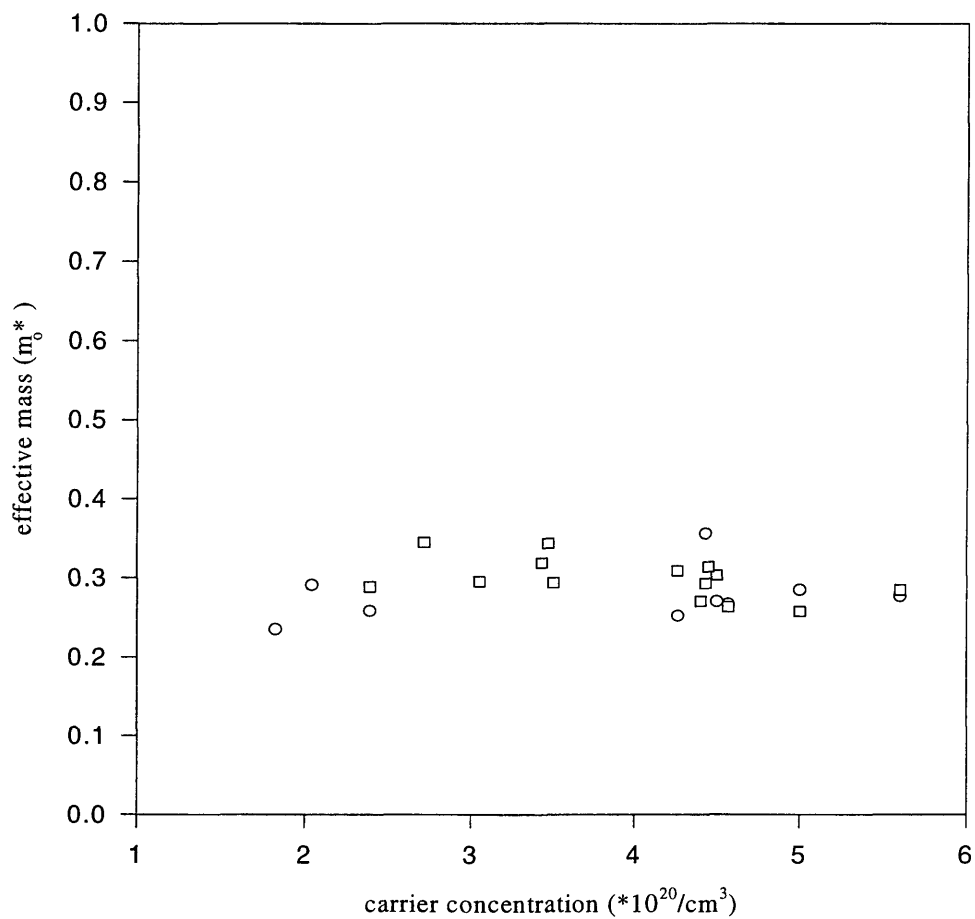


Figure 5.1 Plasma frequency from both ellipsometry (o) and reflection measurements (□) against carrier concentration for some tin oxide films.

As seen from Figure 5.2, the experimental dependence obtained by us is very close to $n^{-2/3}$.

Using Eq. 5.23 and the effective mass value indicated above we calculated the scattering parameter (τ) value (see Figure 5.3). The latter will be used in Sec. 5.2 for identification of the scattering mechanism.

5.2.2 Resistivity and Mobility (Influence of the Grain Boundaries)

A significant difference is usually observed between mobility ($\mu=[qpn]^{-1}$) values measured on single crystal and polycrystalline samples of the same material (the same composition, carrier concentration, etc.). For example, resistivity measured on CdS or CdTe polycrystalline films could be by several orders of magnitude higher than that for single crystals. This difference is usually attributed to the influence of the grain boundaries (GB). Electronic properties of the material in the GB region may be significantly different from those in the bulk of the grains. Deep electronic levels that exist at the interface between two grains trap the majority carriers and hence acquire some electrical charge, which provides a potential barrier for the majority carriers. Thus the GB behaves like two Schottky diodes connected back-to-back.

It is common to treat the problem of the GB influence on resistance in terms of "GB-scattering". This terminology is not always correct and sometimes can be misleading. Indeed, frequency of scattering, $1/\tau$, is an important parameter that in combination with the effective mass determines the mobility value. Carriers are scattered by impurities, point

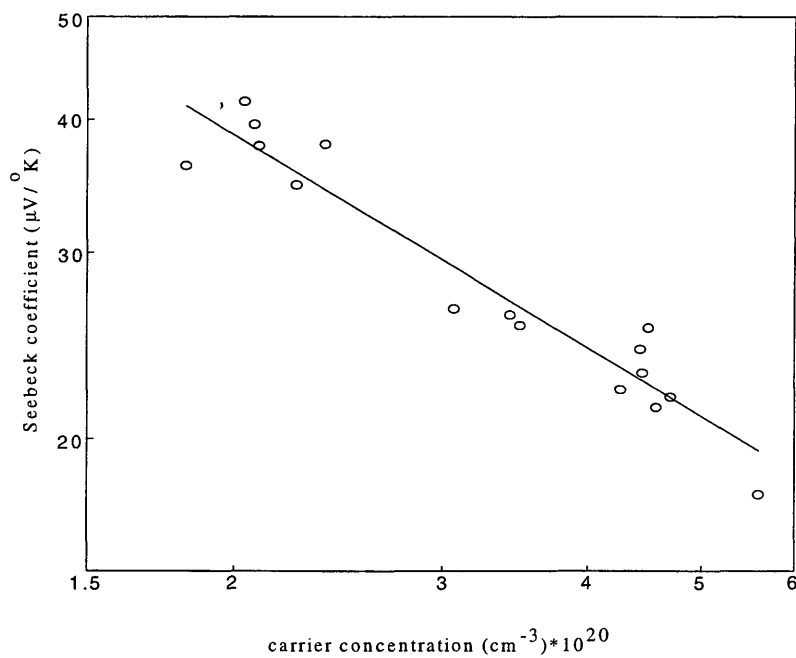


Figure 5.2. Carrier concentration versus Seebeck coefficient for tin oxide samples where the straight line represents the best fitting

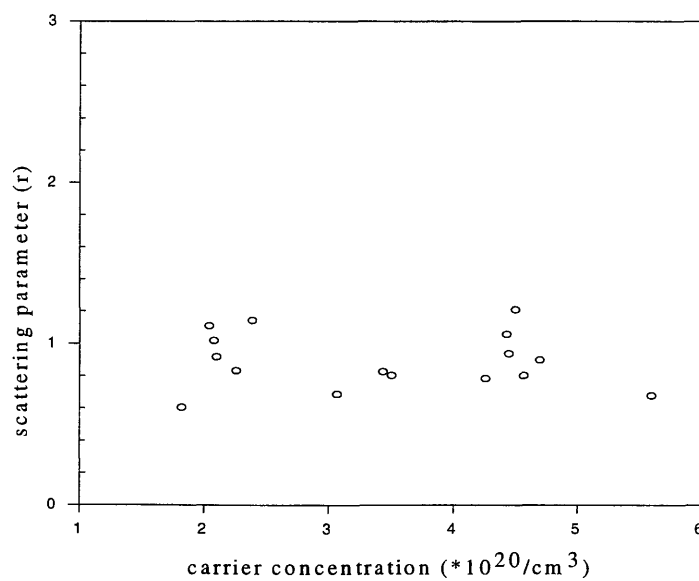


Figure 5.3. Carrier concentration versus scattering parameter for tin oxide samples.

defects, dislocations, by phonons (scattering in the grain bulk, or B-scattering) and also by GB (GB-scattering). For several coexisting scattering mechanisms, the total collision frequency is the sum of the partial ones:

$$1/\tau = 1/\tau_1 + 1/\tau_2 + 1/\tau_3 + \dots = 1/\tau_B + 1/\tau_{GB}$$

The individual contribution of the GB scattering can be evaluated by comparison of $1/\tau_{GB}$ and total scattering frequency, $1/\tau$. For this purpose it is convenient to rewrite the previous equation in terms of mean free paths, $l_i = \tau_i v$. Velocity, v , for high degeneracy is the Fermi velocity which is the same for all the electrons. Thus

$$1/l = 1/l_B + 1/l_{GB}$$

where l_B is a free path for the B-scattering and l_{GB} is that for the GB-scattering. The latter is of the order of the grain size, d_G , and the l value can be calculated based on the carrier concentration and mobility data by using Eq. 5.27. The highest l value we obtained in this way is about 50 \AA , while the grain size in our films is in the 10^3 \AA scale. Thus $1/l \gg 1/l_{GB} \sim 1/d_G$, hence the GB-scattering can be neglected, and we must use some different approach to discussion of the GB influence on the sample resistivity.

Next we can model the polycrystalline material as a two-phase system. One phase is the material inside grains (bulk material), and the second (high resistivity) phase is the material in the GB region. When traveling through the sample under the influence of the electric field, an electron is crossing a grain, then GB, another grain, and so on. Hence the electrical circuit of the sample may be represented by series connection of resistors, R_B and R_{GB} , representing bulk material and GB, respectively. When measuring DC resistivity,

with either the four probe or van der Pauw method, we measure the sum of these two types of resistances. Thus the Hall mobility in general should be lower or at least the same as the real bulk mobility:

$$\mu_H \approx \frac{\mu_B}{1 + R_{GB}/R_B} \quad (5.46)$$

Mobility can be also determined by using the effective mass and collision time (momentum relaxation time) value, the latter determined as $\tau = (\omega_c)^{-1}$:

$$\mu_{opt} \approx \frac{q\tau}{m^*} = \frac{q}{m^* \omega_c} \quad (5.47)$$

Table 5-1. Comparison of the Hall and optical mobility values.

Sample #	Thickness (nm)	Hall carrier conc. (10^{20}cm^{-3})	mobility (cm^2/Vs)	
			μ_H	μ_{opt}
1	110	5.9	4.5	21
2	60	4.0	4.5	32
3	90	2.4	3.3	29
4	730	2.3	12	24
5	370	5.6	25	26
6	500	4.6	29	30
7	470	3.1	11.5	12

We call this mobility value (Eq. 5.47), calculated with τ determined from optical measurements, the optical mobility. Collision frequency is the actual frequency of scattering and is influenced by grain boundaries only if l_{GB} and l_B values are comparable, which is not the case for our films as shown above. Thus $\mu_{opt} \approx \mu_B$.

Table 5-1 presents the Hall and optical mobility values for several typical films. It is seen that for the first three samples μ_H is significantly smaller than μ_{opt} which indicates a significant influence of the grain boundaries, while for the last three these values are practically the same, within the accuracy of measurements and modeling. For these films, the contribution of the GB to the measured resistivity can be neglected. The data on the films like these will be used for the analysis of the bulk scattering mechanism.

5.2.3 Bulk Scattering Mechanism

To identify the scattering mechanism we will start with the well known and widely used signatures of the scattering mechanisms, such as the temperature dependence of mobility and scattering parameter, which is defined by Eq. 5.12.

The temperature dependence of mobility is defined by two factors. The first one comes from the temperature dependence of the density of scatterers. It is clear that for scattering by impurities and crystal structure defects the scatterer density does not depend on temperature. This dependence exists only for scattering by phonons whose concentration increases with temperature. The second factor is defined by two issues: (a) relaxation time dependence on energy and (b) temperature dependence of the energy of the

carriers that contribute mostly to the transport, $\langle E \rangle$. For the non-degenerate carrier gas (classical statistics) this energy is proportional to temperature: $\langle E \rangle \sim k_B T$. For high degeneracy $\langle E \rangle \approx \eta$ and to the first approximation the Fermi level dependence on temperature should be neglected.

Relaxation time dependencies on energy (hence, scattering parameter) and on temperature for various scattering mechanisms were studied theoretically and believed to be defined precisely for the parabolic band model, e.g. see [39 and 54]. Below are presented scattering parameter values and temperature dependencies of mobility (the latter for high degeneracy) predicted by theory for the most common scattering mechanisms.

Acoustic phonon scattering:

$$r = -1/2, \mu \propto T^{-1};$$

Optical phonon scattering:

For temperature below Einstein temperature, Θ_E , $r=0$, $\mu \propto \exp(t/\Theta_E)$

For temperature well above Θ_E , $r=1/2$, $\mu \propto T^{-1}$;

Scattering by the neutral hydrogen-like impurity centers:

$$r = 0, \mu \propto T^0;$$

Scattering by point defects with the $\delta(r)$ -type scattering potential:

$$r = -1/2, \mu \propto T^0;$$

Scattering by impurity ions with q/r-type Coulomb scattering potential:

$$r = 3/2, \mu \propto T^0;$$

We have measured Hall mobility in temperature range of 300 to 500°C using our Hall system. No dependence on temperature was found. Based on this result we must exclude from consideration all the phonon scattering mechanisms and focus on scattering by defects/impurities. For high carrier concentrations like those in our samples, the most probable mechanism is scattering by impurity ions because the number of impurity sites is of the same order as the number of the free carriers, or even higher if there is some compensation. To check this assumption we must look at the scattering parameter. Its value determined from Seebeck coefficient measurements is presented in Sec. 5.2.1, Figure 5.3. The value obtained ($r=0.89\pm 0.17$) is higher than the predicted ones for all the mechanisms listed above, except ion impurity scattering. At the same time our scattering parameter value is lower than that indicated above for this mechanism. The discussion below is aimed at explanation of this discrepancy.

The Coulomb scattering potential of the impurity ion is screened due to:

1. Polarization of the electronic shells of the atoms surrounding the impurity atom; dielectric constant corresponding to this screening mechanism is the high-frequency dielectric constant, ϵ_∞ ; its value for SnO₂ is close to 4.
2. Polarization of the lattice (displacement of the lattice ions toward and outward the impurity ion), characterized by ϵ_L component.
3. Screening by free carriers (SFC): free carriers are pulled closer to impurity ion (if their charge sign is opposite to that of impurity ion) or pushed out (if the charge signs are the same).

In insulators or slightly doped semiconductors the third mechanism of screening can be neglected and the screened Coulomb potential of an impurity atom is described by

$$|U| = \frac{|Q|}{\epsilon_0 r} \quad (5.48)$$

where U is the magnitude of scattering potential, Q is the magnitude of the impurity ion charge, r is a distance from the center of the impurity ion, and $\epsilon_0 = \epsilon_\infty + \epsilon_L$ is a static dielectric constant. In SnO_2 $\epsilon_0 \approx 10$. In metals or heavily doped semiconductors the SFC mechanism can play a significant role and the scattering potential is described by:

$$|U| = \frac{|Q|}{\epsilon_0 r} \exp(-r/r_0) \quad (5.49)$$

where r_0 is the screening radius for SFC which is defined for highly degenerate semiconductors by

$$r_0 = \sqrt{\left(\frac{\epsilon \hbar^2}{16\pi^2 m^* q^2} \right) (\pi/3n)^{1/3}} \quad (5.50)$$

The difference between Equations 5.48 and 5.49 leads to the difference in scattering parameter value for the Coulomb potential screened and unscreened with free carriers. To calculate the r -value for our materials we will use the theory developed in [58-61]. The dependence of relaxation time on energy for scattering by the impurity ions with SFC can be written in the form:

$$\tau(E) = \left(\frac{\epsilon^2 \sqrt{2m^*}}{\pi q^4 N_i \Phi(E_F)} \right) E^{3/2} \quad (5.51)$$

where

$$\Phi(E_F) = \ln(1 + \xi) - \frac{\xi}{1 + \xi}; \quad \xi = (2k_F r_o)^2 \quad (5.52)$$

$$k_F = (3\pi^2)^{1/3} n^{1/3} \quad (5.53)$$

$$r_o = 3.65 \times 10^{-5} \varepsilon^{1/2} (m_o / m^*)^{1/2} n^{-1/6} \quad (5.54)$$

Function $\Phi(\xi)$ in Eq.5.51 reflects the influence of SFC, k_F (Eq. 5.53) is the Fermi wave vector magnitude, and Eq. 5.54 is the expression for the screening radius obtained by rewriting Eq. 5.50. Based on Equations 5.51-5.54 and on the definition of scattering parameter, $r \equiv d \ln \tau / d \ln E \big|_{E=\eta}$ (see Eq.5.12), it is easy to obtain the expression for the scattering parameter for the scattering mechanism under consideration:

$$r = \frac{3}{2} - \frac{d \ln \Phi}{d \ln \xi} \bigg|_{E=\eta} = \frac{3}{2} - \frac{\xi^2}{(1 + \xi)^2} \frac{1}{\Phi(\xi)} \quad (5.55)$$

We can calculate the scattering parameter for $n=1 \times 10^{20} \text{ cm}^{-3}$ and $n=5 \times 10^{20} \text{ cm}^{-3}$, $m^*=0.275m_o$, and $\varepsilon=\varepsilon_o=10$.

$$\underline{n=1 \times 10^{20} \text{ cm}^{-3}}: \eta=0.26 \text{ eV}; k_F=1.5 \cdot 10^7 \text{ cm}^{-1}; r_o=10.2 \text{ \AA} \Rightarrow \underline{r=0.9}$$

$$\underline{n=5 \times 10^{20} \text{ cm}^{-3}}: \eta=0.76 \text{ eV}; k_F=2.5 \cdot 10^7 \text{ cm}^{-1}; r_o=7.5 \text{ \AA} \Rightarrow \underline{r=1.0}$$

The obtained values of the scattering parameter are close to those obtained from the Seebeck coefficient data (see Sec. 5.2.1). At the same time, based on the values of screening radius, r_o , one can see an additional problem to be discussed. Indeed, due to the screening by free carriers the scattering potential (see Eq. 5.49) turned out to be localized in the region of the order of the unit cell. If so, the problem is what dielectric constant value

should be used when calculating r_0 and τ . The screening effect caused by displacement of the lattice ions (Sn^{+4} and O^{-2}) depends on how many coordination spheres are involved in the ionic screening. To provide the effect corresponding to the "static dielectric constant", ϵ_0 , the ion displacement must occur in many unit cells surrounding the impurity atom. This is not the case if the perturbing potential is located in the region close to one unit cell. Thus we must suggest that the effective dielectric constant that should be put in our calculations is lower than ϵ_0 . Therefore we repeated the calculations of r_0 and scattering parameter using $\epsilon = \epsilon_\infty = 4$. The results are as follows:

$$\underline{n=1 \times 10^{20} \text{ cm}^{-3}}: \eta=0.26 \text{ eV}; k_F=1.5 \cdot 10^7 \text{ cm}^{-1}; r_0=6.5 \text{ \AA} \Rightarrow \underline{r=0.7}$$

$$\underline{n=5 \times 10^{20} \text{ cm}^{-3}}: \eta=0.76 \text{ eV}; k_F=2.5 \cdot 10^7 \text{ cm}^{-1}; r_0=4.8 \text{ \AA} \Rightarrow \underline{r=0.8}$$

It is seen that the scattering parameter does not change considerably and stays close to the experimental value. The real effective dielectric constant should be somewhere between ϵ_0 and ϵ_∞ , hence the scattering parameter value between values calculated for the limiting ϵ values. Thus one can conclude that the dominating bulk mechanism of scattering is the scattering by impurity ions screened with free carriers.

5.2.4 Calculation of Mobility in the Bulk of the Grains

Studies presented above provided us with the information that allows calculating the carrier mobility and comparing the calculated and measured data. For calculations the equation

$$\mu = q\tau(\eta) / m^*(\eta) \quad (5.26)$$

was used where the effective mass was assumed to be isotropic, independent on carrier concentration (hence on η) and equal to $0.275 m_0$. Relaxation time, which generally depends on carrier concentration that is on η , was calculated by using Eqs. 5.51-5.54. Carrier concentration was assumed to be $=5 \times 10^{20} \text{cm}^{-3}$ which is close to that for the best SnO₂ TCO samples. Fermi energy value, η corresponding to this concentration, calculated by using Eq. 5.22; is equal to 0.76 eV. Because of the uncertainty in the effective dielectric constant value (due to the spatial dispersion) mentioned above, we calculated μ value for different ϵ in the range from ϵ_∞ to ϵ_0 . The results of calculations are presented in Table 5-2. We assumed no compensation, that is the density of scatterers, N_i in Eq. 5.51, is equal to the carrier concentration.

It is seen from the table that (a) the SFC screening radius, r_0 , is really small, hence we need to use dielectric constant value lower than ϵ_0 , and (b) mobility calculated with $\epsilon=5$ is close to the experimental data (around $30 \text{ cm}^2/\text{Vs}$). If the measured mobility is so close to theoretically calculated, then one may conclude that the achieved level of mobilities is close to the limiting one, and there is not much room for the mobility increase by improvement of processing technology. A conclusion of this kind would be of great importance for industry if there were not some uncertainty about the dielectric constant value that should be used for calculation of mobility.

Another source of uncertainty is the compensation problem. One can not be sure that the compensation degree for the samples we studied experimentally was zero. If the

Table 5-2. Calculated mobility as a function of dielectric constant
 $n=5 \times 10^{20} \text{ cm}^{-3}$; compensation degree $\beta=0$

ϵ (Å)	r_o	μ (cm ² /V·s)
10	7.2	83
8	6.7	60
6	5.8	40
5	5.3	32
4	4.8	23

compensation is considerable, then in our calculations of mobility we must use the density of the scatterers greater than the carrier concentration. Indeed,

$$n=N_d-N_a \text{ and } N_i=N_d+N_a,$$

where N_d , N_a , and N_i are the densities of donors, acceptors and impurity ions, respectively.

If we designate the compensation degree as $\beta \equiv N_a/N_d$, and mobility in the non-compensated material ($\beta=0$) as μ_o , then the mobility in compensated material with the same carrier concentration, μ , can be written as

$$\mu = \mu_o \left[\frac{1-\beta}{1+\beta} \right] \quad (5.56)$$

It is seen from this equation that even for a not significant compensation degree, the measured value of mobility could be considerably lower than that for the uncompensated material with the same carrier concentration. For example, for $\beta=0.2$ $\mu/\mu_o=0.67$ and for

$\beta=0.5$ $\mu/\mu_0=0.33$. Table 5-3 shows the calculated decrease in mobility due to increase in compensation degree for the given donor concentration.

Table 5-3. Calculated ratio of mobilities in compensated and non-compensated SnO₂ for the same donor concentration, $N_d=5 \times 10^{20} \text{ cm}^{-3}$.

Comp. degree (β)	Carrier Conc. (n) 10^{20} cm^{-3}	μ_β / μ_0
0.0	5	1
0.2	4	0.7
0.4	3	0.48
0.6	2	0.3
0.8	1	0.15

Unfortunately our deposition system did not permit precise control of the fluorine dopant content. We also could not measure directly donor and acceptor concentrations in the prepared films. However as an indirect evidence of the compensation influence we will present below the data on mobility for several samples with different carrier concentrations.

To exclude a possible influence of grain boundaries we selected samples for which the Hall and optical mobilities differ only slightly from each other (less than 7%). We compared two groups of samples prepared at different times and under slightly different conditions. The first group consists of three samples with almost the same parameters: thickness (averaged thickness $\langle t \rangle = 450 \text{ nm}$), carrier concentration ($\langle n \rangle = 5.3 \times 10^{20} \text{ cm}^{-3}$), and

mobility ($\langle\mu\rangle=29.6 \text{ cm}^2/\text{Vs}$). The other group also consists of three samples with common parameters and is characterized by $\langle t \rangle=510 \text{ nm}$, $\langle n \rangle=3.1 \times 10^{20} \text{ cm}^{-3}$, and $\langle\mu\rangle=12.6 \text{ cm}^2/\text{Vs}$. Calculation of mobility based on the assumption of zero compensation for both groups leads to a mobility value higher for the first group by only about 10 % because of higher concentration and more pronounced SFC. Let us now suppose that compensation is absent in the first group ($N_{d1}=n_1$), and the donor concentration in the second group is the same as in the first one ($N_{d2}=N_{d1}=N_d$). If so, compensation is the only reason why in the second group carrier concentration is lower, and compensation degree can be estimated as $\beta=(N_d-n_2)/N_d=(n_1-n_2)/n_1=0.42$. According to calculations like those presented in Table 5-3, the ratio of mobilities should be: $\mu_2/\mu_1=0.45$ which is in a good agreement with the experimental ratio, 0.425.

If all the samples we studied experimentally were compensated, then we must compare the theoretically calculated mobility with the measured value corrected by a factor $(1+\beta)/(1-\beta)>1$. In this case, the coincidence of the calculated and corrected experimental data will take place at higher values of the effective dielectric constant, ϵ . Thus there are two sources of the uncertainty when calculating mobility: (a) spatial dispersion of dielectric constant that should be analyzed theoretically in the future studies; (b) possible influence of compensation which should be studied experimentally.

5.3 Summary

- Studies presented in this chapter were aimed at determination of the fundamental parameters of SnO₂ thin films, such as dependence of electron energy on the electron momentum, dominating scattering mechanism, mobility and the factors that influence its value. For this purpose the following things were done.
- The theory of electron transport phenomena was analyzed to formulate and explain our approaches to the fundamental parameters studies. Various approximations of the theory were discussed; their validity with respect to the specific properties of the heavily doped SnO₂ was substantiated based on the literature data and results of our own studies. The final formulas were presented and analyzed.
- A variety of characterization methods and techniques were used for the experimental studies of SnO₂ films, including resistivity, Hall and Seebeck effects measurements, optical spectroscopy, and multi-angle spectral ellipsometry.
- These measurements provided an information on characteristics of the electron system in our samples: carrier concentration, mobility, scattering parameter, and plasma and collision frequencies.
- By comparison of the carrier concentration and plasma frequency the effective mass was determined. Its value was constant in a wide range of carrier concentrations/ Fermi energies, which indicates validity of the parabolic band model.

- It was shown that for the films with a grain size in the range of thousands of Angstroms, scattering of the electrons by the grain boundaries can be neglected compared to the scattering in the bulk of the grains.
- The individual contribution of the grain boundaries to the measured electrical resistance was estimated. The method is based on comparison of the Hall and optical mobilities (the latter is calculated by using collision frequency). It was found that for the high quality films (large grain size, high carrier concentration) this contribution is negligibly small.
- It was shown that the dominating scattering mechanism in the grain bulk is scattering by impurity ions screened with free carriers. The estimations of screening radius indicated that the spatial dispersion of the dielectric constant should be taken into account when making the theoretical calculations of mobility.
- It was demonstrated that compensation of donors with unintentionally induced acceptors could significantly influence the film mobility. To provide sheet resistance of the SnO₂ TCO thin films as low as possible one must eliminate compensating acceptor centers.

CHAPTER 6

MAJOR RESULTS, CONCLUSIONS, AND RECOMMENDATIONS

1. A reproducible APCVD process to fabricate heavily doped tin oxide thin films has been developed. Deposition conditions and the system design were reconsidered and improved based on both experiments and the computational fluid mechanics modeling. These results were used for designing a pilot APCVD system for a large area (13"×13") TCO thin films production.
2. TCO SnO₂ thin films on soda lime glass substrates were fabricated with spectral transparency and sheet resistance close to those for the best commercially available (Nippon Glass) materials. An averaged transparency of 82% in the wavelength range of 500 nm to 900 nm and sheet resistance of 8 Ω/\square were achieved.
3. A variety of methods and instruments were used to characterize structural, optical and electrical properties of the films. Those included SEM, AFM, XRD, surface profiling, spectrophotometer, multiangle spectroscopic ellipsometry, and measurements of Hall effect, electrical resistance and Seebeck effect (thermopower). Equipment for thermopower measurement and Seebeck coefficient mapping over the area of a thin film of arbitrary size and shape was designed and built.

4. The alternative methods for determining carrier concentration and mobility were developed based on measurements of transport coefficients and optical properties. Comparative studies of the Hall coefficient, Seebeck coefficient and plasma frequency provided empirical correlation between the two last parameters and carrier concentration. Mobility, which is usually measured by the Hall effect and electrical resistance measurements, was also determined by measurement of collision frequency provided by ellipsometry in our studies. Comparison of the Hall and optical mobilities were used to separate the individual contributions of grain boundaries and bulk material to the film electrical resistance.
5. By means of measurements and combined analysis of optical and electrical properties the fundamental characteristics of the electron system were studied. An effective mass determined from carrier concentration and plasma frequency measurements did not manifest any significant dependence on carrier concentration in the range of $n \approx 1 \times 10^{20}$ to $5 \times 10^{20} \text{ cm}^{-3}$. That means that no considerable deviations from parabolicity of the electron spectrum takes place, and the simplest parabolic model can be used for the analysis of the electronic properties. This conclusion was confirmed by the Seebeck coefficient dependence on concentration. The value of effective mass turned out to be very close to the most reliable literature data: $m^* \approx 0.28 m_0$.
6. By comparing the Hall and optical mobility it was found that for the films with high carrier concentration and not too small grain size, contribution of grain boundaries to the measured film resistance could be neglected. Theoretical analysis of the bulk

mobility data and scattering parameter derived from the Seebeck coefficient showed that the dominating scattering is by the impurity ion Coulomb potential screened by free carriers.

7. When analyzing the theoretical limit of mobility, it was shown that there are two sources of the uncertainty. The first is the spatial dispersion of the dielectric constant. It should be taken into account when the scattering potential of the impurity is confined to the region of the order of unit cell size due to the strong screening by free carriers. The other issue is the compensation of donor dopant by uncontrollable acceptor levels, probably induced by native defects (self-compensation mechanism). Numerical estimations showed that even a moderate compensation degree leads to a considerable decrease in mobility.

Based on the results of this research some recommendations could be made regarding future studies in this area.

1. Development of the experimental methods and characterization techniques suitable to studies of TCOs should be continued and intensified. In particular it seems worthy to combine the methods used in this research with a method proposed by Dr. V. Kaydanov and realized in Dr. T. Coutts group at NREL. The latter is based on simultaneous studies of four transport coefficients: Hall, Seebeck, Nernst-Ettingshausen and resistivity, in wide ranges of carrier concentration and temperature.
2. When developing these methods, great attention should be paid to the methods that can be used for routine characterization of materials not only in scientific laboratories but

also in commercial manufacturing. As an example, for non-destructive characterization of carrier concentration and its mapping over the area of arbitrary size and shape, the thermoelectric (Seebeck) diagnostics seems very attractive. Ellipsometry seems very promising, since it is able to provide data on numerous parameters of thin film and multilayer structures.

3. Better understanding of fundamental properties of TCOs, in particular, factors that define mobility value could be achieved by applying the same experimental methods and approaches to the data treatment and analysis for various TCO materials. Those should include the widely used tin oxide, ITO and ZnO, as well as other perspective materials like cadmium stannate, zinc-cadmium stannate and others.
4. For numerical estimation of the theoretical limit for mobility (and sheet resistivity) it is important to perform the theoretical analysis of the influence of spatial dispersion of dielectric constant. Maybe even more important, though more difficult, is to develop reliable and precise experimental methods for detection and quantitation of the compensation degree in heavily doped TCOs.
5. APCVD has demonstrated its potential for fabricating tin oxide TCO films both in laboratory and commercial manufacturing. It is reasonable to investigate advantages and shortcomings of this method with respect to other TCOs. When optimizing the doping methods it is important to provide not only optimal carrier concentration, but also as low a compensation degree as possible. The latter is one direct way to increase mobility.

REFERENCES CITED

1. C. G. Granqvist, *Appl. Phys.*, A, 19 (1993) 57.
2. G. Haacke, *J. Appl. Phys.*, 47 (1976) 4086.
3. T. J. Coutts, *Transparent Conducting Oxides: Their fabrication, Properties, Applications and Science*, American Vacuum Soc., Short course, Aug. 20, 1991, Denver, Co.
4. R. G. Gordon, NREL/SNL 14th PV Program Review meeting, Lakewood, (1996).
5. F. Simonis, M. van der Leij and C. J. Hoogendoorn, *Solar Energy Mater.*, 1 (1979) 221.
6. N. W. Ashcroft and N. D. Mermin, *Solid State Physics*, Sanders College Publishing, Fort Worth, 1976.
7. E. Burstein, *Phys. Rev.* 93 (1954) 632.
8. T. S. Moss, *Proc. Phys. Soc. A*, 382 (1954) 775.
9. K. L. Chopra, *Thin Solid Films*, 102 (1983) 1.
10. J. Y. W. Seto, *J. Appl. Phys.*, 46 (1975) 5247.
11. Z. M. Jarzebski and J. P. Marton, *J. Electrochem. Soc.* 123 (1976) 199c.
12. G. Sanon, R. Rup and A. Mansingh, *Thin Solid Films*, 190 (1990) 287.
13. *Selected Powder Diffraction Data for Metal and Alloys*, International Centre for Diffraction Data, Pennsylvania, 1978.

14. Ya. Kuznetsov, *Sov. Phys. Solid State*, 2 (1960) 30.
15. E. Shanthi, A. Banerjee, V. Dutta and K. L. Chopra, *J. Appl. Phys.*, 53 (1982) 1615.
16. D. Belanger, J. P. Dodelet, B. A. Lombos and J. I. Dickson, *J. Electrochem. Soc.* 132 (1985) 1398.
17. J. Prosvic and R. Gordon, *Thin Solid Films*, 214 (1992) 175.
18. T. Muranoi and M. Furukoshi, *Thin Solid Films*, 48 (1978) 309.
19. M. Kojima, H. Kato, A. Imai, and A. Shida, *J. Appl. Phys.*, 64 (1988) 1902.
20. J. S. Maudes and Rodriguez, *Thin Solid Films*, 69 (1980) 183.
21. J. C. Manificier, *Thin Solid Films*, 90 (1982) 297.
22. C. Manificier and J. P. Fillard, *Thin Solid Films*, 77 (1981) 67.
23. K. B. Sundaram and G. K. Bhagrat, *J. Phys. D: Appl. Phys.*, 16 (1983) 69.
24. *Handbook of Chemistry and Physics 45th Edition*, The Chemical Rubber Co., Ohio, 1964.
25. H. de Waal and F. Simonis, *Thin Solid Films*, 77 (1981) 253.
26. K. Sato, K. Adachi, Y. Hayashi and M. Mizuhashi, *Proc. of 20th IEEE, Las Vegas* (1988) 267
27. J. C. Manificier, L. Szepessy, J. F. Bresse, M. Perotin and R. Stuck, *Mater. Res. Bull.*, 14 (1979) 163.
28. Z. M. Jarzebski and J. P. Marton, *J. Electrochem. Soc.*, 123 (1976) 333c.
29. G. N. Advani, A. G. Jordan, C. H. P. Lupis, and R. L. Longini, *Thin Solid Films*, 62 (1979) 361

30. M. Mizuhashi, *J. Non-Crystal. Solids*, 38&39 (1980) 329.
31. E. Shanti, V. Dutta, A. Banerjee, and K. L. Choopra, *J. Appl. Phys.*, 51 (1980) 6243.
32. B. D. Cullity, *Elements of X-Ray Diffraction*, Addison-Wesley, Reading, MA 1978.
33. D. K. Schroder, *Semiconductor Material and Device Characterization*, John Wiley & Sons, Inc., USA 1990.
34. N. Cusack and P. Kendall, *Proc. Phys. Soc.*, 72 (1958) 898.
35. R. B. Roberts, *Philos. Mag.*, 36 (1977) 91.
36. M. J. Laubitz, T. Matsumura, and P. J. Kelly, *Can. J. Phys.*, 54 (1976) 92.
37. H. M. Ahmad and D. Greig, *J. Phys. (Paris)*, 35 (1974) C4-223.
38. *The Temperature Hand Book*, Vol. 29, Omega Engineering, Inc. 1995.
39. V. I. Kaydanov, *Thin Film Thermolement: Physics and Application*, House Nauice, Moscow, 1985.
40. W. P. Mulligan, *A study of the Fundamental Limits to Electron Mobility in Cadmium Stannate Thin Films*, Ph.D. thesis. Dept. of Material Science. Colorado School of Mines.
41. Y. Qu, *A Study of Transparent Zinc Oxide Thin Films*, Ph.D. thesis. Dept. of Physics. Colorado School of Mines.
42. *A Short course in Ellipsometry*, © J. A. Woollam Co., Inc.
43. O. J. Heavens, *Optical Properties of Thin Solid Films*, Dover Publications, Inc., New York, 1991.
44. R.N. Ghoshtagore, *J. Electrochem. Soc.* 125 (1978) 110.

45. B.J. Baliga and S. K. Ghandi, *J. Electrochem. Soc.* 123 (1976) 941.
46. C. G. Borman and R. G. Gordon, *J. Electrochem. Soc.* 136 (1989) 3820.
47. O. Tabata, T. Tanaka, M. Waseda and K. Kinuhara, *Surf. Sci.* 86 (1979) 230.
48. J. Kane, H. P. Schweizer and W. Kern, *J. Electrochem. Soc.* 123(1976) 270.
49. J. Kane, H. P. Schweizer and W. Kern, *J. Electrochem. Soc.* 122(1975) 1144.
50. Wolden, C., Personal Communication.
51. K. Sato, Y. Gotoh, Y. Wakayama and Y. Hayashi, *Rep. Res. Lab. Asahi Glass Co. Ltd.*, 42 (1992) 129.
52. M. Mizuhashi, Y. Gotoh and K. Adachi, *Jpn. J. Appl. Phys.*, 27 (1988) 2053.
53. D. Albin, D. Rose, R. Dhere, NREL/SNL 14th PV Program Review meeting, Lakewood, (1996).
54. B. M. Askerov, *Electron Transport Phenomena in Semiconductors*, World Scientific, Singapore, 1994.
55. O. Madelung, *Semiconductors other than Group IV Elements and III-V Compounds*, Springer-Verlag Berlin Heidelberg, New York 1992.
56. C. Herring, E. Fogt, *Phys. Rev.*, 101 (1956) 944.
57. G. Sanon, R. Rup and A. Mansingh, *Phys. Stat. Sol.(a)*, 135 (1993) 581.
58. E. M. Conwell, V. F. Weisskoff, *Phys. Rev.*, 77 (1950) 388.
59. H. Brooks, *Phys. Rev. A*, 38 (1951) 879.
60. H. Brooks, *Advances in Electronics and Electron. Phys.*, 7 (1955) 87.
61. R. Mansfield, *Proc. Phys. Soc. B*, 69 (1956) 79.